ABSTRACT

Title of Document: FABRICATION AND CHARACTERIZATION OF MAGNETOSTRICTIVE THIN FILMS USING THE COMBINATORIAL METHOD

Dwight Denroy Hunter, Doctor of Philosophy, 2011

Directed By: Professor Ichiro Takeuchi, Department of Materials Science and Engineering

Magnetostrictive materials are smart materials which show dimensional and magnetization changes in response to magnetic fields. Presently, there is growing interest to find magnetostrictive thin films for many microsystem applications, especially in microelectromechanical systems (MEMS) as powerful transducers for microactuators. But to exploit their capabilities and meet the stringent needs of microactuator and sensor applications, small driving magnetic fields on the order of mT are desirable. Current magnetostrictive materials such as rare-earth containing Terfenol, despite exhibiting giant magnetostriction, is at an extreme disadvantage due to the high saturation field ($H > 0.1$ T) imposed by its large magnetocrystalline anisotropy. Recently, large magnetostriction was observed in Fe-Ga alloys, and has sparked widespread research into other Fe-based alloys for possible replacements of Terfenol. Furthermore, it is becoming increasingly important to find rare-earth free compounds from a cost and availability point of view.

In this thesis, we investigated the composition dependent magnetostrictive and micro-structural properties of several binary (Fe-Ga, Co-Fe, Fe-Zn, Fe-W, Fe-Mo) and ternary (Fe-Ga-Zn, Fe-Co-Al) Fe-based thin film alloys prepared using a co-sputtering based composition spread approach. This technique facilitates synthesis and screening of large compositional landscapes in individual studies and allows rapid identification of compositions with enhanced physical properties. Magnetostriction measurements were performed on as-deposited and on some annealed composition spread films, which were fabricated on arrays of micro-machined cantilevers substrates.

From this study, binary Co-Fe thin film alloys emerged as a large magnetostrictive material with effective magnetostrictive values in excess of 260 ppm at a low saturation field ≈ 10 mT, which were quenched following a vacuum anneal at 800 ^{o}C for 1 hour. This substantial increase in magnetostriction was observed for compositions near the (fcc+bcc)/bcc phase boundary ($Co_{0.65}Fe_{0.5}$), and was found to depend on the cooling rate from the annealing temperature. Structural characterization by synchrotron micro-diffraction and transmission electron microscopy (TEM) reveals that this large increase in magnetostriction is associated with the presence of an equilibrium Co-rich fcc phase that precipitates into a Fe-rich bcc host phase upon annealing. The Co-Fe system is compared with Fe-Ga alloys, in which DO_3 nanoprecipitates dispersed in the host A2 matrix were observed at compositions ($Fe_{0.8}Ga_{0.2}$), which displays enhanced magnetostriction. The DO_3 nanoprecipitates in the Fe-Ga alloys are believed to behave as tetragonal defects in the matrix and their orientations can be changed by the application of a magnetic

field, leading to magnetostriction. It is speculated that the Co-rich precipitates in our Co-Fe films function in much the same way as the DO_3 precipitates in the Fe-Ga alloys, implying that the mechanisms which give rise to magnetostriction in both systems are similar.

The results on the as-deposited Fe-Ga-Zn and Fe-Co-Al ternary thin film spreads are somewhat encouraging from the point of view of finding new magnetostrictive materials. In the Fe-Ga-Zn alloys, we found that the magnetostriction value around the $Fe_{0.6}Ga_{0.1}Zn_{0.3}$ compositions was reasonably high, $\lambda_{eff} \sim 80$ ppm. This could be interesting from an application and cost points of view: this means that a less expensive metal such as Zn could be substituted for Gab, while still preserving the magnetostriction. For the Fe-Co-Al ternary, the highest effective magnetostriction, $\lambda_{eff} \sim 80$ ppm, was observed near the $Fe_{0.5}Co_{0.25}Al_{0.25}$ composition.

FABRICATION AND CHARACTERIZATION OF MAGNETOSTRICTIVE THIN FILMS USING THE COMBINATORIAL METHOD

By

Dwight Denroy Hunter

Dissertation submitted to the Faculty of the Graduate School of the
University of Maryland, College Park, in partial fulfillment
of the requirements for the degree of
Doctor of Philosophy
2011

Advisory Committee:
Professor Ichiro Takeuchi, Chair/Advisor
Professor Lordes Salamanca-Riba
Professor John Cumings
Professor Samuel E. Lofland
Professor Hugh Bruck

Dedication

To my maternal grandmother, Patricka Ambrozine Swaby, for all that she has given me!

Contents

Acknowledgements

First and foremost, I want to give thanks to God for this abundance of blessings and for enabling me with the ability to earn this degree. Please continue to bless me, and I ask for a daily dosage of humility so I may never forget the favor You have found in me.

My deepest appreciation goes out to my advisor Professor Ichiro Takeuchi for his mentorship, guidance, financial support and supervision of this work. Professor Takeuchi, I cannot thank you enough. I have really enjoyed working and learning from you these past 5 years. Looking back, I feel I have matured as a researcher and have evolved into a better and effective communicator, and I owe a great deal of that to you. I also want to express my sincere gratitude to my co-advisor Professor Manfred Wuttig for willingly imparting an abundance of knowledge if not the completion of this thesis would not be possible. Thank you for adjusting your schedule and making the time to see me on a moment's notice. I really enjoyed all your teachings both from a professional and social perspective. I also want to thank Professor Samuel E. Lofland at Rowan University for making his lab available and for his assistance for almost 3 years with magnetostriction experiments, valuable input, and help in transferring the magnetostriction setup from the lab at Rowan to our campus here in Maryland.

Thanks to Professors Lordes Salamanca-Riba, John Cumings, and Hugh Bruck for graciously accepting to serve on my dissertation committee. A hearty thank you goes out to former colleague Drs. Jason Hattrick-Simpers, Daisuke Kan, Debjani Banerjee, Anbu Varatharajan, Chris Long for numerous discussions and experimental

help. I want to thank Professor Isabel Lloyd for supporting my career development and introducing me to the Sloan program from which I received a grant to help support travel to conferences and research labs. I am grateful to Dr. Kathleen Hart, the graduate program coordinator for being such a strong advocate for us students and for reminding me about important deadlines. Also, a big thank you to the staff in the MSE and business office for processing purchase orders, travels, and doing a wonderful job to make my stay here a pleasant one.

I also want to give a special acknowledgement to the group at NIST especially Dr. Will Osborn, Dr. Ke Wang, Dr. Nataliya Kazantseva, and Dr. Leonid Bendersky for their collaboration on the various parts of this project. Also, thanks to Drs. Marcus Young and Apurva Mehta for securing beam time at SSRL for us. I also want to thank Drs. Peter Zavalij at the X-ray crystallographic center and Kenneth Evans-Lutterodt at BNL for help with X-ray analysis and beamtime, respectively. To Drs. Larry Dai, Wen-An Chiou, and Phil Piccoli here at the nanocenter for their experimental help. I want to also thank all members of Professor Takeuchi's group, both past and present especially R. Suchoski, I. Kierzewski, and E. Din for experimental help making cantilevers and depositing films. Thanks to the numerous students all over campus that I've been privileged to be friends with over the course of my time here at UMD.

A special acknowledgement and thanks to my mom, dad, brothers, and sisters for their constant encouragement and support, and to all my relatives in Jamaica.

Finally, I want to thank my family: my wife Brooke; my children Julian and Mckenzee, for their understanding and unwavering support throughout this journey.

List of Figures

List of Illustrations

List of Tables

Thesis Overview

The motivation for this thesis was driven both by curiosity and technological implications. It focuses on the exploration of magnetostrictive thin film materials, in particular Fe-based alloys through the application of combinatorial materials science methods for the accelerated development and discovery of large magnetostrictive materials and to investigate their composition-structure property relationships. In addition, the reader will become familiar with the growing effort dedicated to developing rare-earth free large magnetostrictive compounds for microactuators and other sensing needs. The Co-Fe alloys discussed in this thesis could perhaps one day replace some of the more expensive alloys that are currently in use.

This thesis is divided into seven chapters. Chapter 1 entails the main introductions to all the subtopics and concepts that comprise this thesis. Chapter 2 is the experimental method section. Chapters 3, 4, 5, and 6 are the results sections. Finally, Chapter 7 provides a global conclusion and an outlook at some future work that could be of potential interest.

Chapter 1: Introduction

Overview

This chapter serves as the primary introduction to all the subtopics contained in this thesis. It begins by reviewing some of the basic and fundamental principles of magnetism and discusses some of the underlying parameters that give rise to magnetism in materials. Next, the topic of ferromagnetism will be introduced followed by the concepts of magnetoelastic effects of which magnetostriction is a byproduct. Next I will delve into how magnetostriction is manifested in isotropic and anisotropic materials. This is followed by some historical examples of magnetostrictive materials and their applications. Finally, I will close the chapter with an introduction to the concepts of the combinatorial science which is the scientific method central to this thesis.

1.1: Magnetism

Magnetism is the magnetic response of materials to an applied magnetic field. This behavior is dictated by the interactions of the magnetic moments of the atoms in the material. Unlike mechanical forces, forces of magnetism are non-contact forces which manifest in the form of dipoles, where like poles repel each other and unlike poles attract each other. In general, magnetic materials are classified based on the way their local atomic moment couple to each other i.e. randomly oriented (not coupled at all) or partially coupled (can be parallel, anti-parallel). If the individual atomic moments, μ_m, are randomly oriented such that $\Sigma\mu_m = 0$ or experiences partial

coupling under the influence of a magnetic field then the material is said to be a paramagnet. Paramagnetic materials have magnetic moments which cancel each other in the absence of a magnetic field due to their non-ordering in the bulk material. They have susceptibility in the range 10^{-5} to 10^{-2} and such materials at best can only exhibit weak field induced magnetization. Alternatively, if the atomic moments are strongly coupled then the material will exhibit some type of magnetic ordering such that $\Sigma\mu_m \neq 0$ in the absence of a field. Depending on how the atomic moments are aligned (parallel, antiparallel), the material can be either ferromagnetic, antiferromagnetic, or ferrimagnetic. Materials that maintain strong parallel coupling of their atomic moments in the absence of a magnetic field are known as ferromagnets. This is due to the long range ordering of magnetic dipoles. These materials exhibit magnetostrictive behavior and constitute the focus of this thesis.

1.1.1: Ferromagnetism

In order to comprehend the concepts of magnetostriction and the behavior of magnetostrictive materials, a fundamental understanding of ferromagnetism is required.

Ferromagnetism is the resulting magnetic behavior exhibited by ferromagnets i.e. materials that have unpaired electrons. They are characterized by long range ordering of their atomic moments and tends to have spontaneous orientations of their magnetic spins, which are aligned parallel even in the absence of a magnetic field. The long-range spontaneous magnetization of a ferromagnet only exists at lower temperatures and vanishes above an ordering temperature known as the Curie

temperature Tc. Above Tc, the thermal energy agitates the atomic spins to a state of disorder and the spins are no longer parallel to each other. At this point, the material becomes paramagnetic and the susceptibility drops precipitously from $\chi \approx 10$ to 10^4 (ferromagnets) down to $\chi \approx 10^{-3}$ to 10^{-5} (paramagnets).

Materials such as iron (bcc α-phase), cobalt, nickel and rare-earth containing permanent magnets which exist in their ferromagnetic phase at room temperature are known as ferromagnetic materials. The maximum value of magnetization or saturation magnetization (M_s) is achieved when the applied field is able to align all the magnetic moments in the material in the direction of the applied field. Thus the M_s can be viewed as the product of the magnetic moment of each atom and the number of atoms in the material, divided by the volume of material. The magnetic moment mentioned here is due to the electron spin and orbital motion of electron around the nucleus. The coupling of magnetic moments between adjacent atoms can occur in materials other than ferromagnets. If the spins are arranged in opposite directions then the material is said to be antiferromagnetic. Figure 1.1 shows a schematic of the localized spin alignments in a ferromagnet and that of an antiferromagnet characterized by antiparallel spins.

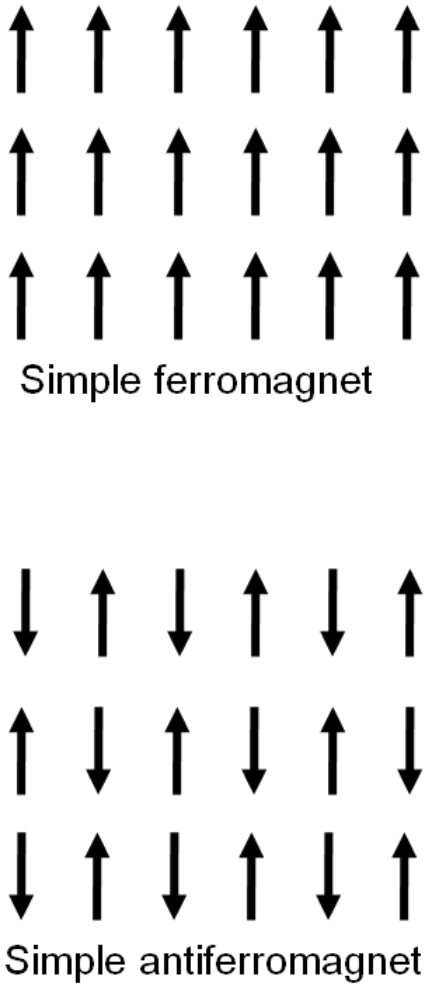

Figure 1.1 Examples of two types of magnetic order using an array of localized moments. Top) simple ferromagnetism, and bottom) simple antiferromagnetism.

1.2: Introduction to magnetostriction

The change of the magnetization of a ferromagnetic material is almost always accompanied by a change in its dimensions. The resulting change is called magnetostriction and is defined as the measure of the fractional change in the dimensions of a ferromagnetic material when an external magnetic field is applied. This strain induced by a directional magnetic field is called the magnetostrictive strain and was first observed in 1842 by James Joule, when he observed that a sample of iron changes its length when magnetized. The magnetostrictive strain is denoted by $\lambda = \Delta l/l$, where l is the unmagnetized length and Δl is the change in length after the material has been magnetized. From a phenomenological point of view, there are two types of magnetostriction: spontaneous magnetostriction which arises from the ordering of magnetic moments into domains at the Curie temperature; and field induced magnetostriction, which is more technologically important and the focus in this thesis. Both cases are discussed in the following sections.

1.2.1: Spontaneous magnetostriction

As stated above, all ferromagnetic materials are in their non-ordered magnetic state above their Curie temperature. When a ferromagnetic material is cooled through its Curie (ordering) temperature, the previously non-ordered magnetic moments which were randomly oriented becomes ordered over a long range encompassing a large volume of atoms due to exchange interaction. In these volumes called "domains" all the magnetic moments lie parallel to each other. However, the direction of spontaneous magnetization M_s varies from domain to domain throughout the

material such that the net magnetization of the bulk material is zero. This is due to the minimization of the magnetostatic energy of the overall material.

We consider an isotropic material in its paramagnetic state having spherical domains of unstrained solid, represented by spherical solids in Figure 1.1a, and we lower the temperature. At the onset of ferromagnetism, i.e. when spontaneous magnetization occurs and the magnetic moments become ordered, there is an associated strain e or magnetostriction λ_0 along a particular direction as shown in Figure 1.1b. Within each domain, the strain varies with an angle θ from the direction of spontaneous magnetization according to the relation:

$$e(\theta) = e\ cos^2\theta \tag{1.1}$$

Since a material can consist of polycrystalline grains, the domains will be oriented at random and any crystallographic direction is likely. Therefore, the average deformation throughout the material can be obtained by integration

$$\lambda_0 = \int_{-\frac{\pi}{2}}^{\frac{\pi}{2}} e cos^2\,\theta\ sin\theta\ d\theta \tag{1.2}$$

$$= e/3.$$

Thus, this is the spontaneous magnetostriction caused by long range ordering of magnetic moments at the onset of ferromagnetism. It is important to note that for this scenario the strain is equally distributed in all directions such that although the sample undergoes changes in dimensions, its shape remains the same.

1.2.2: Field induced magnetostriction

Now let's consider field induced magnetostriction. Here, we consider the magnetostriction which is the fractional change in length between a demagnetized ferromagnetic state and a magnetized state. In other words, there is a transition from an ordered but demagnetized state to the ordered saturated state under the application of a magnetic field. In the saturated state, the magnetic moments in each domain are all aligned in the direction of the field therefore causing the strains to be parallel to the field as shown in Figure 1.1c. The resulting saturation magnetostriction can then be represented as the following

$$\lambda_s = e - \lambda_0 \tag{1.3}$$

$$\lambda_s = (e - \frac{e}{3}) = \frac{2}{3}e \tag{1.4}$$

Therefore by measuring the saturation magnetostriction λ_s, one can measure the spontaneous strain *e* within a material due to magnetic ordering.

The saturation magnetostriction also depends on the angle θ to the magnetic field. For an isotropic material the saturation magnetostriction $\lambda_s(\theta)$ at any angle θ to the field direction is given by:

$$\lambda_s(\theta) = \frac{3}{2}\lambda_s(cos^2\theta - \frac{1}{3}) \tag{1.5}$$

where λ_s is the saturation magnetostriction along the direction of magnetization. In most experiments, the field is either applied parallel or perpendicular to a sample direction and their saturation magnetostriction is given in terms of the direction in

which the field was applied as $\lambda_{s\parallel}$ and $\lambda_{s\perp}$ for field applied in parallel and perpendicular directions to the selected sample direction, respectively. The difference between these two quantities gives the spontaneous strain within a single domain.

$$\lambda_{s\parallel} - \lambda_{s\perp} = \lambda_s + \frac{\lambda_s}{2} = \frac{3}{2}\lambda_s = e \tag{1.6}$$

Thus the strain in an isotropic material is given by the expression above.

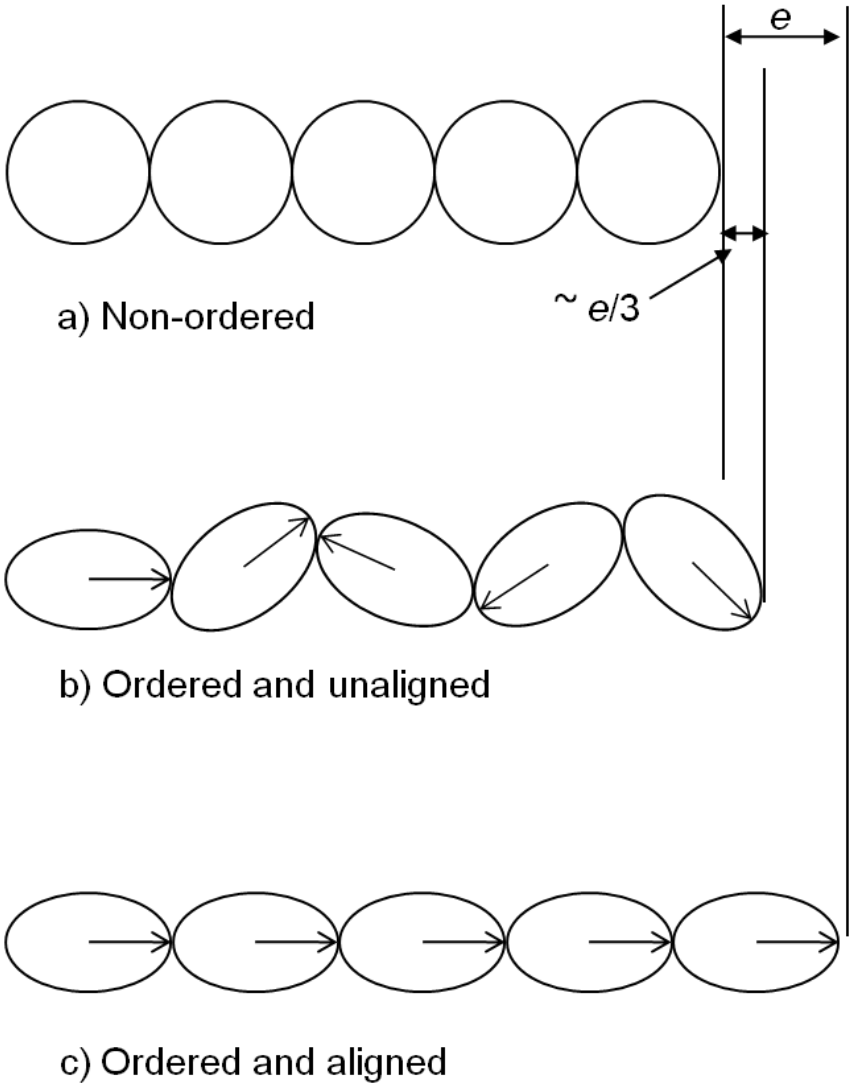

Figure 1.2 Schematic diagram illustrating the magnetostriction in: (a) the non-ordered (paramagnetic) state; (b) the ferromagnetic state demagnetized; and (c) the ferromagnetic state, magnetized to saturation[1].

Anisotropic materials

The exchange interaction which occurs at the Curie temperature leads to spontaneous magnetization. However, it does not dictate in which direction the magnetization will align. Therefore, magnetization is free to orient along any crystallographic direction without altering the internal energy. However, in all ferromagnetic materials there exists a preferred direction known as the "easy axis" in which the magnetization likes to align. The direction varies for different classes of materials with different crystal structures but in general, rotation of the magnetization away from the easy direction increases the internal energy of the system. Since the energy of the system is at its minimum when the magnetization is aligned along the easy direction, rotation of the magnetization can only occur by means of a magnetic field. This energy which dictates the preference in magnetization orientation is called the magnetic anisotropy, and the anisotropy that assigns energy to different directions in the crystal is called the magnetocrystalline anisotropy.

Since most ferromagnetic materials exhibit some degree of anisotropy, the saturation magnetostriction needs to be defined relative to the crystal axes along which the magnetization lies. For a cubic crystal structure there are two principal directions in which the magnetization likes to orient: they are <100> or <111> crystallographic directions.

The magnetostrictions or spontaneous strains are defined along those directions. In the case of cubic materials there are two independent magnetostriction constants λ_{100} and λ_{111}. Table 1 shows the two magnetostrictive coefficients for some cubic materials. The values can sometimes vary substantially as is the case in

Terfenol. The directional dependence of the saturation magnetostriction of a single domain single crystal cubic structure is given by:

$$\lambda_s = \frac{3}{2}\lambda_{100}\left(\alpha_1^2\beta_1^2 + \alpha_2^2\beta_2^2 + \alpha_3^2\beta_3^2 - \frac{1}{3}\right) + 3\lambda_{111}(\alpha_1\alpha_2\beta_1\beta_2 + \alpha_2\alpha_3\beta_2\beta_3 + \alpha_3\alpha_1\beta_3\beta_1) \quad (1.7)$$

where λ_{100} is the saturation magnetostriction measured along the ⟨100⟩ direction, λ_{111} is the saturation magnetostriction along the ⟨111⟩ direction, α_1, α_2, α_3 are directional cosines relative to the field direction of the axis along which the magnetic moments are saturated, and β_1, β_2, β_3 are the directional cosines relative to the field direction in which the saturation magnetostriction was measured. The spontaneous strains along the two principal axes are $e_{100} = (3/2)\lambda_{100}$ and $e_{111} = (3/2)\lambda_{111}$.

Magnetostrictive effects arise due to the reorientation of magnetization by both magnetic fields and stress, and is known as magnetomechanical or magnetoelastic effect. The magnetoelastic effect will be discussed next.

Table 1 Magnetostriction coefficients of some cubic materials

Material	**λ_{100} (ppm)**	**λ_{111} (ppm)**
Iron	21	-21
Nickel	-46	-24
Terfenol	90	1600

1.3: Magnetoelastic effects

The phenomenon of magnetostriction is the manifestation of the magnetoelastic coupling which exists in all ferromagnetic materials. This behavior is observed to some degree in all magnetic materials and manifests itself in different ways. Over the years such behaviors have been categorized, and their various names and descriptions are listed below.

Joule effect

The Joule effect[2] was first discovered by James Prescott Joule in 1842, and it is characterized by a change in length due a change in the magnetization state of the material. This is also sometimes known as linear magnetostriction and assumes that the volume of the material remains constant. More details on this type of magnetostriction will be presented in section 1.3.2.

Villari effect

The Villari effect[3] (1865) otherwise known as the inverse Joule effect or stress induced anisotropy describes the mechanical stress-induced change in magnetization. Materials with a positive magnetostriction will show an increase in magnetization as the stress is increased, while materials with negative magnetostriction exhibits a decrease in magnetization with decreased stress. If λ_s is positive, it is easier to magnetize the material in the tensile stress ($\sigma > 0$) direction. In general, it is harder to magnetize a material in a direction for which $\lambda_s < 0$ and $\sigma > 0$ or $\lambda_s > 0$ and $\sigma < 0$.

Wiedemann effect

The Wiedemann effect[4] arises due to the torsional motion of a sample when a current passing through a magnetic material in the direction of magnetization causes a twisting of the magnetization around a current axis. In the inverse effect known as the "Matteucci effect," a mechanical twisting of the sample causes a voltage drop to appear along the sample length consistent with the Faraday's law and the strain-induced magnetization change.

Volume Magnetostriction

Barrett (1882) observed that the volume changed in certain ferromagnetic materials under the influence of a magnetic field and coined the term "volume magnetostriction[5]." In this scenario, the material undergoes an isotropic expansion of the lattice. Volume magnetostriction typically occurs at high fields and the increase is small and therefore has no practical applications.

Conventionally, the *Joule* and *Wiedemann* effects are used for actuation purposes, whereas the *Villari* and *Matteucci* effects are used for sensing purposes.

1.3.1: Magnetoelastic energy

Magnetoelastic energy is the energy expressed in terms of magnetization direction of the atomic moments and the lattice strain. It arises from the strain dependence of the magnetostatic energy, magnetocrystalline anisotropy energy, and the Heisenberg exchange energy. In actuality, solid ferromagnets are not rigid but rather elastic, and the magnetoelastic energy can modify the magnetization properties

in a material when subjected to a mechanical stress. Due to the magnetoelastic energy, the material strains when its magnetization is changed. Typical magnetostriction values can range from near zero $\lambda \sim 10^{-7}$ to nearly $\pm 10^{-4}$ in *3d* metals and alloys. There is a magnetic stress tensor called the magnetoelastic coupling coefficient B_{ij} which relates the magnetostrictive strains in formula: $B_{ij} \propto C_{ijkl}\ \lambda_{kl.}$ *w*here C = Young's modulus. Magnetoelastic coupling arises from spin-orbit coupling and strong interaction between electron clouds of adjacent atoms. The reciprocal effect holds true also, i.e. the magnetization changes if the material is stressed by external mechanical force. As stated earlier, this phenomenon was first observed by Villari in 1865 and has since been known as the *Villari effect*[3]or the inverse *Joule effect*.

1.3.2: Mechanism of Joule Magnetostriction

Joule magnetostriction arises from the spin-orbit coupling and is an inherent material property that does not degrade with time. The large phenomenon of Joule magnetostriction can be viewed as a result of the transition from a demagnetized multi-domain state to a single domain state through the motion of domain walls due to the application of a directional magnetic field. As seen in the schematic of Figure 1.2b and 1.2c, the magnetic moments in the material is a makeup of the orbital spins (black arrows) and surrounding electron clouds (ellipses), which are strongly coupled to the crystal lattice structure, for a ferromagnetic sample in two states. At H=0 (Figure 1.2b) or when no magnetic field is applied the spins are coupled to the orbits in a random orientation. The application of a magnetic field tries to orient the electron

spins along the direction of the applied field. The orbits which are coupled to the spins also rotate as shown in Figure 1.2c. It is this rotation of the orbits and the associated distortion of the crystal lattice which manifests as magnetostriction. The ideal spin-orbit coupling should be large enough to produce significant lattice distortion but at the same time the magnetocrystalline anisotropy should be small enough so that the lattice can be distorted by applying small magnetic fields.

Joule magnetostriction can also be considered as the relationship between the spontaneous magnetization and elastic response of a material, and thus measurements of magnetostrictive strains are convoluted functions of the respective magnetostrictive constants of the principal axes. For example, in a cubic material, the measured strain is related to the saturation magnetostrictive constants along the [100] λ_{100} and [111] λ_{111} directions by equation (1.7). In polycrystalline samples, there is random orientation of the crystal axis with respect to the measurement direction, and one must average the contributions of the two magnetostrictions over all possible orientations of the measurement direction with respect to the crystal axis. This can be achieved by evaluating the following integral

$$\lambda_s = \int_{\theta=0}^{\frac{\pi}{2}} \int_{\phi=0}^{\frac{\pi}{2}} \lambda_s \sin\theta d\theta d\phi \qquad (1.8)$$

Usually to obtain the saturation magnetostriction, it is necessary to magnetize the samples in two orthogonal directions to ensure that the domains have switched between two orthogonal single domain states. This is primarily done to remove any ambiguity that arises from determining the strain of the zero magnetization state since at zero magnetization, there can be an infinite number of possible domain

configurations. However, in most bcc bulk materials, especially Fe-based, the [100] direction gives a substantially larger magnetostriction than the [111] direction, so measuring λ_{100} is sufficient to get a good idea of the magnetostrictive constant. Figure 1.3 illustrates the joule magnetostriction in bulk and thin film materials. In bulk, the material expands/contracts linearly until saturation along the same direction in which the field was applied. For thin film materials clamped to substrates, application of a magnetic field results in bending of the substrate. Figure 1.3 also shows the bending motion of the substrate derived from applying field along two different directions.

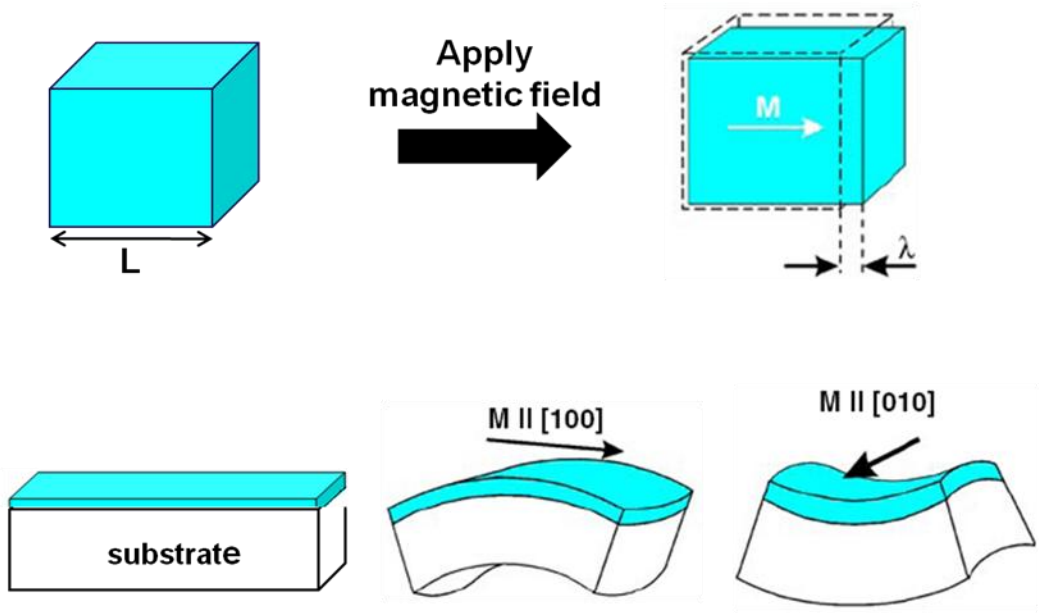

Figure 1.3 Schematic of Joule magnetostriction illustrated in different materials. top) bulk and bottom) thin films.

1.4: Magnetostrictive materials

Magnetostrictive materials are active materials which can transduce energy from one form to another. The capability of energy transduction in active materials makes them different from a passive device such as hydraulic press which only transmits (not transduces) mechanical energy through a fluid, thereby producing a mechanical advantage. Although, sensing and actuation requires active materials, the requirements of ideal sensors can be different from that for actuators. Table 2 summarizes some of the desirable characteristics for actuators and sensors.

Table 2 Desirable characteristics of actuators and sensors Ref[6].

Actuator	**Sensor**
Large stroke	High sensitivity
Large blocked force	Large range
High stiffness	High resolution
High coupling factor	Low drift
Impedance matching	High accuracy and precision

Since the discovery of magnetostriction by Joule[2] in 1842 in an Fe specimen, most ferromagnetic materials have been found to exhibit some degree of magnetostriction. Some of the earlier and most common materials to show magnetostriction include pure elements such as Fe, Ni, and Co. They have magnetostriction on the order of 10 $\mu\varepsilon$ and have limited use in practical applications. However, this changed with the development of rare-earth (RE) alloy systems which

include Terfenol-D, a Tb-Dy-Fe alloy that can generate a giant magnetostrictive strain over 2000 ppm.

1.4.1: Bulk magnetostrictive materials

Most of the magnetostrictive materials currently being studied are in bulk forms. By bulk, we mean a piece of three dimensional material, where its overall shape usually does not matter but it is at least several microns thick in each dimension. Since this dissertation is on the study of thin-film materials, most of the discussions will be limited to thin film materials, where the material is very large in two directions and have thickness of the order of ~ 0.5 μm in the third dimension.

1.4.2: Thin-film magnetostrictive materials

There has been a growing interest in developing thin film magnetostrictive materials for applications where bulk is not possible. Most of the magnetostrictive materials studied in bulk have also been studied in thin films. Magnetostriction in thin film is usually smaller compared to bulk materials due to the clamping effect imposed by the substrate. However, from an applications point of view, thin film magnetostrictive materials are vastly important and there are many critical applications such as sensors and micro-actuators in smart microsystems. To fully exploit their capabilities for microactuators and sensors applications, small driving magnetic fields on the order of mT is desirable.

Studies on magnetostrictive films date back to the mid 1970's[7]. Since then various single layer and multilayer alloy films have been investigated[8-13]. The main idea behind the multilayer design is to decrease the saturation field while preserving the magnetostriction. To date, the multilayer film TbFe/FeCo consisting of alternate layers (8 nm) of giant magnetostrictive amorphous TbFe metals and high saturation magnetization FeCo have exhibited the largest magnetostriction of about 550 ppm at 20 mT field[14-15]. It is believed that the large magnetostriction in thin multilayer arises from enhancement in the magnetic polarization and very high magnetoelastic energies. Some of the conditions for designing giant magnetostrictive multilayer films include deposition under a magnetic field and some type of post-field annealing. This is necessary in order to induce an easy axis in a desired in-plane direction[11].

Single layer films, such as those to be discussed in this thesis have great practical applications. It is also increasingly important to find rare-earth free compounds to reduce cost and increase availability. In the next section, I will introduce some of the growing applications of magnetostrictive films.

1.4.3: Applications of magnetostrictive films

Thin film materials that exhibit giant magnetostriction are of technological importance due to their potential use in microsystem applications, especially microelectromechanical systems (MEMS) as powerful transducers for microactuators[15-18]. Other attractive features are remote control operation without wires, simple actuator designs, low fabrication temperatures, and compatibility with

microelectronics manufacturing processes, allowing for seamless integration in current technologies [8,15,19-21].

Actuators

In an actuator device, applying a magnetic field causes a shape change. Based on this phenomenon, devices can be used to do work. In fact, actuators using bulk magnetostrictive materials are currently in existence such as under-water sonar devices. One of the growing applications for which magnetostrictive materials are gaining interest is in the field as microactuators. However, for this application to be realized we need low saturation field on the order of mT. Figure 1.4 shows two examples of actuator designs using magnetostrictive thin films. These examples[16] demonstrate the promising actuation mechanism for realization of different microactuators, especially if large magnetostriction at low fields can be achieved.

Sensors

In a magnetostrictive sensor device, stressing the material causes a change in the magnetization state of the material. An excellent example of a sensor application is a magnetoelectric sensor which uses the magnetoelectric (ME) effect. The working principle behind the ME effect is that magnetic field induced strain (λ) in the magnetostrictive layer which is transferred to a strain (ε) in the piezoelectric component through elastic coupling, resulting in a piezoelectric induced voltage. By utilizing such a multilayer composite configuration, a large ME coupling can be obtained[22].

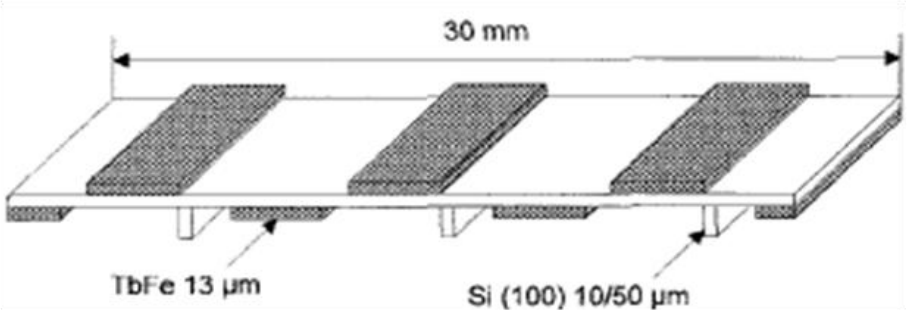

Ultrasonic magnetostrictive thin film micromotor

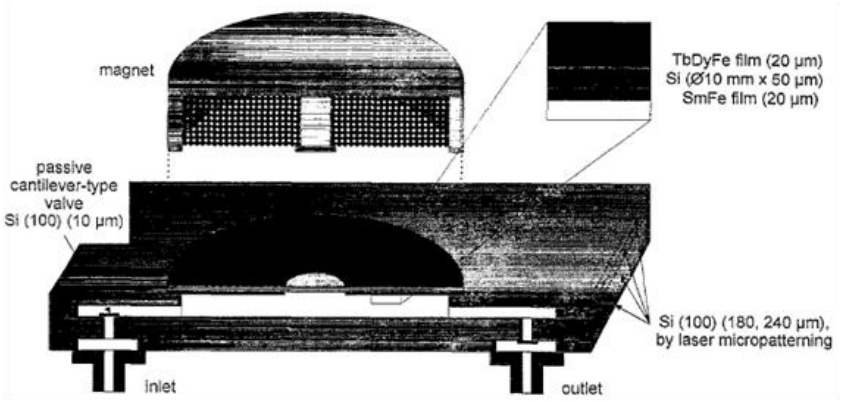

cross-section of the magnetostrictive membrane-type micropump

Figure 1.3 Examples of two actuator designs using magnetostrictive thin films. top) ultrasonic micromotor, and bottom) magnetostrictive micropump, from Ref[16].

As an example, an all thin-film ME sensor based on magnetostrictive and piezoelectric layers is shown in Figure 1.5. This design allows for fabrication of sensor arrays as well as integration with other circuit components. Also a major advantage of the all-thin-film devices over that of bulk-based devices is the fact that the ME coupling is achieved through natural film adhesion rather than the epoxy resin used in bulk magnetostrictive/piezoelectric laminate composite.

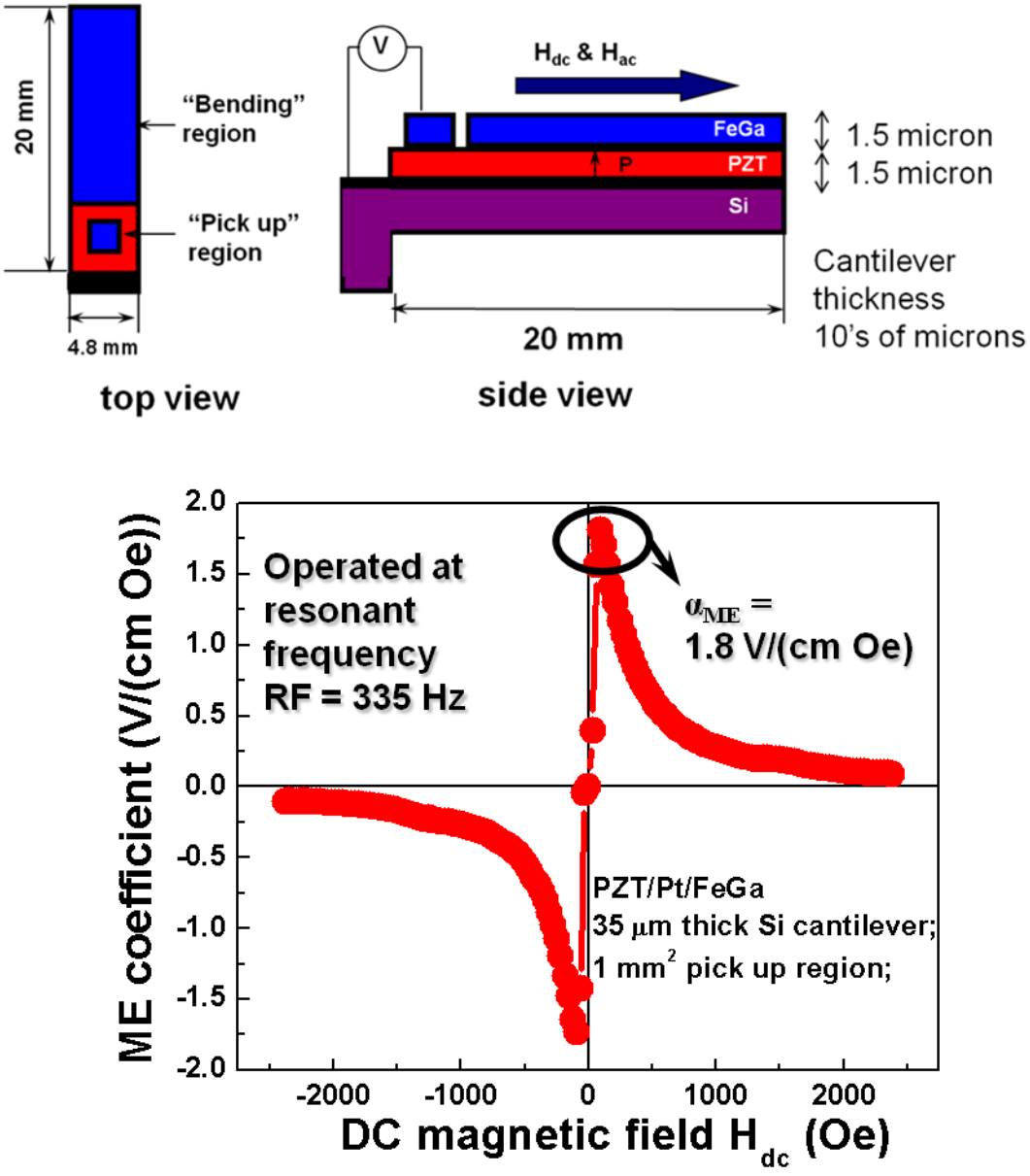

Figure 1.4 Illustration of an all thin-film ME device for sensor applications. top) schematic of the fabricated structure, left) top view, right) side view. bottom) measured ME coefficient of the composite device as a function of dc magnetic field at its mechanical resonant frequency Ref[22].

In chapters 3-6 of this thesis, I will discuss some magnetostrictive thin film materials that we have been exploring which can potentially used in applications, such as the ones discussed above.

1.5: Combinatorial Materials Science

Combinatorial materials science is a high-throughput materials exploration approach. It is geared toward rapid discovery, study, and optimization of new and known compounds by combining parallel synthesis, high-throughput screening, and fast data processing. Its goal is to investigate properties of large numbers of compositionally varying materials simultaneously. It allows synthesis and screening of large compositional landscapes in individual studies and facilitates rapid identification of compositions with enhanced physical properties. The term "combinatorial" refers the act of combining and "mixing" different materials or groups of elements as their constituents in order to arrive at new multi-component compounds. Combinatorial synthesis techniques have been used to fabricate assemblies of both bulk and thin-film materials. However, the application of the combinatorial methodology to technologically interesting smart materials is best implemented in the form of thin-film libraries.

By one account, the earliest history of a high-throughput approach to materials exploration can be traced back to 1878 when Thomas Edison applied parallel and combinatorial methods for the investigation of suitable filament materials for the incandescent lamp as outlined in a review by Schubert and co-workers[23]. In 1970, Hanak successfully demonstrated the principle idea of a composition spread or

gradient libraries at the research laboratories of RCA in the investigation of inorganic materials[24]. However, it wasn't until 1995 when Xiang et al.[25] coined the term combinatorial approach to materials discovery that the "multiple-sample concept" took off. Since then numerous studies have demonstrated the applicability of the combinatorial methodology in a variety of materials systems ranging from catalysts and biomaterials to electronic materials and polymers[26-40]. Rapid synthesis of materials libraries and their high-throughput characterization is also instrumental in the determination of compositional phase diagrams. The concept of the combinatorial thin film library is discussed in the following section.

1.5.1: Materials libraries

A combinatorial library is a large number of spatially addressable, compositionally varying samples which were fabricated in a single synthesis/deposition experiment. There are three different types of materials library designs which can be used in the combinatorial approach for materials exploration. They are natural composition spread libraries, discrete libraries, and the layer-by-layer composition spread.

The natural composition spread is usually implemented through a co-deposition technique resulting in intimate atomic mixing of materials during deposition. Figure 1.6a shows a schematic of this design. In this example, three elements/compounds (A, B, and C) are co-sputtered. The deposition profile from each element/compound during deposition is such that there is a thickness gradient the farther one goes away from the position directly below each target. Co-sputtering

multiple elements/compounds results in a relatively uniform thickness, and the regions of a wafer where the deposition profiles overlap result in an atomically mixed composition spread. In fact, one advantage of this technique is the uniform atomic intermixing during deposition in the plasma which negates the need for post annealing to acquire compositional homogeneity throughout the thickness of the film[28-29]. The discrete library has sets of separated samples with discrete compositions (Figure. 1.6b) and allows for rapid screening of a large number of compositionally disparate materials. Each site is spatially separated from its neighbor through shadow masking and can be individually addressed. Such libraries have been used in the investigation of luminescence materials as shown in Figure 1.6b[25]. The layer-by-layer deposition library can be used to generate a continuous composition variation which can be denoted, for instance, by $A_{1-x}B_x$. By utilizing a continuously moving masking system, the composition can be made to vary from pure *A* on one end to pure *B* on the other end in a binary spread as shown in Figure 1.6c. The samples are deposited in a layer-by-layer wedge configuration which allows for atomic mixing at the nanometer level. This type of library is more suitable for the determination of composition-structure-property relationships with respect to a given binary/ternary compositional phase diagram[41].

In this thesis the natural composition spread library, illustrated in Figure 1.6a was used in the fabrication of binary and ternary composition spreads on cantilever substrates. The use of the natural composition techniques has already been shown to be a reliable method for exploring previously unknown regions of phase diagrams for new materials with enhanced physical properties[28,42-44]. Here, efforts to explore the

functional phase diagrams of various binary and ternary Fe-based systems will be described, with emphasis on the structure-magnetostrictive property relationship.

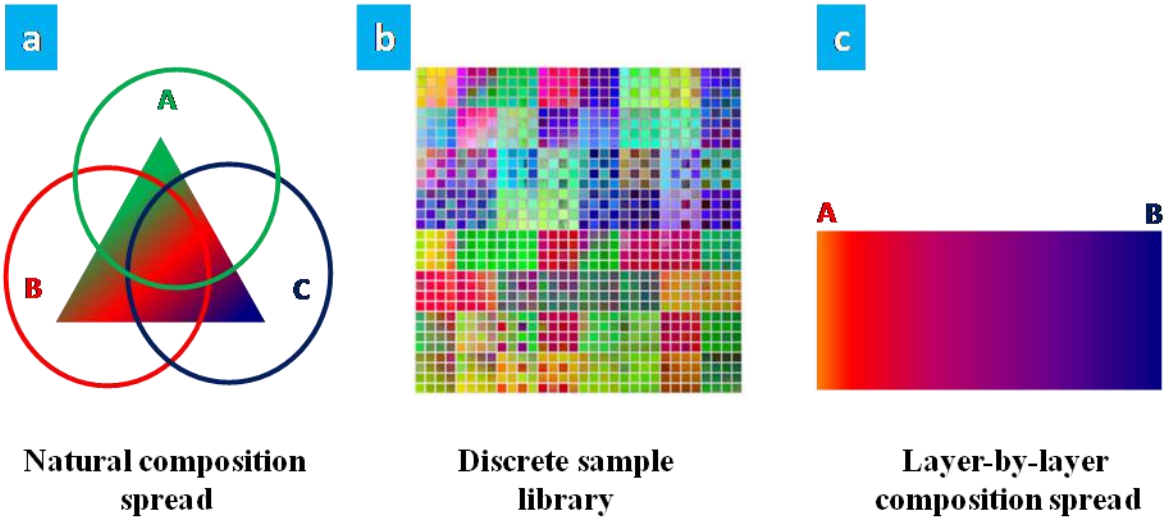

Figure 1.5 Examples of common combinatorial sample designs. a) Natural composition spread, the type used in the present work. b) Photograph of the as-deposited discrete quaternary library under ambient light used in the search for a blue photoluminescent composite material. The array of colors in the different sites arises from variations in the film thicknesses and their different optical indices of reflection[25]. c) Schematic of a layer-by-layer composition spread showing pure A on one end of the binary spread and pure B on the other.

Chapter 2: Experimental Methods

Overview

This chapter describes the various experimental methods that were used in the fabrication and characterization of thin-film composition spreads studied here. It begins with a description of the design and fabrication of the cantilever substrates, followed by details on the thin film fabrication process using a specialized combinatorial sputtering system for depositing all the films investigated in this work. I will then describe the post-deposition thermal treatment which was performed on some of the composition spread samples. This will be followed by an in-depth discussion of a revised method to measure magnetostriction in thin-films using the cantilever method. A brief description on the measurements performed to determine the elastic modulus, which in turn is used in the calculation of magnetostriction is also presented. Finally, I will close this chapter with descriptions of the TEM and synchrotron micro-diffraction techniques which were used for micro-structural characterization on the samples.

2.1: Fabricating the cantilever substrates

Each thin film sample studied in this thesis was deposited onto arrays of mm sized cantilevers, which had been patterned from 3-in thermally oxidized (1.5 μm SiO_2) Si wafers via standard Si bulk micromachining techniques. The etching of the cantilevers involves a sequence of photolithography steps performed in a clean-room as described in the flowchart below.

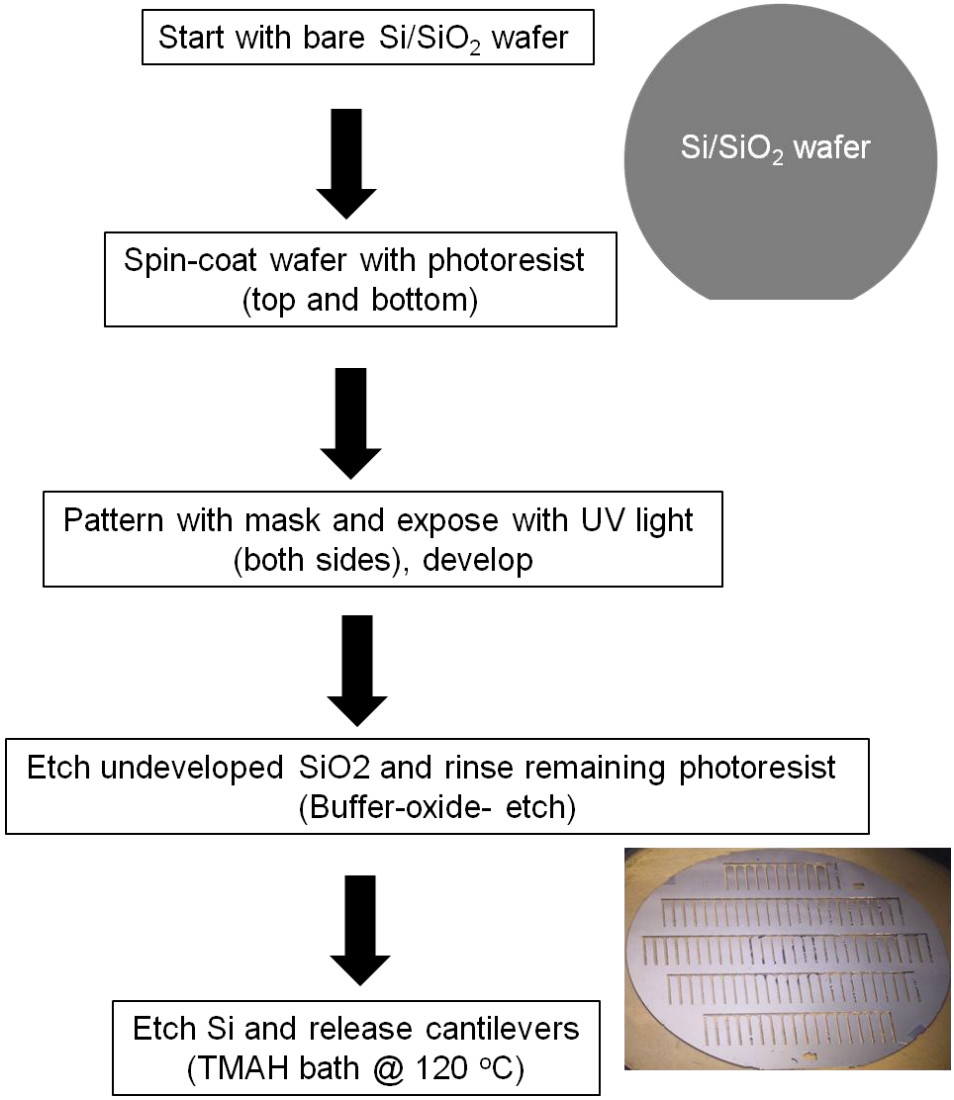

Illustration 1 Flow diagram showing the lithographic steps involved in the fabrication of the cantilevers used in this thesis.

At the end of the wet etching process, five rows totaling 101 identical unimorph cantilevers; 10 mm thick, 2 mm wide, and 70 μm thick were fabricated and used as a substrate during thin film depositions. Depositing thin films on cantilever substrates instead of whole wafers provides the advantage that the film is no longer completely constrained by the full substrate, and thus changes in actuation properties

can be detected. The process of monitoring the displacements of cantilevers has been the basis for measurements of the thermal actuation of martensite[45], magnetic field actuation of magnetostrictives[40,42,46], and hydrogen adsorption/desorption in hydrogen storage materials[47]. For the deposition of thin-films on these cantilever substrates, we use a combinatorial co-sputtering based technique which will be discussed in the following section.

2.2: Combinatorial Magnetron Co-Sputter Deposition System

The natural composition spread libraries used in this work were deposited in a dedicated ultra-high vacuum (UHV) combinatorial sputtering system.

2.2.1: Magnetron sputtering

Sputtering is the removal of atomized material from a solid due to the energetic bombardment of its surface layers by ions or neutral particles. To begin the sputtering process, a controlled inert gas (such as Ar) is allowed inside the high vacuum chamber while a negative voltage (> -300 V) is applied to the target material to be sputtered causing a large potential drop across the material and the source. The high energy ions collide with the surface of the target, and some of their energies are transferred to the target. If the energy transfer is greater than the binding energy of the constituent atoms of the target material, collision cascades occurs resulting in atoms being scattered backwards and "sputtered" towards the substrate. Sputtering is a hyper- thermal process with energies of the species in the keV to MeV range.

A magnetron sputtering system is equipped with magnets which are fixed to the back of each target material to be sputtered. The magnetron creates a magnetic field which confines the orbits of the ions and electrons to maintain intensity of the plasma and to increase the collision rate with Ar gas. The target material hits the substrate with very high energy and cools to room temperature rather quickly, thus sputtering is considered a hyper-thermal process or quenching phenomenon. A schematic of the magnetron sputtering system is shown in Figure 2.1. One of the main advantages of a magnetron sputtering over a conventional sputtering is the wide range of target materials which can be sputtered. These range from pure metals where a d.c. power supply can be used to semiconductors and insulators which require r.f. power, and the depositions can be carried out in either non reactive (inert gas) or reactive (inert and reactive gas) discharges. Also, the magnetron causes a higher sputtering rate which enables lower pressure to be used. During the sputtering process, the electrons follow the helical paths dictated by the magnetic field lines thus undergoing additional collisions with the ions. These additional collisions enhance the ionization of the plasma near the target which results in a higher sputtering rate.

Sputtering was one of the first depositions techniques used to create compositions spread samples by Hanak et al. in the 1970's[24,48]. Recent combinatorial investigations have embraced sputtering due to its ability to deposit a variety of materials without heating the source material.

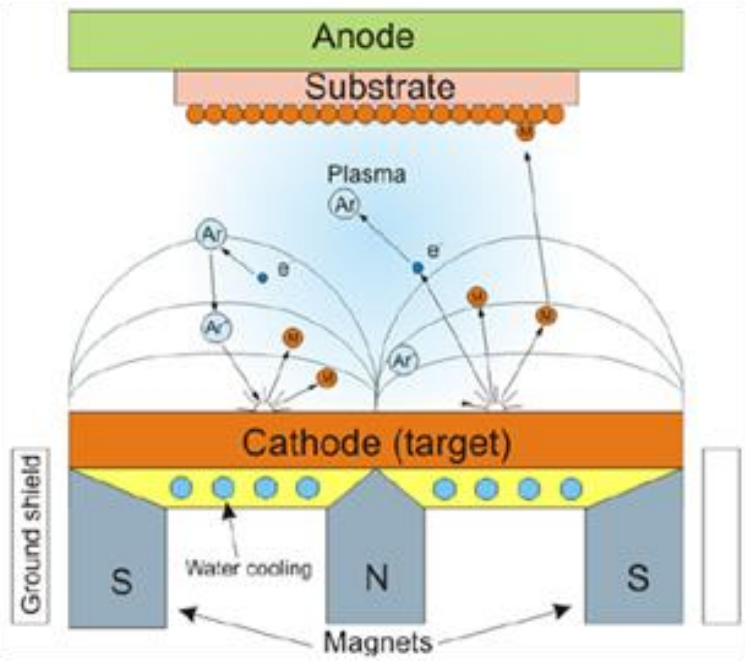

Figure 2.1 Schematic of magnetron sputtering. A magnetic field confines the orbits of the ions and electrons to maintain intensity of the plasma and to increase the collision rate with Ar gas. This significantly enhances the number of Ar ions formed and impinging on the target, knocking out individual atoms which are then deposited onto the substrate, taken from Ref[49].

2.2.2: Composition Spreads

The combinatorial magnetron sputtering system (Figure 2.2), used in these experiments can create compositions spreads across 3" silicon wafers by simultaneous sputtering of different materials which leads to a natural atomic mixing of elements. The main chamber has a cryo-pump (CP-8 Oxford) which creates a base pressure lower than 2 $x10^{-8}$ Torr. The system is equipped with 3 magnetron sputtering guns, parallelly placed and adjacent in a triangular geometry as shown in Figure 2.3. Each gun uses a 1.5" diameter target and can be sputtered simultaneously using either direct current (DC) or radio frequency (RF) power supply whose power can range from 5 to 200 Watts. The guns are housed in individual chimneys which help to

prevent cross-contamination as well as direct the plasma onto the substrate during deposition.

Elemental targets (purity: 99.99% or better) are used for the present experiments and pre-sputtered for at least 5 minutes at the beginning of each deposition run to minimize contamination. Depositions are performed with ultra-high purity (99.9995% purity) Ar at a typical pressure of 5 mTorr, with a target-to-substrate distance of 150 mm and without intentional substrate heating. During depositions, the sample is placed on a vertically height adjustable substrate heater allowing manipulation of the target-to-sample distances which in turn allows precise control over the size of the composition region to be covered within a compositional phase diagram. The substrate heater has a temperature range of 25-900 ^{o}C, and is used for in-situ post-deposition anneals.

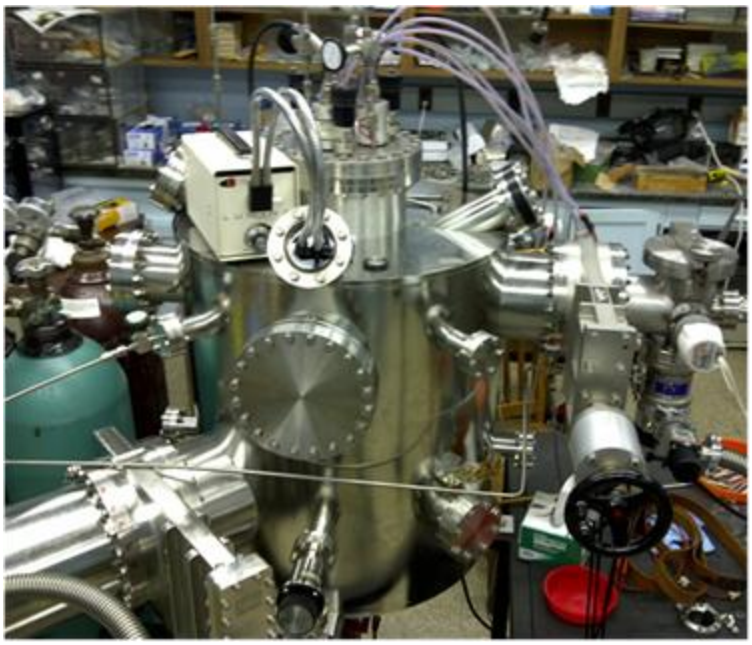

Figure 2.2 A picture of the magnetron co-sputter deposition system used in the experiments described in this thesis.

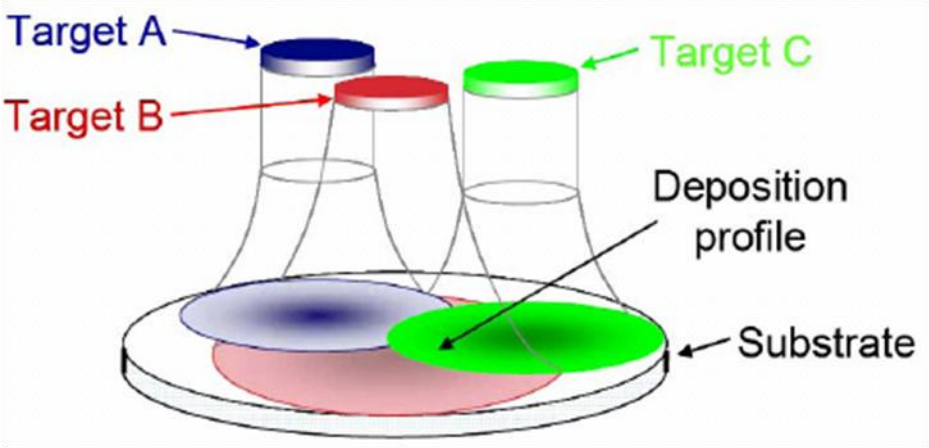

Figure 2.3 Schematic of gun/target orientation in our magnetron co-sputter deposition system[50]. This multi-gun configuration leads to the interatomic mixing of sputtered species A, B, & C during deposition as represented here.

As mentioned earlier, one of the special features about this particular chamber is the orientation of the sputtering guns. Typically, magnetron sputtering systems have guns that focus to the same point on the wafer usually to provide uniform composition across the wafer. In our case, the guns are non-confocal, and it is this non-confocal geometry that allows for the natural composition spreads to be fabricated without the use of a masking system.

For deposition of binary composition spreads, only two guns were used, but for ternary spreads the three gun orientation shown above was used.

2.3: High Vacuum Annealing

To capture any high temperature or metastable phases present in the thin-film composition spread samples, we utilize a high-vacuum quenching chamber, as shown in Figure 2.4. This narrow slit chamber is a mobile high-vacuum system that gets placed directly inside a modified in-house high temperature furnace. Prior to annealing, the wafers are placed inside the chamber, in contact with the inside wall of the chamber so that during annealing the chamber and the wafer are at the same temperature. The chamber is pumped down to high vacuum with a base pressure better than 10^{-9} torr using a cryopump (CP-5). The nose of the chamber is inserted into a high-temperature furnace for annealing. A schematic of this setup is shown in Figure 2.5. This is similar to the technique discussed in references[40,50].

Following high temperature annealing, the spreads are cooled from a high temperature while in vacuum either by slow-cooling or by quenching. For general slow-cooling, the chamber with the samples were pulled out of the high-temperature furnace at the end of the anneal and allowed to cooled down to room temperature. The typical cooling rate for the slow-cooled samples is approximately 2 $°C \cdot min^{-1}$. In the case of the quenched samples, the nose of the chamber with the samples were pulled out of the high-temperature furnace at the end of the anneal and immediately plunged into an ice-bath for rapidly cooling down to room temperature. It takes on average 2~5 seconds to obtain fully quenched samples, yielding a cooling rate cooling rate of 2.3×10^{3} $°C \cdot min^{-1}$. Since the sample is always in contact with the walls of the chamber, both the sample and the chamber cool at the same time.

Figure 2.4 Picture of the high-vacuum mobile quenching furnace used for performing high temperature high vacuum post-deposition annealing on some of our thin film composition spreads.

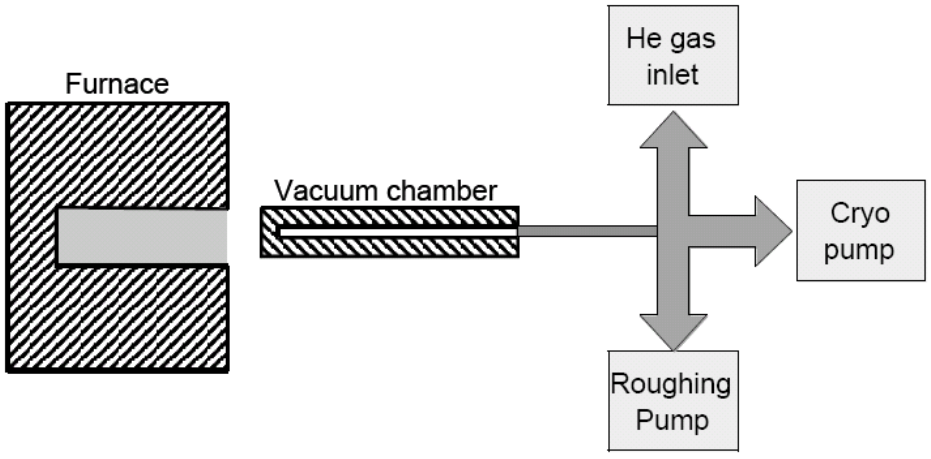

Figure 2.5 Schematic detailing the operation of the high vacuum quenching chamber for capturing high-temperature phases in thin film composition spread samples. The picture of the vacuum chamber is shown in Figure 2.4.

2.4: Measuring magnetostriction in cantilever thin films

The magnetostriction of all composition spread thin film samples (as-deposited and annealed) studied in this work were determined using the cantilever method[46]. A 635 nm power-stabilized diode laser (5 mW) was deflected off the tip of each cantilever onto a position sensitive detector (PSD) ON-TRAK OT301 precision sensing module. Once the magnetic field has been applied, cantilever bending occurs due to the magnetostriction in the film, and the resultant cantilever displacement is captured on the PSD and measured as a function of the applied field as schematically shown in Figure 2.6. Displacement measurements were recorded for magnetic fields applied parallel and perpendicular to the cantilever length.

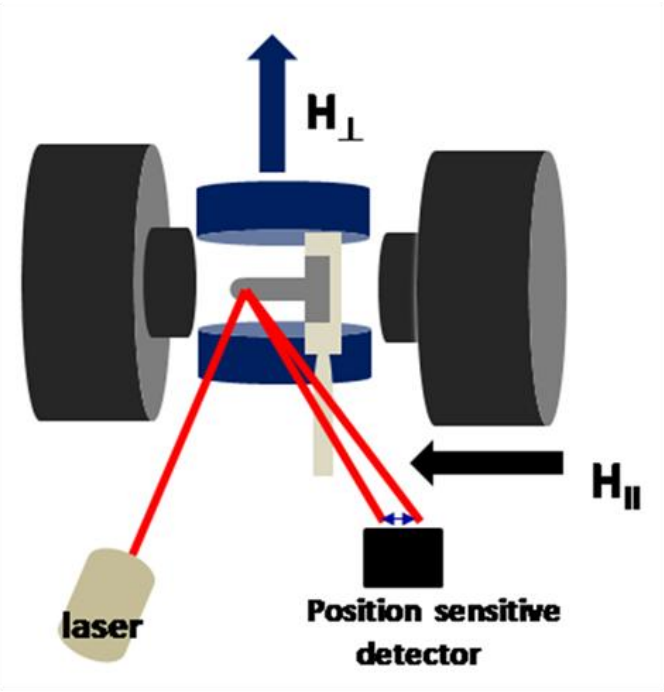

Figure 2.6 Schematic of the experimental setup for measuring magnetostriction in cantilever thin films. The figure shows the laser (5 mW), position sensitive detector, and magnets for applying field in parallel ($H_{\parallel}$) and perpendicular ($H_{\perp}$) directions to the sample.

As the magnetic field was applied along the in-plane directions of each sample, careful adjustments were made to ensure minimum contribution from torque is included in the displacement output. The torque effect, which is different from true magnetostriction, comes from the mutual misalignment between the direction of the magnetic field and the magnetization of the cantilever. This can cause the cantilever to deflect/displace even when there is no magnetostriction. To mitigate this, the cantilevers were adjusted until the cantilever/field angles was zero and the "wings" of the butterfly curve were flat. Figure 2.7 shows typical magnetostriction displacement /butterfly curves of a cantilever sample. The two bottom curves labeled initial and 1st adjustment illustrate the effect of torque while the green plot shows the near zero torque after the appropriate adjustments were made.

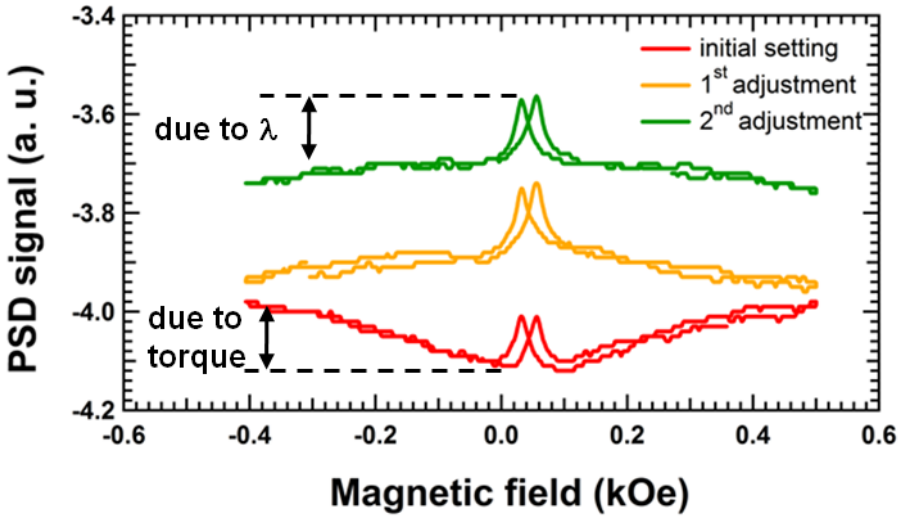

Figure 2.7 The effect of torque and the corrective adjustments during the measurement of magnetostriction. The bottom curve indicates a misalignment between the field and magnetization of the cantilever, while the middle and top curves are following successive adjustment steps showing reduction in torque. The green curve shows ideal alignment which exhibits a near zero torque.

Data taken from measurements similar to the green curve shown in Figure 2.7 above are used in the calculation of the magnetostriction. To obtain the overall magnetostriction in thin film samples, magnetic fields were applied parallel and perpendicular to cantilever's long axis and the resulting displacement are measured separately. Recent studies carried out on cantilever unimorphs have used the formulation of Lacheisserie to calculate magnetostriction[15,40,50-51], the same technique is used here. According to the Lacheisserie model, the raw parallel ($D_{\parallel}$) and perpendicular ($D_{\perp}$) displacements from measurements with two field directions can be converted to a magnetoelastic coupling constant (b) through the expression of du Tremolet de Lacheisserie and Peuzin[46]:

$$b = \frac{(D_{\parallel} - D_{\perp}) * E_s * t_s^2}{3 * E_f * L^2 * t_f * (1 + v_s)} \tag{1.9}$$

Here L is the sample length, E_f and E_s are Young's moduli of the film and substrate, t_f and t_s are their respective thicknesses, and v_f and v_s are their respective Poisson's ratios. $D_{\parallel}$and $D_{\perp}$ represent the displacement measured when the field is applied along the length and perpendicular to the cantilever, respectively.

The effective magnetostriction constant (λ_{eff}) can then be calculated from the magnetoelastic coupling constant by taking the ratio of the magnetoelastic coupling (b) with the shear coefficient (c) of the film, and the formula for magnetostriction becomes:

$$\lambda_{eff} = \frac{2(D_{\parallel} - D_{\perp}) E_s t_s^2 (1 + v_f)}{9 E_f L^2 t_f (1 + v_s)} \tag{2.0}$$

The λ_{eff} convention used reflects the fact that the measured overall magnetostriction is a convolution of the cubic constants (λ_{100} and λ_{111}) since the films studied here are either polycrystalline or textured.

For the case of polycrystalline samples the effective magnetostriction is given by[52]:

$$\lambda_{eff} = \frac{2}{5}\lambda_{100} + \frac{3}{5}\lambda_{111} \tag{2.1}$$

and the formula for a 110 textured sample is given as[52]:

$$\lambda_{eff} = \frac{1}{5}\lambda_{100} + \frac{4}{5}\lambda_{111} \tag{2.2}$$

where λ_{100} and λ_{111} are the cubic constants.

2.4.1: Measuring Young's modulus of the films

The elastic modulus (E_f) of the films is calculated by measuring the frequency of the first flexural mode of just the Si cantilevers, and then with the film deposited using a laser doppler vibrometer. This technique used to determine the Young's modulus of the films is similar to the one used in reference[53]. To account for non-uniformities in the Si cantilever thickness which resulted from the release procedure and estimated to be 0.01 μm, an effective thickness was calculated using Euler-Bernoulli beam theory[54]. Using the calculated thickness, the modulus of the deposited films can be determined from the following equation:

$$\frac{f_{uni}}{f_{bi}} = \frac{\frac{k_i \sqrt{\frac{h_s^2 E_s}{L^4 \rho_s}}}{4\sqrt{3}\,\pi}}{\frac{k_i \sqrt{\frac{h_f^4 E_f^2 + 4 h_f^3 h_s E_f E_s + 6 h_f^2 h_s^2 E_f E_s + 4 h_f h_s^3 E_f E_s + h_s^4 E_s^2}{L^4 (h_f E_f + h_s E_s)(h_f \rho_f + h_s \rho_s)}}}{4\sqrt{3}\,\pi}} \tag{2.3}$$

where E, h, ρ are the modulus, thickness, and density, respectively with subscript s and f denoting properties of the substrate and film respectively. The ratio of f_{uni} and f_{bi} is not fully simplified to show the full forms of the frequency equations where L is the length of the cantilever and k_i is the eigenvalue for the flexural mode (3.516 for the first mode). Error bars were calculated using the 95% confidence intervals for the Lorenzian fit of the resonant peaks at f_{uni} and f_{bi}. The extracted Young's modulus is then used to calculate λ_{eff} using equation (1.9).

2.5: Wave dispersive spectroscopy

The composition distribution of the combinatorial thin-film samples were accurately mapped using wavelength dispersive spectroscopy (WDS) on an electron microprobe (JXA-8900R). WDS is a non-destructive x-ray spectroscopic method for determining the atomic percentages of elements in unknown specimens. WDS is a widely used microprobe technique for obtaining quantitative composition analysis. The basic principle of this technique is that a focused electron beam (30 microns diameter) penetrates the unknown sample, and part of the energy of the incident electrons scatters as characteristic x-rays of particular elements. These emitted x-rays

which have a different wavelength depending on the elements present are filtered through selected x-ray spectrometers and analyzed. By detecting characteristic wavelengths of different elements, quantitative identifications of elements can be performed.

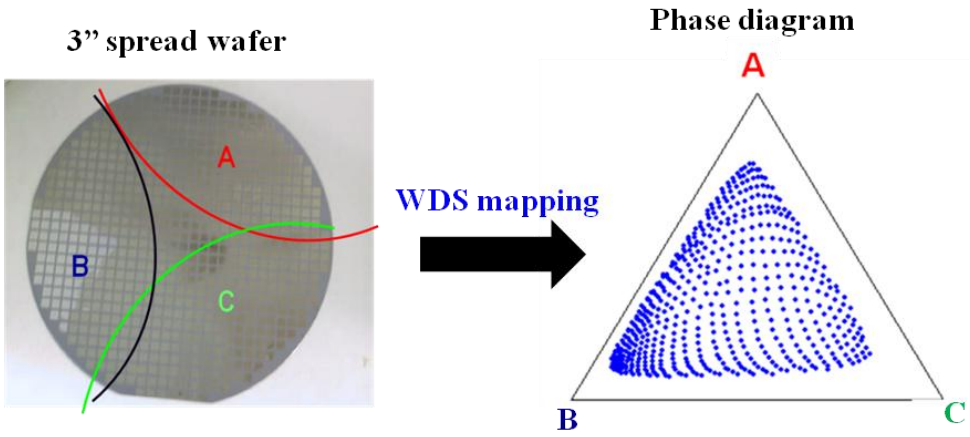

Figure 2.8 Illustration of the WDS mapping from a natural composition spread. left) projected areal coverage from 3 sputtering targets onto a 3" wafer, right) composition mapping via WDS onto a ternary phase diagram.

An example of the use of WDS to map regions of a ternary system is shown above in Figure 2.8. In this example, A, B, and C are three different elements. Each point on the composition spread wafer spread A-B-C has a different atomic percentage of each element. Each composition data point is projected onto a ternary A-B-C phase diagram. Phase diagram makes it easier to visualize hundreds of compositions and their characteristic properties.

2.6: Structural Identification

The crystal structures of the films were characterized via synchrotron X-ray micro-diffraction and high resolution transmission electron microscopy. In the next few pages I will discuss these very important characterization techniques.

2.6.1: Synchrotron microdiffraction

Synchrotron micro-diffraction is an X-ray analysis tool which uses synchrotron radiation emitted by relativistic electrons in a cyclotron (high intensity X-ray) to study structural details of materials. The lattice parameters of the thin film samples in this study were characterized using synchrotron X-ray micro diffraction at the 11-3 beam line at the Stanford Synchrotron Radiation Lightsource user facility at the SLAC National Accelerator Laboratory. In these studies (Figure 2.9), each diffraction measurement was recorded at room-temperature on an image plate detector (MAR 345) with an exposure time of 30 seconds, long enough to obtain sufficient diffracted intensity for complete lattice parameter analysis. The beam size was focused to 15×15 μm^2, the photon energy used was 12.7 keV, and the incident angle (ω) of the beam was set at 5^o. Figure 2.10 shows a picture of the inside of the hutch, where all measurements were performed. The diffraction peak positions of the raw data were normalized using the National Institute of Standards and Technology CeO_2 standard powder. High resolution d-spacings were extracted from the integrated diffraction patterns of the different compositions using fit2d software (www.esrf.eu/computing/scientific/FIT2D/. To identify the detected phases,

comparisons were made to databases of known phases using Pauling Files binaries, DIFFRACPLUS software from Bruker, and the Pearson's Crystal database.

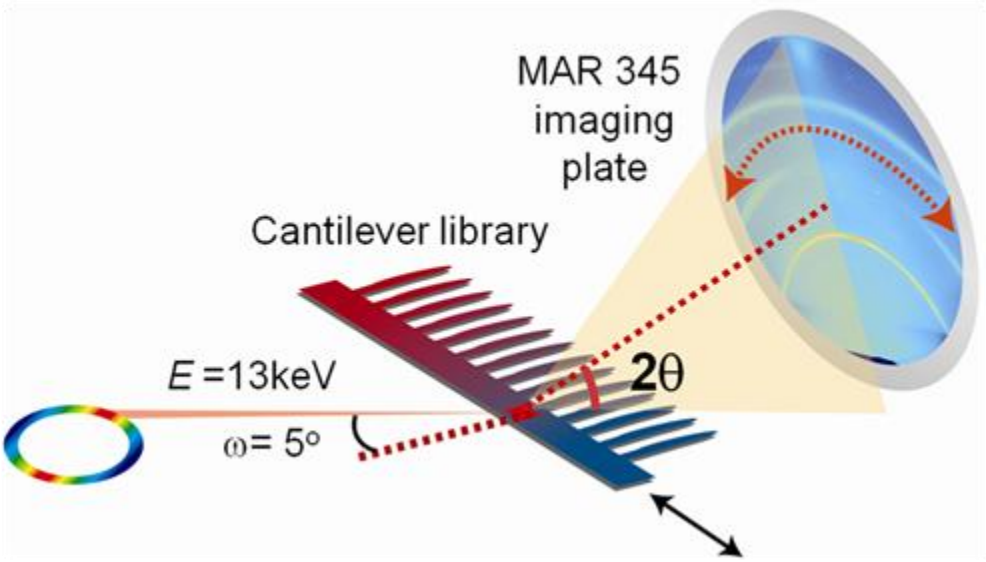

Figure 2.9 Schematic of synchrotron measurement on cantilevers.

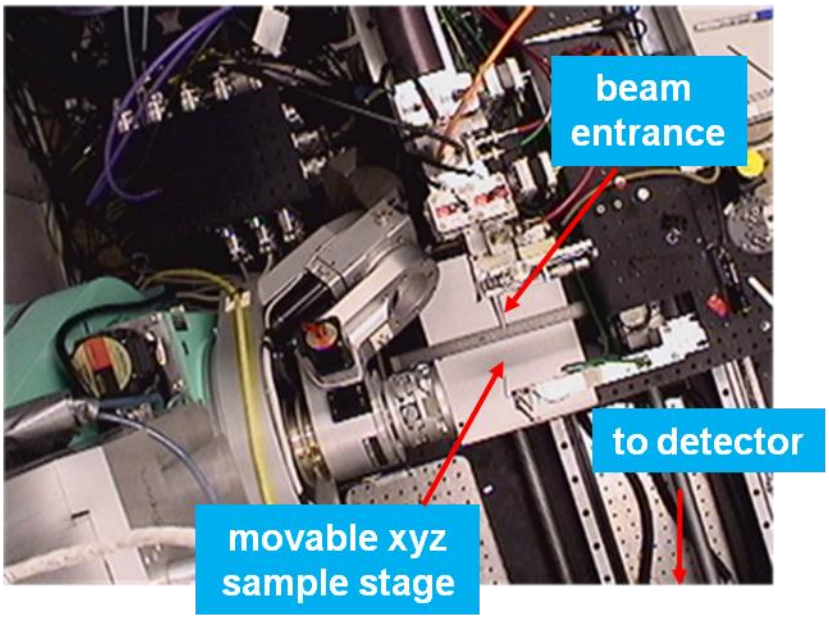

Figure 2.10 Actual picture of the inside of the hutch at the user facility of Stanford Synchrotron Radiation Lightsource of SLAC.

2.6.2: Transmission electron microscopy

Transmission electron microscopy (TEM) is performed on as-deposited and annealed films to determine their microstructure. All investigations were carried out on a JEOL TEM-3010UHR microscope operated at 300 kV. High resolution d-spacings are extracted from the integrated diffraction patterns of the different compositions.

In principle, a TEM operates much like an optical microscope except that optical microscopes use light sources and glass lenses, while TEMs use electron sources and electromagnetic lenses. During operation, electrons are emitted from a filament at very high accelerated voltage (100 kV – 1000 kV) then focused through a high resolution set of condenser lenses onto the specimen. The electron beam is scattered by the specimen and the diffracted beams are brought into focus by an objective lens on a focal plane to form a diffraction pattern. Some of the common diffraction imaging techniques are: conventional imaging (bright-field and dark-field), selected area electron diffraction (SAED), convergent-beam electron diffraction (CBED), phase-contrast imaging (high resolution TEM, HRTEM), and Z-contrast imaging.

In addition, to the diffraction and spatial imaging, spectroscopic techniques such energy-dispersive x-ray spectroscopy (EDS) and electron energy-loss spectroscopy (EELS) can be performed. The latter techniques use the electronic excitations of the atoms in the specimen. In this work, bright-field and dark-field imaging, SAED, and TEM was used to characterize the microstructures, and EDS was used to study the chemical compositions in the films.

2.6.3: Scanning electron microscopy (SEM)

Since the thickness of the magnetic layer influences the bending motion of the cantilevers which affects the saturation magnetostriction, it is very important to get an accurate measurement of the film thickness. To this end, the film thicknesses of the composition spreads were measured using cross-sectional scanning electron microscopy (SEM). The cantilevers were broken off at their bases and inserted into the SEM tool with the broken end exposed to the electron gun. The electron probe scans across the cross-section to the cantilever to give high resolution image such as that seen in Figure 2.12. In this figure, the magnetostrictive film, the insulating layer (Si/SiO2), and the substrate (Si) can be clearly seen. All measurements are carried out on a Hitachi SU-70 ultra-high resolution analytical SEM equipment.

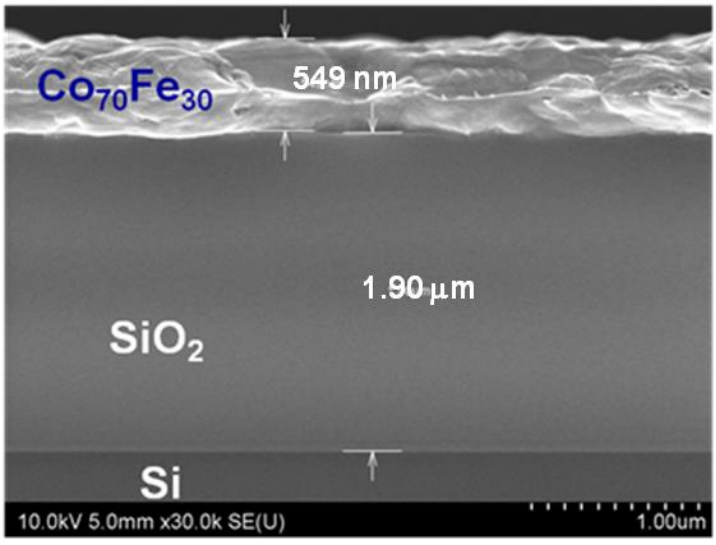

Figure 2.11 Actual SEM image taken from a magnetostrictive thin film sample. Here, the magnetostrictive film, the insulating Si/SiO2 and substrate are clearly visible.

Chapter 3 Magnetostriction in Fe-Ga alloys

Overview

This chapter discusses magnetostrictive properties in rare-earth free Fe-Ga alloys. Fe-Ga was one of the first Fe-based alloys to show promise as large magnetostrictive material. This also serves as one of the motivations behind investigating magnetostriction in other alloys such Co-Fe which will be discussed in the following chapter. It begins with a brief introduction to the Fe-Ga alloys and in particular how the discovery of Galfenol has inspired other research. This is followed by a discussion on thin-film magnetostriction in Fe-Ga, followed by results on magnetization and microstructural studies on Fe-Ga thin films. This study on Fe-Ga thin films is an extension of Jason Hattrick-Simpers PhD thesis (2007) work.

3.1: Introduction to Fe-Ga binary alloys

Single crystal iron (α-Fe) at room temperature has a body centered cubic (BCC) unit cell which is equivalent to an A2 disordered structure in the strukturbericht notation[55]. In an A2 structure, each lattice point has a compositionally weighted equal probability of having an iron or gallium atom. The bulk Fe-Ga phase diagram (Figure 3.1b) shows that the α-Fe or A2 phase exists up to 12 atomic percent Ga while the α-Fe_3Ga ($L1_2$) ordered FCC phase exists between 25 and 30 atomic percent Ga[55]. The region between 12 and 25 atomic percent Ga consists of a mixture of these two phases. Other phases such as $D0_3$ (ordered FCC), B2 (ordered BCC), and β-Fe_3Ga ($D0_{19}$) only exists at temperatures above 650 ^oC. Extensive work on the Fe-

Ga phase diagram showed that the structural properties of these alloys are thermal history-dependent, they display complex meta-stable phases which influence their magnetic properties[56-58]. For more details on the Fe-Ga phase diagram, all is referred to Ref[6].

3.2: Magnetostriction in Fe-Ga alloys

Bulk

R. C. Hall showed that substitution of Al for Fe leads to increase magnetostriction of more than five times that of pure Fe[59]. Clark *et al* later found that alloying Fe with 20 at.% Ga in single crystal $Fe_{1-x}Ga_x$ alloys yields an even larger magnetostrictive tetragonal strain of 3/2 $\lambda_{100} \geq 400$ ppm (Figure 3.1a). The quantity λ_{100} is the magnetostriction coefficient with the field applied in the [100] crystallographic direction of the sample[60]. These alloys also show good mechanical properties at low fields[61]. Such characteristics have made Fe-Ga alloys attractive alternatives to existing rare-earth based magnetostrictive materials such as Terfenol-D, which despite its large magnetostriction > 1000 ppm[7], has large magnetocrystalline anisotropy and low workability due to its brittleness.

One of the striking features of the $Fe_{0.8}Ga_{0.2}$ alloy is the phase condition under which enhancement in magnetostriction occurs: a disordered body-centered-cubic (bcc) α-Fe (or A2) phase formed due to quenching is in metastable equilibrium with a $D0_3$ (ordered bcc) phase[62-65]. A proposed model for magnetostriction in $Fe_{1-x}Ga_x$ suggests that the $D0_3$ nanoclusters embedded in the A2 matrix give rise to a magnetic field induced rotation leading to the large magnetostriction[66].

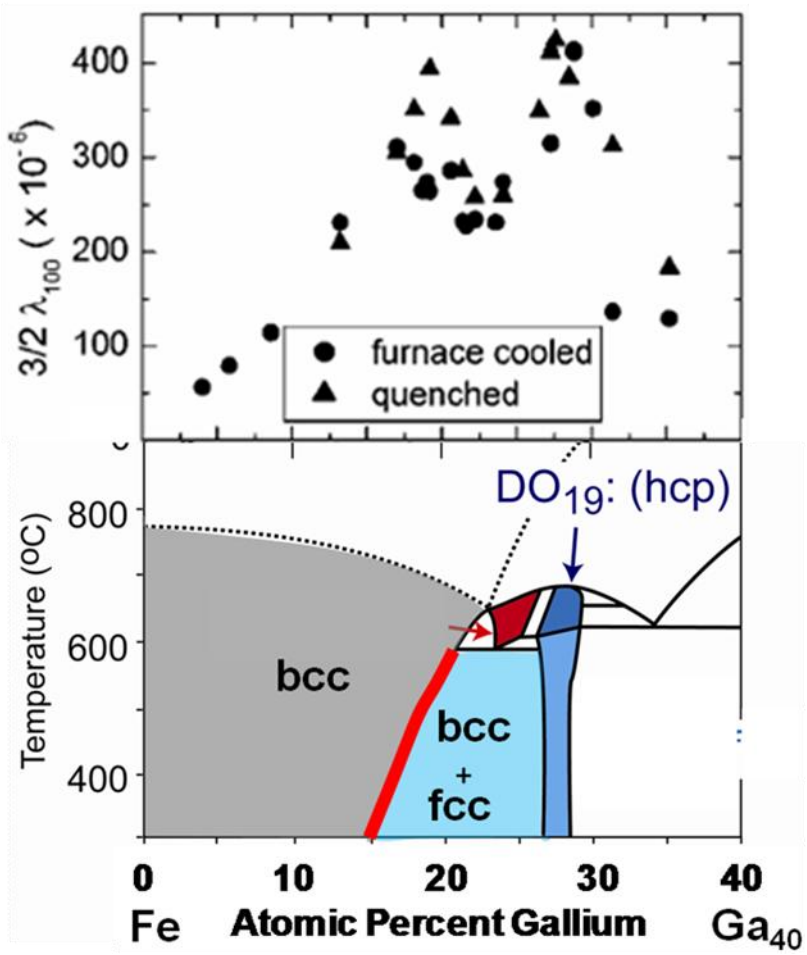

Figure 3.1 **Magnetostriction in bulk single crystal Fe-Ga alloys[62] and a portion of the Fe-Ga phase diagram[55] showing that the peak in magnetostriction occurs at the phase boundary of $D0_3$/A2 phases.**

It is quite remarkable that substituting non-magnetic Ga atoms for Fe can induce such an enormous magnetostrictive strain, to more than ten-fold increase from that of pure Fe (λ_{100} ~25 ppm for pure Fe to $\lambda_{100} \geq 400$ in $Fe_{0.8}Ga_{0.2}$). While the investigation continues as to whether the mechanism of magnetostriction is conventional Joule magnetostriction due to spin-orbit coupling[67-68] or driven by a structural change[69], applications of Fe-Ga for sensing and transducers are being explored[70-74]. However, these alloys are known to display fatigue rather easily[75-78],

and thus strain minimization is important. This is particularly true for thin films where strain-free growth is desirable[79-80].

To address this issue in thin films, we investigated the magnetic and structural properties of $Fe_{1-x}Ga_x$ ($0 \leq x \leq 45$) films grown on Si/SiO_2 substrates and demonstrated that films can be grown with minimal stress while still exhibiting reasonably large magnetostriction. Composition spread thin films of Fe-Ga where the composition continuously change were co-sputtered using a pure Fe target and an intermetallic Fe_2Ga_3 target, at 75 and 40 W, respectively in an ultra-high vacuum sputtering chamber described in Chapter 2.2. The binary composition spreads were deposited on arrays of Si/SiO_2 cantilevers at room temperature. In this study no post-deposition annealing was carried out.

Thin films

Magnetostriction measurements on as-deposited Fe-Ga binary composition spread alloys were performed using the cantilever method described in Chapter 2.3. Each cantilever is 10 mm long, 2 mm wide, and approximately 70 μm thick. Only the first three rows of the composition spreads were measured to ensure film thickness uniformity in the cantilevers. Displacement measurements were recorded for magnetic fields applied parallel (Dpara) and perpendicular (Dperp) to each sample. Figure 3.2 shows the displacement profiles obtained from the two field direction for the entire spread at different at.% Ga. The values from the Dpara-Dperp plot were inserted in equation (2.0) to calculate the effective magnetostriction. Figure 3.3 shows

the results of the effective magnetostriction measurements as function of atomic percent gallium in the cantilever sputtered thin films. The figure shows two plots of highly reproducible data taken from different wafers over a one year time frame. As seen, two peaks of magnetostriction at high Ga contents are present at ~ 24 and 34 at.% Ga. Though the peak positions are slightly shifted from those reported in bulk, these results are consistent with previous thin film results using an identical technique[40,50], and have already been shown to correlate well with the bulk compositional trends[62]. I will not focus much on the magnetostriction aspect of these Fe-Ga films as extensive work has been carried out by Hattrick-Simpers (2007 PhD Thesis), but rather I will discuss the magnetization and structural properties which provides useful and important parameters for their applications.

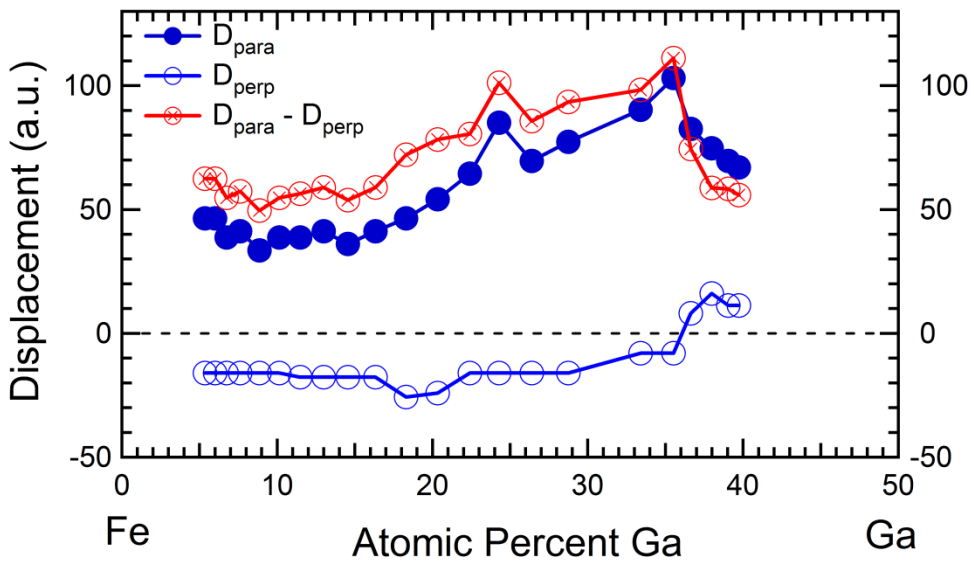

Figure 3.2 Cantilever displacement profiles for magnetic field applied in two directions: parallel (Dpara) and perpendicular (Dperp) to the samples. The values from (Dpara-Dperp) was used in equation (2.0) to calculate the effective magnetostriction.

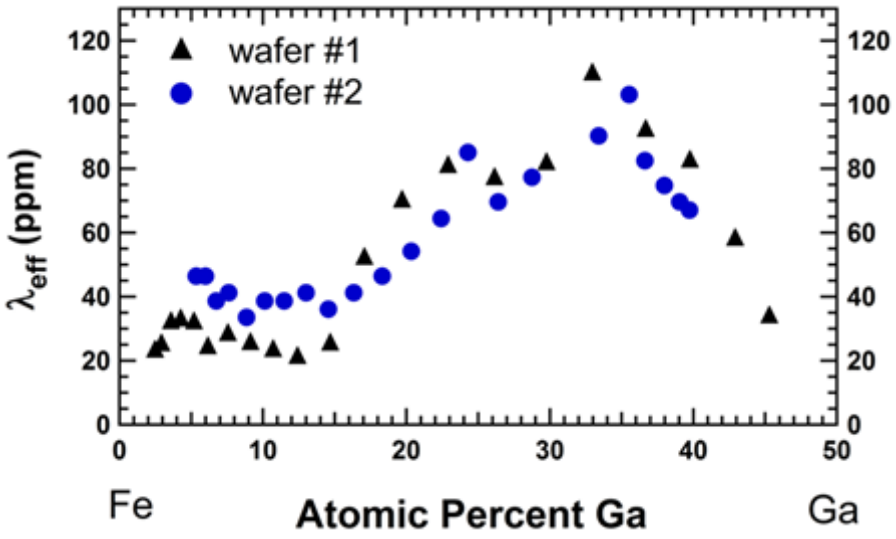

Figure 3.3 Compositional dependence of magnetostriction of Fe-Ga thin film alloys. Results from two different wafers made 1 year apart are shown indicating good reproducibility in the experiment.

3.3: Magnetization

The magnetization in the Fe-Ga films was measured using a vibrating sample magnetometer (VSM). Hysteresis loops of the films were taken at each composition and the measured magnetic moment values is converted to magnetization. Figure 3.4 shows the magnetization results of the Fe-Ga films along with bulk data[81]. As seen from the figure, the magnetization value remains high and close to that of pure Fe (bulk ~1740 emu/cc) with up 15 atomic percent Ga substitutions, after which the magnetization decreases sharply with increasing Ga content. The lower magnetization of the thin films data might be due pinning of the magnetic moments which is caused by grain boundaries and defects. However, in a qualitatively manner the trend of the thin-film is similar to that of the bulk.

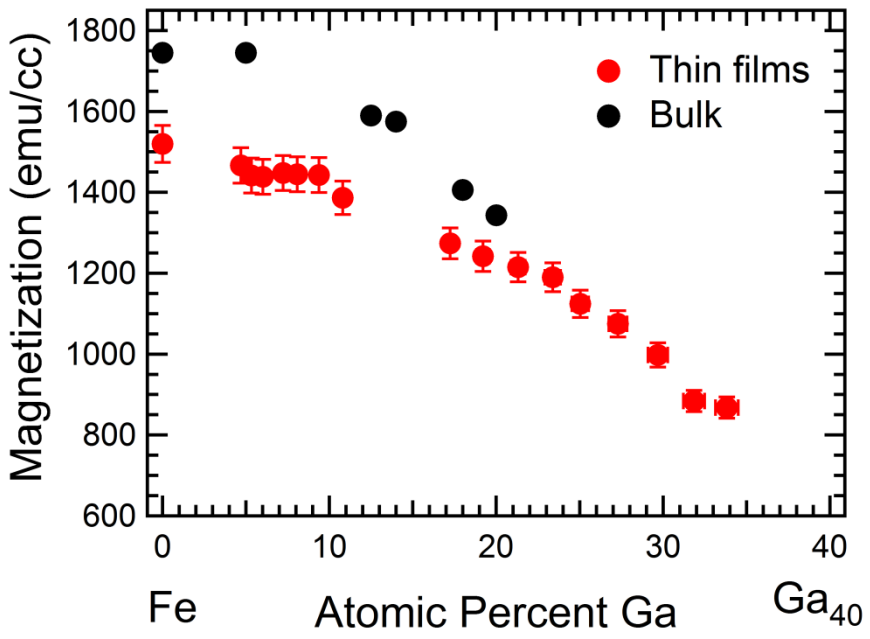

Figure 3.4 Comparison of magnetization in bulk and thin-films. Bulk data was taken from Ref[81].

3.4: Microstructure of Fe-Ga films

To investigate the microstructure in the films, we have performed high-resolution synchrotron X-ray micro-diffraction measurements on as-deposited samples with gallium content between 19 and 43 %, as shown in Figure 3.5. Previous thin film studies on Fe-Ga have shown that the sputtered films are polycrystalline, with slight evidence of [100] texturing, having grain sizes of about 30 nm[40]. From the figure, there are two strong reflections at 2θ = 24 and 41 degrees, corresponding to bcc (110) and bcc (200) peaks, respectively, for > 25 at.% Ga. At these Ga concentrations, the ordered DO_3 and B_2 phases are more pronounced. Above 25 at.% Ga, we see the emergence of an ordered phase with (111) reflection at ~ 2θ = 33

degrees. The onset of this ordered phases corresponds with the peak in magnetostriction (□□ at ~ 25 at.% Ga [65,77]. However, there is no apparent structural correlation with the other known maximum in magnetostriction at Ga at.% ~ 34.

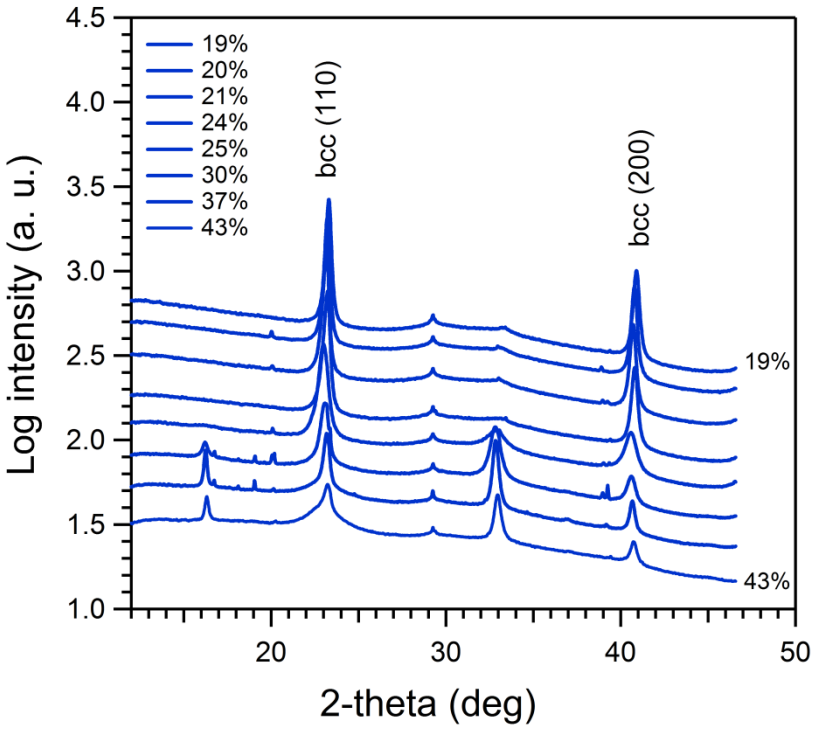

Figure 3.5 Synchrotron X-ray micro-diffraction patterns for different at.% Ga compositions in Fe-Ga thin film samples.

3.6: Conclusion

In summary, we have grown $Fe_{1-x}Ga_x$ films on Si/SiO_2 and investigated the magnetic and structural properties by combinatorial methods. We found that the nearly zero stress observed at ~ 35 at.% Ga is coincident with the minimum in the tetragonal elastic modulus c', which gives rise to a local maximum in the magnetostriction λ_{eff} ~

100 ppm as a function of at.% Ga. Synchrotron diffraction measurements showed that for at.% Ga > 25, the emergence of the ordered DO_3 phase is responsible for the maximum in magnetostriction. The observation of strain-free high-magnetostriction films not only presents many opportunities for practical applications but can also be used to provide insight into the physical mechanism of the phenomenon.

Chapter 4: Magnetostriction in Co-Fe binary alloys

Motivation

Since the discovery of large magnetostriction in $Fe_{1-x}Ga_x$ alloys a decade ago, intense research have been dedicated to deciphering the origin of its unusually large magnitude. Although these alloys show good mechanical properties at relatively low fields[61] as compared to large magnetostrictive high field Terfenol-D, they are still quite brittle. These facts sparked considerable research effort to alloy Fe-Ga with a suitable ternary element in hopes to increase its workability. One of the striking features about the $Fe_{0.8}Ga_{0.2}$ alloy is the phase dynamics under which enhancement in magnetostriction occurs: a disordered body-centered-cubic (bcc) α-Fe (or A2) phase is in metastable equilibrium with a $D0_3$ (ordered bcc) phase[64]. A proposed model for $Fe_{1-x}Ga_x$ suggests that the $D0_3$ nanoclusters embedded in the A2 matrix give rise to a magnetic field induced rotation leading to the large magnetostriction[66]. Also, in the previously studied Fe-Al alloy system, a significant increase in magnetostriction was observed in compositions at the $D0_3$/A2 phase boundary.

An emerging trend then is that magnetostriction enhancement in some Fe-based systems occurs for compositions near structural phase boundaries[82]. It is of fundamental interest to identify new alloys with large magnetostriction and to help understand the origin of magnetostriction enhancement. Here, we investigated the Co-Fe system with a focus on the (fcc+bcc)/bcc phase boundary around the $Co_{0.75}Fe_{0.25}$ composition.

4.1: Introduction to Co-Fe thin film alloys

The bulk Co-Fe phase diagrams[83-84] (Figure 4.1), show that the α-Fe bcc phase exists at higher temperatures for all compositions. At temperatures lower than 912 ^{o}C and Co concentrations > 50 at.%, the bcc phase intersects with a mixed phase region of face-centered-cubic (fcc) Co and bcc Fe phases. Applying the scenario described above for the $Fe_{0.8}Ga_{0.2}$ alloy, it is at this (fcc+bcc)/bcc boundary that the enhancement of the magnetostriction would be expected to occur.

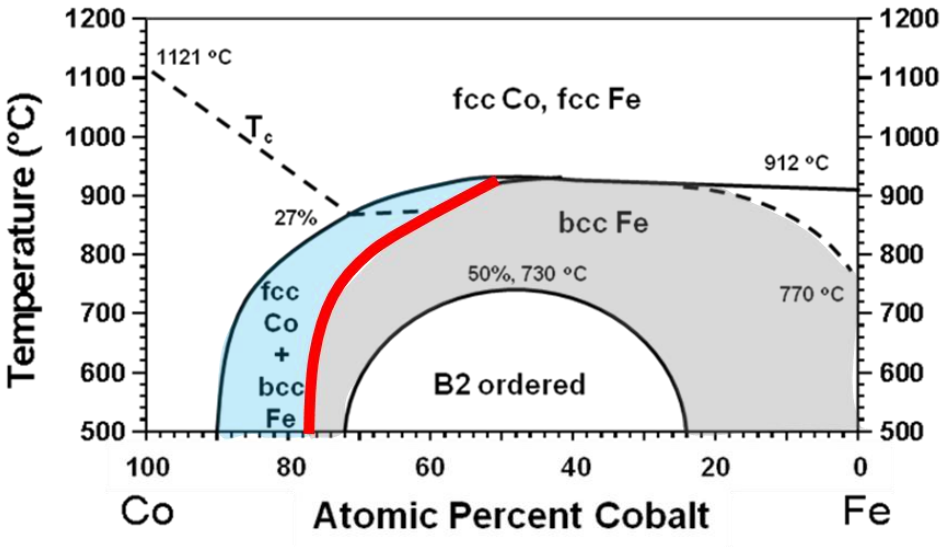

Figure 4.1 Co-Fe phase diagram[83] showing the mixture phases and single phases. The red solid line indicates the phase boundary where enhancement of magnetostriction is expected to occur.

Early bulk studies introduced the Co-Fe alloy system as a highly magnetostrictive material, exhibiting two peaks of magnetostriction; one at the $Co_{0.7}Fe_{0.3}$ and the other near the equiatomic compositions of Fe and Co[85-86]. Later

experiments by Hall on bulk single crystal $Fe_{.50}Co_{.50}$ alloys suggested that the increase in magnetostriction was due to a near zero anisotropy and strong B2 ordering that develops during processing of the alloy[59,87]. Since then, several studies on alloys of the 50:50 composition in bulk and thin films have been reported[9-10,12,51,88-89], but very little attention has been given to the other compositions. In a recent bulk experiment (unpublished), λ_{sat} of 150 ppm was achieved in a post annealed homogenized arc-melted $Co_{0.7}Fe_{0.3}$ alloy[90], igniting interest in this alloy's high magnetostrictive potential and leading to the present investigation.

In this work, we investigated the magnetostrictive and micro-structural properties in $Co_{1-x}Fe_x$ alloy thin films prepared using the combinatorial composition spread approach. High-throughput measurements were performed on as-deposited and annealed (cooled at different rates) composition spread films spanning a composition range from $Co_{0.9}Fe_{0.1}$ to $Co_{0.1}Fe_{0.9}$ to study their magnetostriction.

4.2: Thin- film preparation (As-deposited and annealing)

Co-Fe thin film composition spread samples were fabricated in a manner described in Chapter 2.2. Pure Co and Fe targets were deposited at room temperature on cantilever substrates to obtain composition variation as shown in Figure 4.2. Some of the samples were annealed at 800C for 1hr then slow-cooled or water-quenched to achieve annealed samples. As previously reported in single crystal bulk Fe-Ga, annealing can lead to significant enhancement in the magnetostrictive properties.

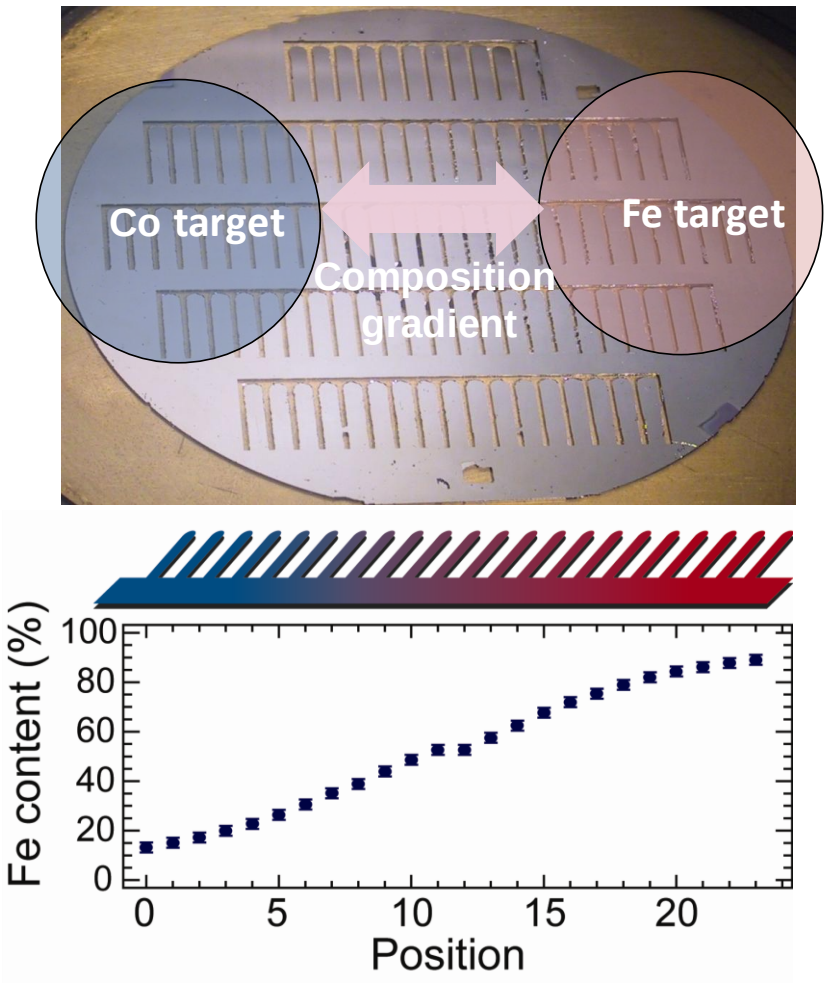

Figure 4.2 Illustration of Co-Fe thin-film composition spread. Top) shows the targets and projected coverage area of binary composition spread. Bottom) composition variations as one traverse the diameter of the wafer.

4.3: Magnetostriction results on Co-Fe thin film alloys

The measured effective magnetostriction as a function of atomic composition for the as-deposited state (black circles), and two references of previous work is shown in Figure 4.3. The room temperature as-deposited composition spread shows that as Co is substituted for Fe, two composition regions with enhanced magnetostriction appear. The first region is centered around the well-studied

$Co_{0.5}Fe_{0.5}$ composition and reaches a maximum magnetostriction of 67 ± 5 ppm at $Co_{0.44}Fe_{0.56}$, while the maximum value of the second enhanced region is 84 ± 5 ppm near $Co_{0.73}Fe_{0.27}$, in the vicinity of the phase boundary of (fcc+bcc)/bcc of the Co-Fe phase diagram shown in Figure 4.1. This composition trend is similar to the one reported for bulk materials where two peaks of magnetostriction were observed near the $Co_{0.5}Fe_{0.5}$ and $Co_{0.7}Fe_{0.3}$ compositions[85-86]. The magnetostriction value of 67 ppm obtained for our $Co_{0.5}Fe_{0.5}$ films is in good agreement with previous polycrystalline thin film[9] and bulk[91] reports as shown in Figure 4.3.

Figure 4.4 shows the magnetostriction as a function of atomic percent Co after two thermal treatments; one which was annealed for 1 hour at 800 ^{o}C and slow-cooled (blue circles), and the other which was annealed for 1 hour at 800 ^{o}C and water-quenched (red circles). The as-deposited composition spread is also included for comparison. The annealed and slow-cooled spread (blue circles) shows a significant increase in magnetostriction over the majority of the composition range studied here, and the two broad peaks of magnetostriction observed in the as-deposited sample have now shifted to lower Co content by a few at.%. The maximum magnetostrictions are now 103 ± 6 ppm and 156 ± 7 ppm for compositions of $Co_{0.4}Fe_{0.6}$ and $Co_{0.66}Fe_{0.34}$, respectively, in the slow-cooled spread.

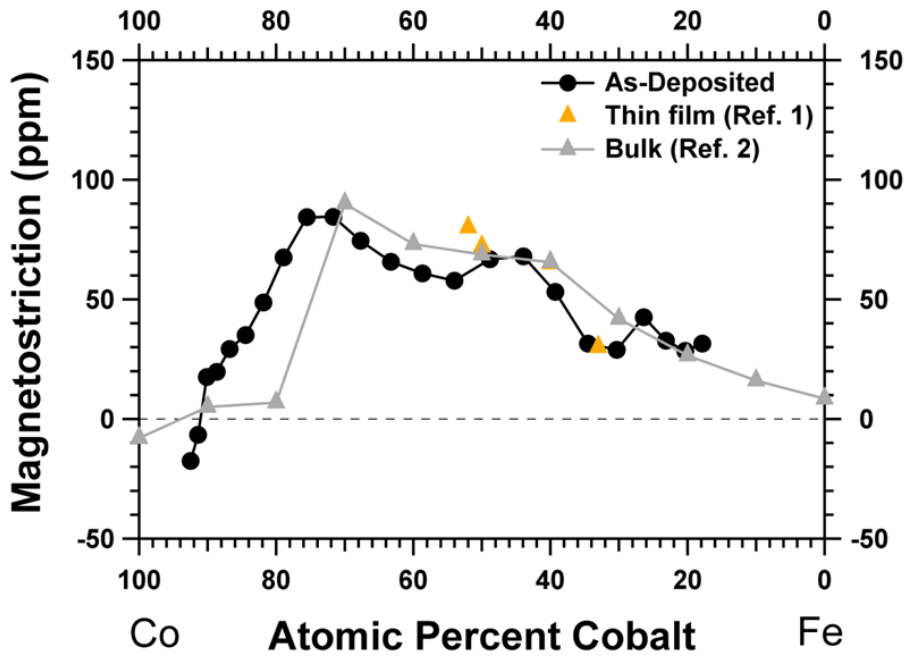

Figure 4.3 Magnetostriction in $Co_{1-x}Fe_x$ alloys, of as-deposited films and comparison with an earliest bulk report[85] and recent thin film reports[9]. As seen from the figure, our thin-film data agree well with previous results.

Annealing and quenching the spreads (red circles) leads to an even larger enhancement in magnetostriction over a large composition range. There are two noticeable features about this heat treatment. First, starting from about $Co_{0.18}Fe_{0.82}$ as more Co is substituted for Fe, the magnetostriction increases steadily up to 180 ppm and a broad plateau is observed in magnetostriction for compositions between 38 and 56 at.% Co. Upon further increase in Co content, the magnetostriction value rises to an unusually high level between 60 and 75 at.% Co with a maximum magnetostriction of 260 ± 10 ppm at the $Co_{0.66}Fe_{0.34}$ composition. Beyond $Co_{0.75}Fe_{0.25}$, the magnetostriction drops precipitously as more Co is added and becomes negative at compositions > 82 at.% Co. At the $Co_{0.66}Fe_{0.34}$ composition, the magnetostriction of the annealed and water-quenched sample is more than three times

the as-deposited value. Two repeat experiments with the same thermal processing have resulted in the same magnetostriction values across the spread. We have confirmed that the composition distribution across the spread remains unchanged after thermal treatment. A comparison plot of the magnetostriction and the corresponding phase diagram is presented in Figure 4.5.

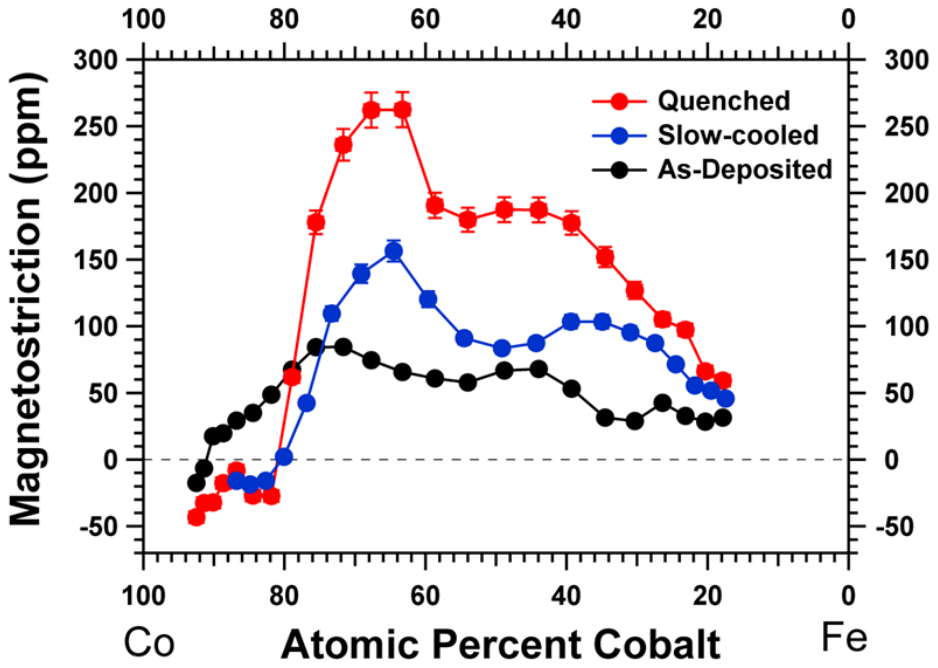

Figure 4.4 Magnetostriction in $Co_{1-x}Fe_x$ alloys from different synthesis conditions. black) as-deposited, blue) annealed and slow-cooled, and red) annealed and water-quenched.

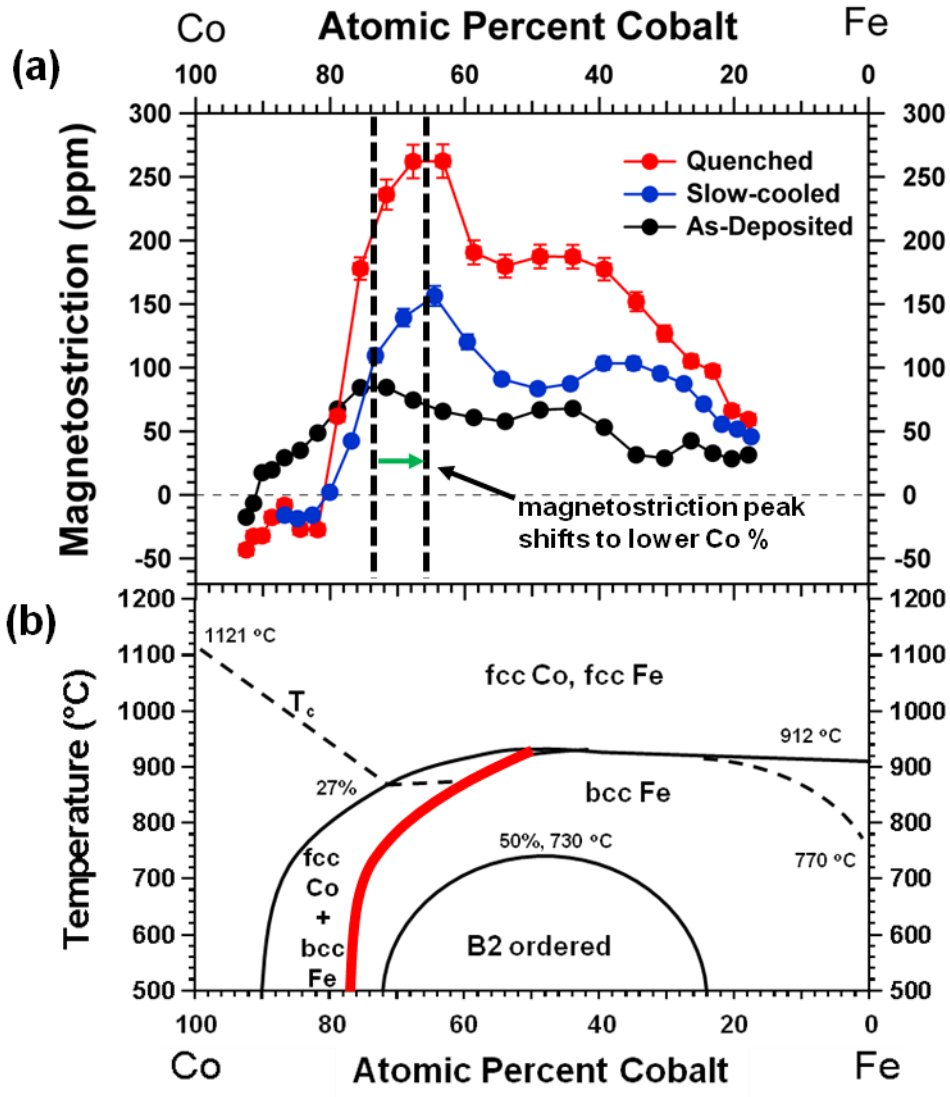

Figure 4.5 a) Magnetostriction vs. atomic percent cobalt for $Co_{1-x}Fe_x$ composition spreads with three heat treatments: as-deposited (black dots), annealed and slow-cooled (blue dots), annealed and water-quenched (red dots). The two dotted lines indicate the compositions of maximum magnetostriction for the as-deposited and annealed samples. b) Co-Fe phase diagram. The thick red solid line indicates the (fcc+bcc)/bcc boundary at which the enhancement of magnetostriction was found to occur.

4.4: Microstructure of Co-Fe thin films

The microstructure in the present Co-Fe films were determined using a variety of techniques. These results are discussed in the next few sections.

4.4.1: Synchrotron micro-diffraction

To explore the structural origin of this enhancement in magnetostriction, synchrotron X-ray micro-diffraction was carried out on the three composition spreads to map their phase distribution. Figure 4.6 shows density plots of the measured d-spacings as a function of atomic composition for the (a) as-deposited, (b) annealed and slow-cooled, and (c) annealed and water-quenched samples. In Figure 4.6a **(**as-deposited spread), a dominant α-Fe (110) phase spans almost the entire Co-Fe composition range studied here. The bcc phase is maintained to compositions with Co concentration as high as 90 %. However, near 78 at.% Co, a weak reflection between *d* ~2.05 Å and *d* ~2.10 Å, corresponding to the fcc (111) reflection of fcc β-Co begins to appear. The two phases co-exist (mixed phase) over a few at.% Co concentration as indicated in the figure. Note that the composition where the β-Co (111) peak first appears (Co 78 at.%) is coincident with the composition that shows the largest magnetostriction in the as-deposited film (Figure 4.3).

Figure 4.6b shows the diffraction data for the same composition spread after it was annealed at 800 ˚C and slow-cooled. The peak near 2.01 Å that was prominent in the as-deposited state remains, but the full width half max value for the reflection is half of the as-deposited value, indicating a well crystallized bcc (110) phase peak. However, the most striking feature in this figure is the fcc (111) β-Co peak at *d* ~2.05

Å. This peak which was weak and broad in the as-deposited state has now evolved into a well pronounced peak and extends further into the Fe-rich region (up to 30 at.% Fe). The growth of this fcc phase during the anneal has resulted in a broader composition region of two-phase mixture compared to the as-deposited state. More importantly, there is a shift in the (fcc+bcc)/bcc phase boundary to lower Co content (≈ Co 66 at.%), and this composition is again coincident with the composition which shows the highest magnetostriction (Figure 4.4).

Figure 4.6c shows the density diffraction plot of the annealed and water-quenched composition spread samples. In structure, it mirrors the slow-cooled spread, and a well defined (111) β-Co peak overlaps with the (110) α-Fe peak to create an fcc Co + bcc Fe phase mixed region, and the phase boundary is shifted to approximately 66 at.% Co. This result closely follows the Co-Fe phase diagram (Figure 4.5) in which the red-line indicating the (fcc+bcc)/bcc phase boundary trends towards lower Co content as the temperature is increased. The key finding here is that in the slow-cooled and the quenched spreads, the maximum enhancement of magnetostriction occurs at the (fcc+bcc)/bcc phase boundary which is where the fcc phase first appears. The peak seen in all three spreads at 2.10 Å results from an oxidized thin surface layer of CoO (T_N = 287 K), which does not contribute to the room temperature magnetic properties discussed here.

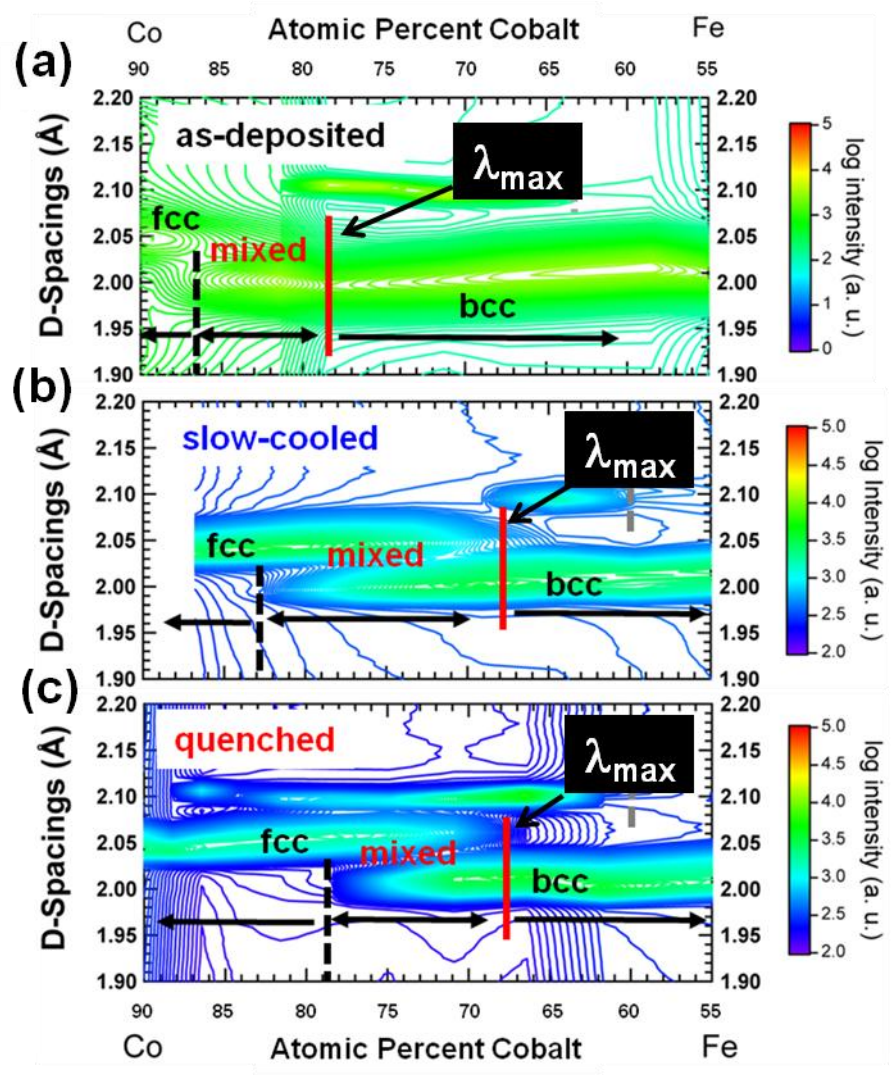

Figure 4.6 Synchrotron microdiffraction of a) as-deposited, b) annealed and slow-cooled, c) annealed and water-quenched composition spread samples. The diffracted intensity is presented in color code to the right of each plot. The red line marked "λ_{max}" in each spread indicates the approximate composition of the (fcc+bcc)/bcc phase boundary. This is also the composition of maximum magnetostriction.

4.4.2: TEM

To elucidate further correlation between the crystal structure and the magnetostriction properties, three magnetostrictive $Co_{.66}Fe_{.34}$ composition thin film samples (as-deposited, slow-cooled, and quenched) were analyzed by transmission electron microscopy (TEM). A low magnification cross-sectional image of this sample is shown in Figure 4.7.

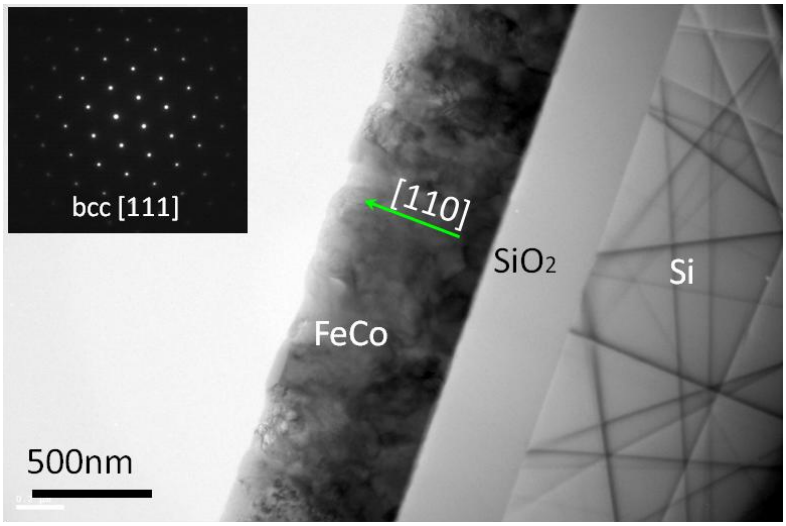

Figure 4.7 Low magnification cross-sectional TEM image of a Co-Fe sample. The image shows the film, insulating layer, and Si substrate.

Figure 4.8a shows a dark-field image of the (011) reflections from the selected area electron diffraction (SAED) pattern (Figure 4.8b) of the as-deposited sample. The image shows a microstructure consisting of randomly oriented nano-sized polycrystals of an average grain size ~ 10 nm. The SAED pattern of Figure 4.8b reveals diffraction rings indicative of the random crystallographic orientations of the

nano-grains of the as-deposited state. All diffraction rings are identified as that of a bcc structure consistent with the synchrotron data in Figure 4.6a.

Figure 4.8c and 4.8d is a bright-field image and the SAED pattern, respectively, of a sample which was quenched following an anneal at 800 ^{o}C. Compared with Figure 4.8a, Figure 4.8c shows a much coarser structure with grain sizes up to ~ 100 nm. The corresponding SAED pattern taken over a large area shows that in addition to the expected bcc reflections, a second phase is present. Detailed SAEDs from individual grains labeled "A" and "B" in Figure 4.8c of the annealed sample were identified to be bcc (Figure 4.8e) and fcc (Figure 4.8f), respectively. Further analysis by EDS (not shown) on theses grains revealed that the bcc phase is Fe-rich and the fcc phase is Co-rich, consistent with the Co-Fe phase diagram and synchrotron results of Figures 4.5b and 4.6c, respectively.

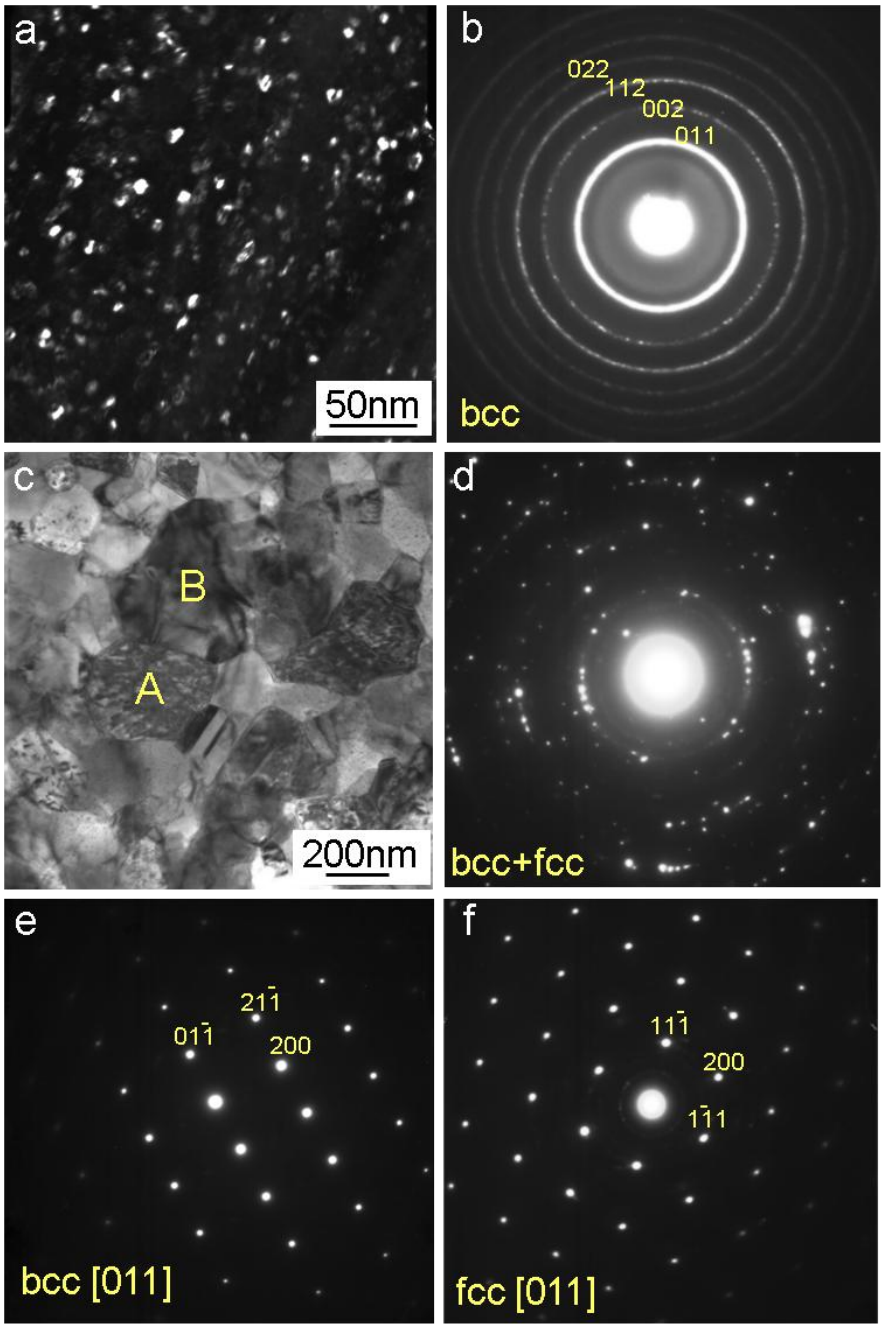

Figure 4.8 TEM images of $Co_{0.66}Fe_{0.34}$: a) (110) dark field image of as-deposited, b) SAED of as-deposited, c) bright field image of annealed, d) annealed SAED pattern of (c) using ~ 1.5 micrometer diameter aperture showing the mixture structure of bcc and fcc phases, e) [011] bcc diffraction pattern from grain "A" in (c), and f) [011] fcc diffraction pattern from grain "B" in (c).

To better understand the relationship between the cooling process and the magnetostriction properties, a detailed TEM analysis was performed on individual grains from both slow-cooled and quenched samples. Figure 4.9a displays an image of a bcc grain from the slow-cooled sample with a composition of $Co_{0.66}Fe_{0.34}$ and a λ_{eff} of 156 ppm. The four weak inner reflections in the SAED pattern of this grain, shown in Figure 4.9b, indicates a beam direction of [001] onto a highly ordered B2 structure. In contrast, the image and SAED pattern (Figure 4.9c and 4.4.2-3d) of a quenched sample of the same composition whose λ_{eff} is 260 ppm shows no diffracted [100] spots and thus no evidence of ordering. This demonstrates that ordering suppresses magnetostriction and is the reason for the reduced magnetostriction observed in the slow-cooled samples as compared to the water-quenched samples.

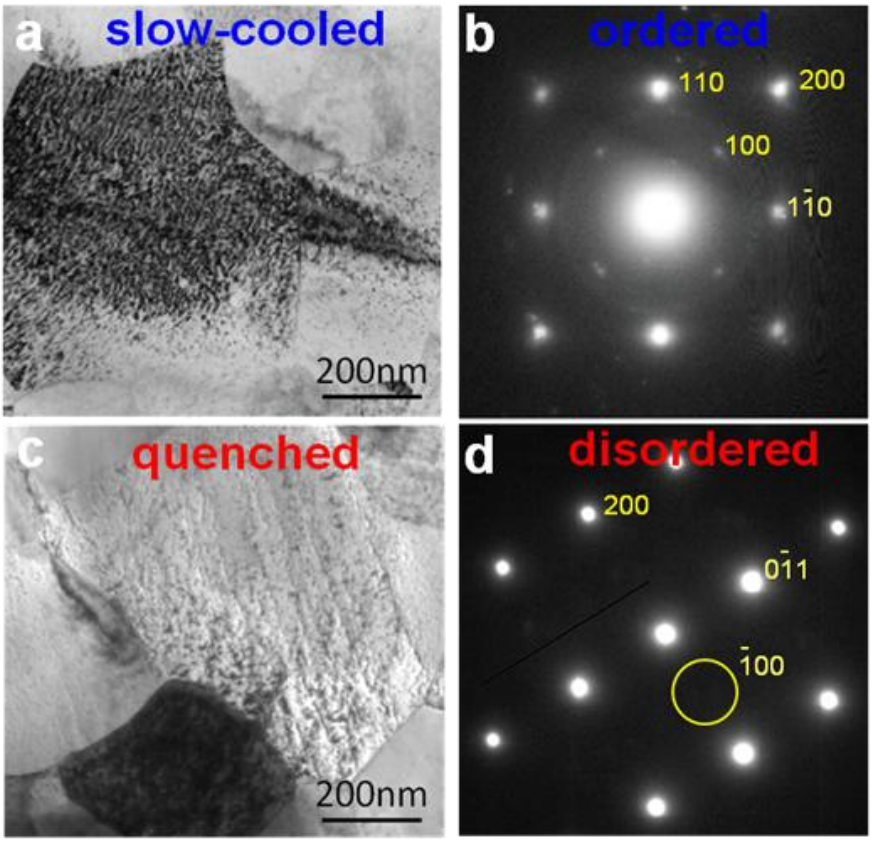

Figure 4.9 TEM of $Co_{0.66}Fe_{0.34}$ grains from the slow-cooled (a and b) and quenched (c and d) heat treatments. The bright field images (a and c) show the location of the corresponding SAED patterns (b and d). The [001] pattern from the slow-cooled grain (b) shows a typical bcc pattern with the addition of four dim [00] reflection that indicates B2 ordering. The absence of the [100] reflection in the [011] SAED pattern of the quenched grain indicate the grain is disordered.

4.4.3: Atomic Force Microscopy (AFM)

Atomic force microscopy was used to probe the topography of the Co-Fe thin films in an effort to provide some topological information about the film surfaces. Figure 4.10 shows the image of an as-deposited sample of $Co_{0.66}Fe_{0.34}$ atomic composition. It shows a very fine almost amorphous type grain structure, consistent with the TEM results presented earlier. It is obvious from the figure that this fine grain structure resulted in a smooth surface as shown. The root mean square (RMS) roughness of the as-deposited is estimated to be less than 1 nm.

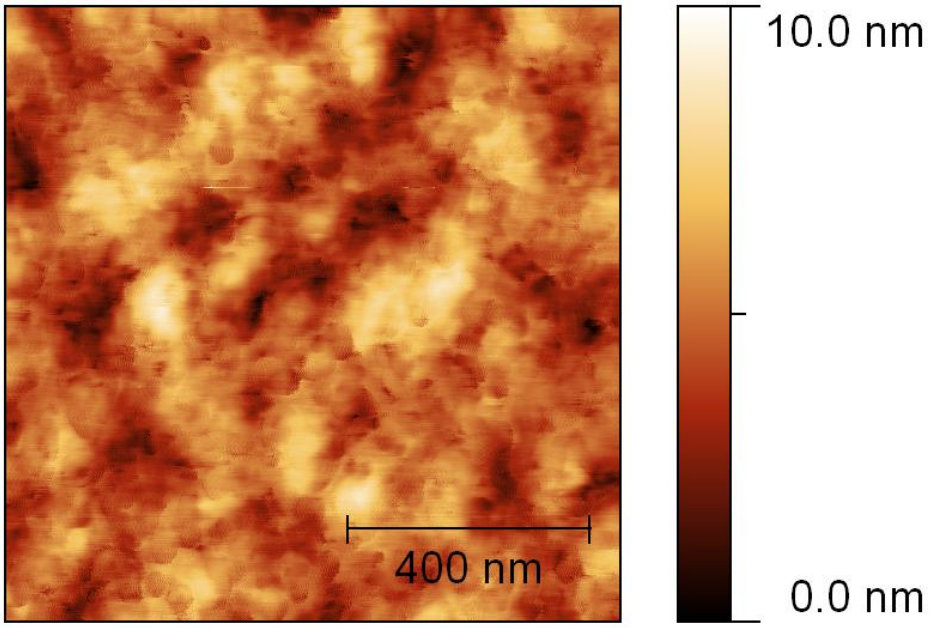

Figure 4.10 AFM of an as-deposited $Co_{0.66}Fe_{0.34}$ thin film sample. The image shows a smooth surface and a very fine grain structure almost amorphous in nature.

Similar measurements were performed on annealed (slow-cooled and water-quenched) samples. Figure 4.11 shows that annealed samples have much coarser

grains and thus a rougher surface than the as-deposited which is again consistent with the TEM analyses reported earlier. We also see that there is a substantial difference in the grain sizes between the slow-cooled and the quenched samples. This leads to almost twice the roughness of the water-quenched samples (RMS ~ 30 nm) over slow-cooled samples (RMS ~ 16 nm) of similar compositions.

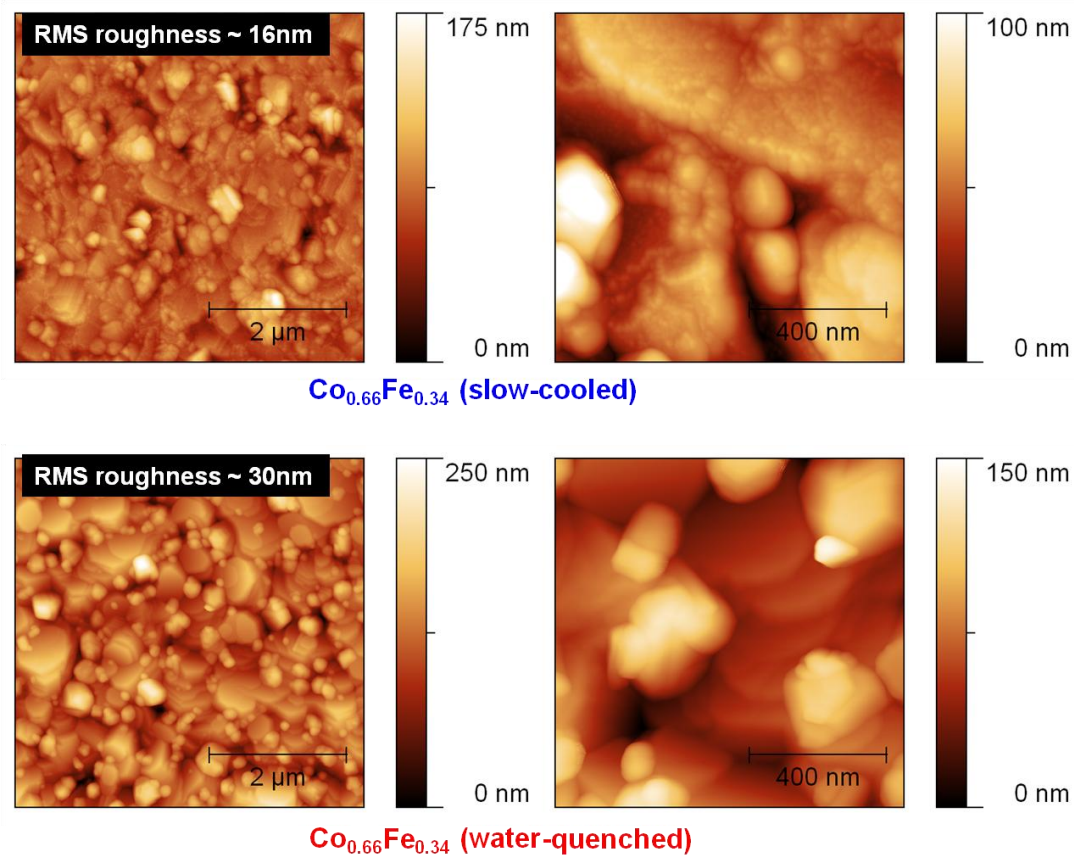

Figure 4.11 AFM of slow-cooled and quenched $Co_{0.66}Fe_{0.34}$ thin film samples. The images show a substantial difference in smoothness between the two different heat treatments. The quenched sample is almost twice as rough as the slow-cooled sample of same composition.

4.5: Magnetization studies on Co-Fe thin films

The magnetic hysteresis loops of the as-deposited and annealed and water-quenched thin film samples were measured at room-temperature using a vibrating sample magnetometer (LakeShore7410 VSM system). Figure 4.12 shows the in-plane magnetization M/M_s vs applied field curves from a $Co_{0.66}Fe_{0.34}$ as-deposited and annealed and quenched film. It is clear from the figure that this quenched film saturates well below 0.01 T. We also observe significant reduction in the coercive field as well as rounding of the M-H curves upon annealing and quenching of the film. Compared to the as-deposited film, the quenched film displays a much smaller coercive field of 50 Oe. This is consistent with the heterogeneous magnetostriction model that an applied field leads to reconfigurations of fct microdomains and the bcc magnetic domains resulting in reduction of the coercive field.

Using the "butterfly" curves presented in Chapter 2.4 of the magnetostriction plots, we were able to extract the coercivity in the as-deposited and slow-cooled spreads. This was done by taking the difference in magnetic field at peak-to-peak in at each composition. Figure 4.13 shows the coercivity mapped as a function of composition for the as-deposited and annealed and slow-cooled films. As the figure indicates, there is more than 50% reduction in the coercivity of the slow-cooled over as-deposited samples over majority of the composition. The annealed and quenched sample (not shown) shows even lower coercive field than the slow-cooled which is consistent with the results obtained via the VSM method. Due to the strong crystallinity of the quenched samples which results in smaller coercivity, it was difficult to get accurate measurements using the method employed here. Therefore,

only the as-deposited and slow-cooled samples, which have larger coercivity was measured.

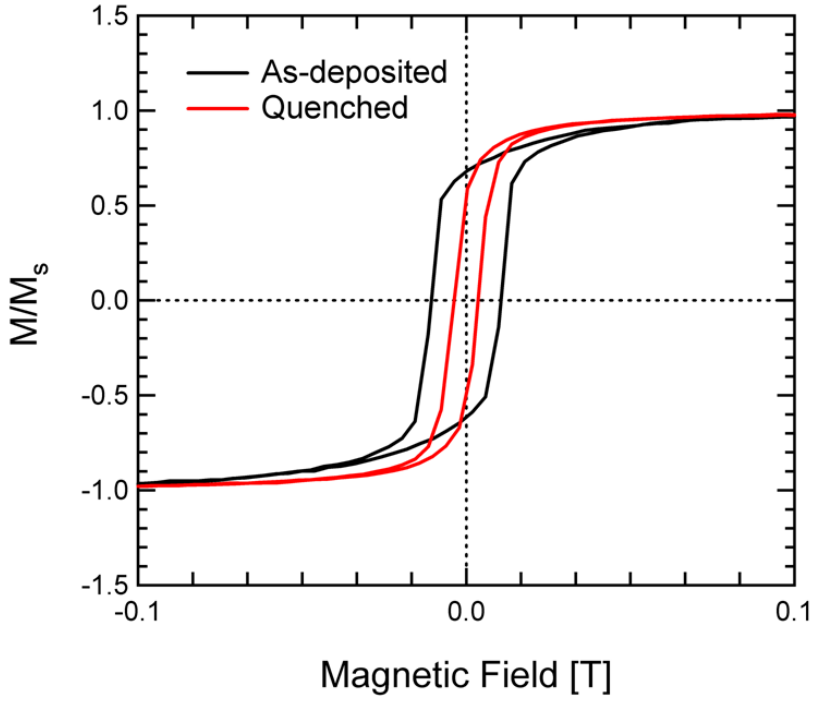

Figure 4.12 In-plane M – H curves for as deposited and quenched $Co_{0.66}Fe_{0.34}$ thin films. It also shows the reduction in coercivity in the quench film.

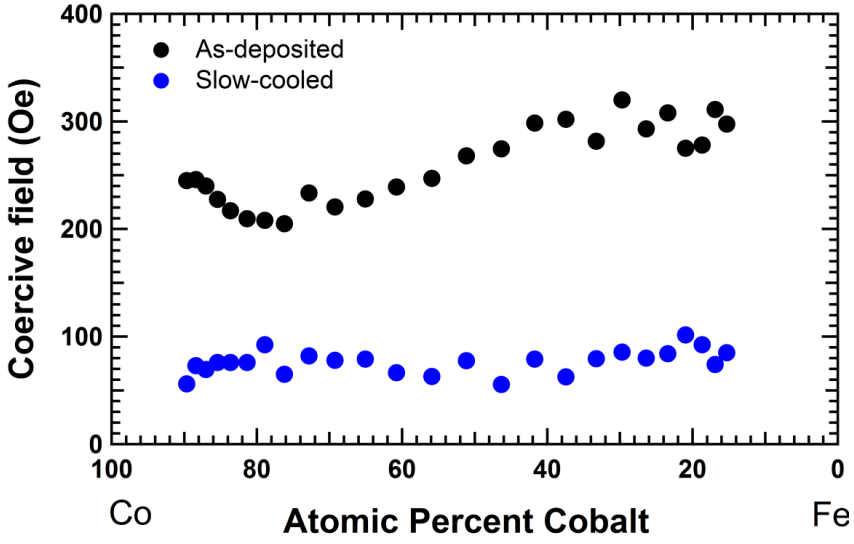

Figure 4.13 Difference in coercivity between the as-deposited and the annealed and slow-cooled composition spread samples.

4.6: Discussion

The substantial enhancement of magnetostriction in annealed $Co_{1-x}Fe_x$ thin film alloys observed here, particularly in the quenched samples, and dependence of the microstructure on processing underscores the close tie between microstructure and magnetostriction. It is remarkable that annealing the sample at a temperature/composition close to the (fcc+bcc)/bcc phase boundary followed by quenching would yield magnetostriction values more than three times that of its as-deposited state. In Figure 4.5a, we see that the peak of magnetostriction shifts to ~7 at.% Co lower composition after annealing. Similarly, the (fcc+bcc)/bcc phase boundary in Figure 4.6 shifts by about the same amount in the annealed spreads indicating that the peak of magnetostriction is linked to this structural phase interface in the composition space.

From Figure 4.6, we also see that the dominant phase at the (fcc+bcc)/bcc interface is bcc. The TEM data from Figure 4.8c and Figure 4.8d of an annealed sample also confirm that the composition consists of the predominant bcc phase and a secondary fcc phase. As discussed above, precipitation of the fcc Co-rich grains into the bcc α-Fe matrix is the cause of the increase in magnetostriction observed in the annealed samples. This is analogous to the Fe-Ga alloy system where the maximum magnetostriction is observed near the $A2/DO_3$ phase boundary at the composition of $Fe_{0.8}Ga_{0.2}$. In a recent report, a significant amount of DO_3 nanoprecipitates dispersed in the host A2 matrix was observed in Fe-Ga samples, and the DO_3 nanoprecipitates are believed to play a significant role in the enhancement of the magnetostriction[92]. The interpretation is that coarsening resistant metastable martensitic clusters form

when DO_3 precipitates equilibrate by undergoing a displacive transition, and it is these martensitic clusters which lead to magnetostriction. It is likely that the Co-rich precipitates in our Co-Fe films function in much the same way as the DO_3 precipitates in the Fe-Ga alloys.

There is a strong dependency of the magnetostriction on the cooling process in the present Co-Fe alloys. According to the Co-Fe phase diagram, the B2 phase exists in the composition region between 28 and 78 at.% Fe. When slow-cooled, samples in this composition space are expected to enter the B2 phase and become ordered as clearly illustrated in Figure 4.9, and there is a substantial difference in magnetostriction of the slow-cooled (B2-ordered) and water-quenched (disordered) samples. Similar ordering dynamics was observed in Fe-Ga where a disordered solid solution is the preferred phase for achieving large magnetostriction[62,93].

In the case of $Fe_{0.8}Ga_{0.2}$, martensitically transformed precipitates would act as tetragonal defects embedded in the matrix [66]. Their orientations can be rotated by applying an external stress or a magnetic field. The magnitude of the resulting magnetostrictive strains is dependent on the density of the precipitates in the matrix.

In our Co-Fe films, a similar scenario can be envisioned at the (fcc+bcc)/bcc matrix boundary. The displacive transition would be bcc to fct (fcc). It is possible that the bcc phase consists of coherently stabilized DO_3[94]. It is the reorientation of the tetragonal precipitates due to magnetic field that would give rise to the magnetostriction observed here. From other TEM micrographs we have obtained from the quenched $Co_{0.66}Fe_{0.34}$, we estimate the volume fraction of the fcc precipitates to be about ~ 3.4 $x10^{-3}$. Multiplying this with the un-relaxed bcc/fcc Bain strain of

0.30, which translates to magnetostriction upon reorientation, we arrive at an upper limit magnetostriction value of 1400 x 10^{-6}. Since our annealed films are [110] textured, the relationship of the effective magnetostriction to the cubic constants is given by[52]:

$$\lambda_{eff} = \frac{1}{5}\lambda_{100} + \frac{4}{5}\lambda_{111} \quad (2.4)$$

If we assume that the reorientation strain dominates, i.e. $\lambda_{111} << \lambda_{100}$,

$$\lambda_{100} \approx 5\lambda_{eff} \sim 5 * 260\ x\ 10^{-6} = 1300\ x\ 10^{-6} \quad (2.5)$$

Thus, with a simple heterogeneous mixture model, we can obtain qualitative agreement between the observed value of magnetostriction and the expected value from reorientation of the precipitates.

We also observe significant reduction in the coercive field as well as rounding of the M-H curves upon annealing and quenching of the film (Figure 4.12). Compared to the as-deposited film, the quenched film displays a much smaller coercive field of 5 mT. This is consistent with the heterogeneous magnetostriction model that an applied field leads to reconfigurations of fct microdomains and the bcc magnetic domains resulting in reduction of the coercive field. Additionally, we see a drop in Young's modulus at the onset of magnetostriction enhancement as a function of composition in the quenched sample (Figure 4.14) as predicted in the model[66]. Young's modulus was measured by the technique described in Chapter 2.4.1. These observations together provide strong evidence that the proposed precipitate

magnetostriction model for Fe-Ga maybe applicable here in the quenched Co-Fe films at the (fcc+bcc)/bcc structural boundary.

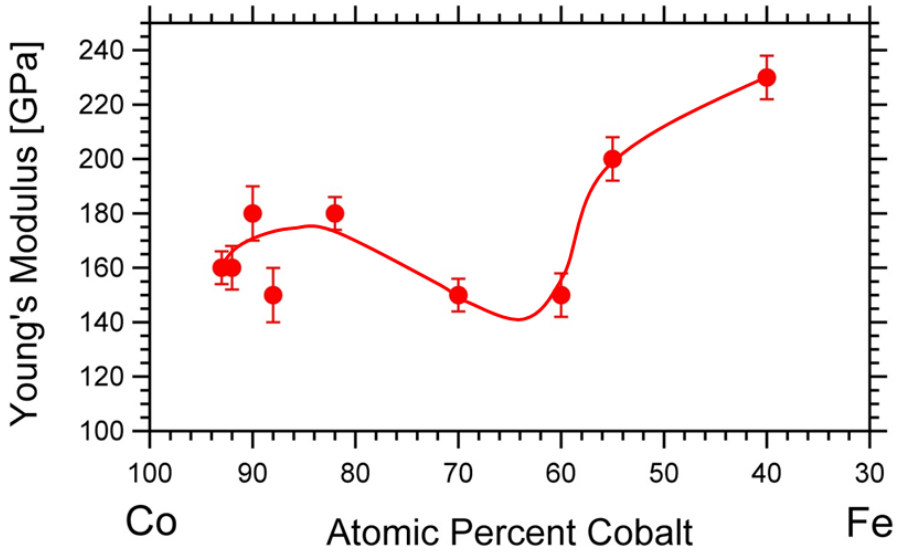

Figure 4.14 Dependence of the Young's modulus on Co composition for annealed samples. The line fit shows that there is a drop in the Young's modulus at the onset of enhanced magnetostriction.

4.7: Conclusion

Giant effective magnetostriction in excess of 260 ppm was discovered in annealed and quenched Co-Fe alloy thin film samples that were prepared using the combinatorial composition spread method. Synchrotron microdiffraction and high resolution TEM analyses suggest that an equilibrium fcc phase which formed during annealing and precipitated into a host bcc phase is responsible for the enhanced magnetostriction seen in the slow-cooled and quenched samples at the given composition. This fcc phase appears as a weak reflection in the as-deposited samples, but eventually evolves into a strong phase in the annealed samples to necessitates the

structural accommodation. The substantial difference in magnetostriction of the rapidly quenched sample and the slow-cooled sample is attributed to the ordering of B2 from a high temperature phase in the slower cooled sample, while the rapidly cooled one appears to retain its disordered state. This suggests that the formation of B2 ordering depends not only on the composition of the high temperature bcc phase but also on the rate of cooling.

The low field magnetostriction reported here is among the highest for a single thin film alloy and is promising for micro-actuator applications. A larger implication of the observed enhancement at the phase boundary and the striking qualitative agreement between the overall properties of the Co-Fe quenched films and the predictions of heterogeneous magnetostriction originally developed for Fe-Ga [66] is that the model can perhaps be extended as a guideline to explore compositions with enhanced magnetoelastic properties in other material systems. These results also suggest that perhaps if we could anneal/quench the Fe-Ga films, we can probably obtain even larger λ. However, we need to find a way to circumvent the problem caused from the high vapor pressure of Ga atoms especially at elevated temperatures, before our present technique can be employed.

Chapter 5 Magnetostriction in other binary thin films

Overview

Since the discovery of the $Fe_{0.8}Ga_{0.2}$ (Galfenol) alloy which exhibits magnetostriction more than 10 times that of bulk Fe over a decade ago, Fe-based metallic alloys have received considerable interest for magnetostrictive applications. Though the mechanisms for the large increase is still not clear, the discovery raises the possibility that perhaps other non-rare-earth alloying elements might also lead to even larger magnetostriction than Galfenol. In addition to studies done on Co-Fe alloys presented in Chapter 4, we have also explored some other systems that are of interest.

In this chapter, I will present results on magnetostrictive properties of three binary Fe-based alloys: Fe-Zn, Fe-W, and Fe-Mo that were investigated for the first time using the thin film composition spread technique. I will begin with a brief introduction, to be followed by the magnetostrictive and microstructural results that were carried out in each system, starting with the Fe-Zn binary alloy system. To conclude I will provide a comparison of all the interesting binary studies which were performed using our technique. These results are by no means exhaustive, but aim to serve as a precursor for future investigations. I should also mention that for all the samples presented in this chapter, during the magnetostriction measurements, the magnetic field was applied only in the parallel direction to the sample. Thus only the $D_{\parallel}$ component was measured. It is well-known that in many Fe-based systems, $D_{\perp}$ is negative which means that $(D_{\parallel} - D_{\perp}) > D_{\parallel}$. Since only $D_{\parallel}$ was used in the calculation of magnetostriction, the effective magnetostriction presented here is a lower bound.

As seen in Fe-Ga plot of Figure 3.2, the qualitative values of $D_{\parallel}$ is a reasonable reflection of the composition dependence magnetostriction in the spread, even though the quantitative values are different.

5.1: Introduction to Fe-Zn binary alloys

The Fe-Zn phase diagram in Figure 5.1 shows the various phases present in this system but more importantly it shows that Zinc has a large solubility in α-Fe at elevated temperatures[95]. Fe-Zn alloys are of interest in the study of magnetostriction in α-Fe base binary alloys for a number of reasons. Zn occupies a position next to Ga in the period table, thus the effect of Zn on the magnetostriction in Fe could lead to a better understanding of the mechanism(s) for large magnetostriction in certain Fe alloys compared with pure Fe. In one report, Zn has been porously substituted for Fe in the (Tb-Dy)Fe-2 Laves phase compounds to study its effect on magnetostriction which is known to decrease with increasing prestress[96]. In general, processing of Fe-Zn alloys in bulk form is very challenging. The main issue is that the boiling point of Zn (1179 K) is much lower than the melting point of Fe (1809 K)[95], and this limits processing temperatures to below 1179 K. The two metals cannot be melted together because of the high vapor pressure of Zn. To date, Fe-rich Fe-Zn alloys have been fabricated either by (i) vapor-phase transport and dissolution of Zn in Fe[97] or (ii) mechanical alloying[98], and recently by explosive compaction[75]. To the best of our knowledge, there have not been any studies of magnetostriction in Fe-Zn thin films.

Here, we applied the combinatorial thin film approach to the Fe-Zn binary alloys. Composition spread thin films of Fe-Zn where the composition continuously changes were deposited in an ultra-high vacuum sputtering chamber with two

magnetron sputtering guns oriented in a non-confocal geometry, the details of which can be found in Chapter 2.2.2. To deposit binary spreads of Fe-Zn, a pure Fe target and a pure Zn target were co-sputtered at 75 and 40 W, respectively on micro-machined cantilevers held at room temperature as described in Chapter 2.1. In consideration of the high vapor pressure known to exist in Zn, the cantilever samples were post-annealed in vacuum at 300 ^{o}C and then slow-cooled. Magnetostriction measurements are presented for as-deposited and vacuum annealed (300 ^{o}C) samples, followed by some structural data obtained by X-ray diffraction and TEM.

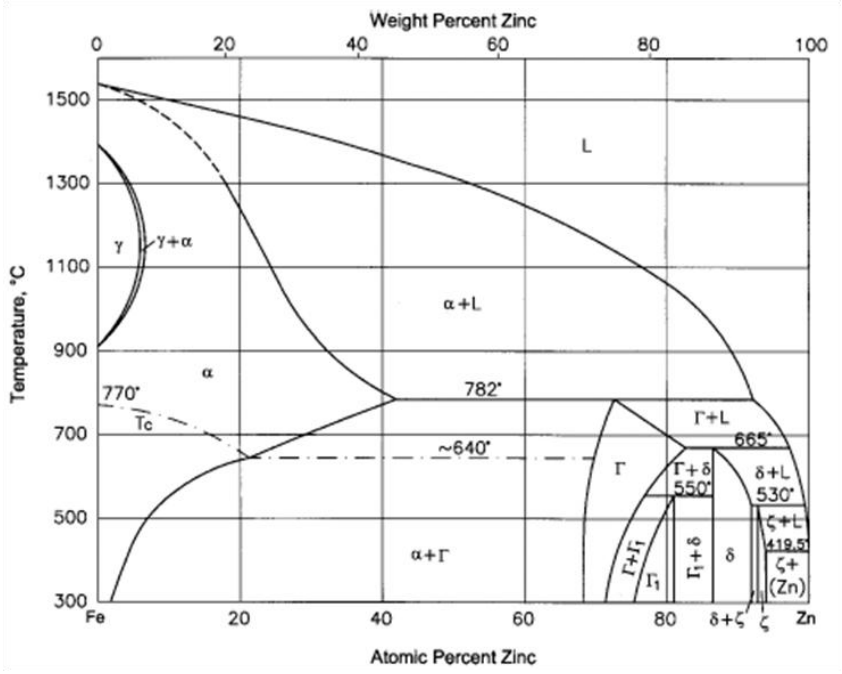

Figure 5.1 Fe-Zn phase diagram Ref[95].

5.1.2: Magnetostriction in Fe-Zn thin films

Figure 5.2 shows the magnetostriction variation as a function of atomic composition for the $Fe_{1-x}Zn_x$ composition spread film samples. Samples with up to 50

atomic percent zinc was investigated. Two peaks of magnetostriction were observed one at about ~7 at.% and the other at ~35 at.% Zn for the room temperature as-deposited samples. The annealed samples showed a modest increase in magnetostriction but the overall trend mirrors that of the as-deposited samples. The largest peak in effective magnetostriction was 40 ppm observed at ~7 at.% in the annealed sample. These results differ from the theoretical predictions of $3/2\ \lambda_{100} >$ 200 ppm near 12 at.% Zn[99]. The difference can attributed to the clamping effect imposed by the substrate and the fact that we only measured the $D_{\|}$ component, which would lead to lower bound magnetostriction values.

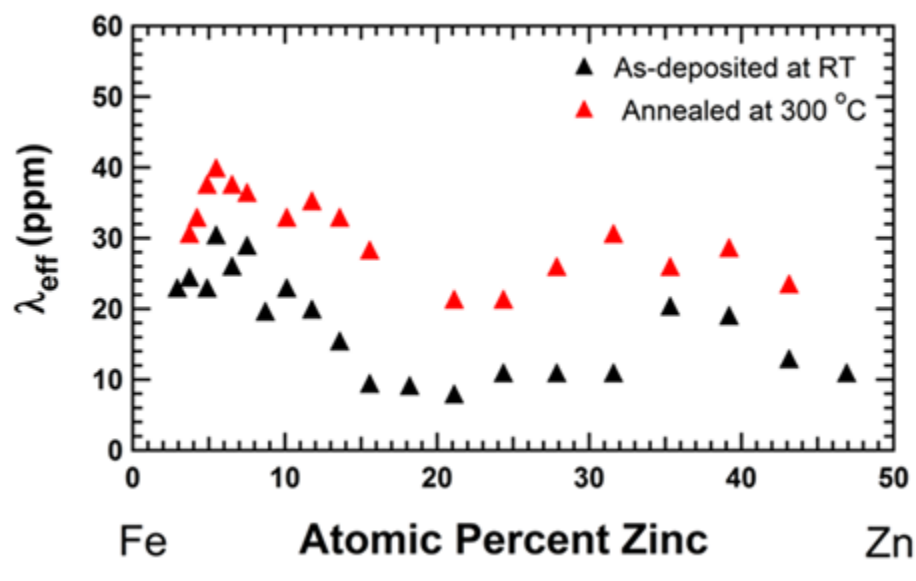

Figure 5.2 Experimental results of magnetostriction in Fe-Zn thin film alloys for as-deposited (black) and vacuum annealed (red) samples showing two small peaks at ~7 and ~30 at.% Zn.

5.1.3: X-ray diffraction in Fe-Zn thin films

To explore the structural properties, synchrotron X-ray micro-diffraction was carried out on the two Fe-Zn composition spreads to map their phase distribution. Figure 5.3 shows contour plots of the measured d-spacings as a function of atomic composition for the (top) as-deposited and (bottom) annealed and slow-cooled Fe-Zn samples. In the as-deposited spread, a dominant α-Fe (110) phase spans almost the entire Fe-Zn composition range studied here. Figure 5.3 (bottom) shows the diffraction data for the same composition spread after it was vacuum annealed at 300 ˚C and slow-cooled. The peak near 2.02 Å that was prominent in the as-deposited state remains, but the full width half max value for the reflection is half of the as-deposited value, indicating a well crystallized bcc (110) phase peak. In addition, there are few spots of high intensity ~ 2.1 Å for 10 and 25 at.% Zn compositions likely a result of Zn clustering.

To elucidate further correlations between the magnetostriction and structural origins, two compositions of $Fe_{0.95}Zn_{0.5}$ and $Fe_{0.75}Zn_{0.25}$ samples were examined in their as-deposited and annealed conditions using a D8 Bruker XRD equipment. Only one peak at ~44.5 (2-theta) degrees which appears to be that of bcc Fe (110) phase was observed in the two sets of samples as shown in Figure 5.4. From these results, we see that the position of the bcc Fe phase peak shifts to lower 2-theta values at higher Zn content. This suggests an enlargement of the crystal lattice which means that Zn atoms are substituting Fe in these alloys.

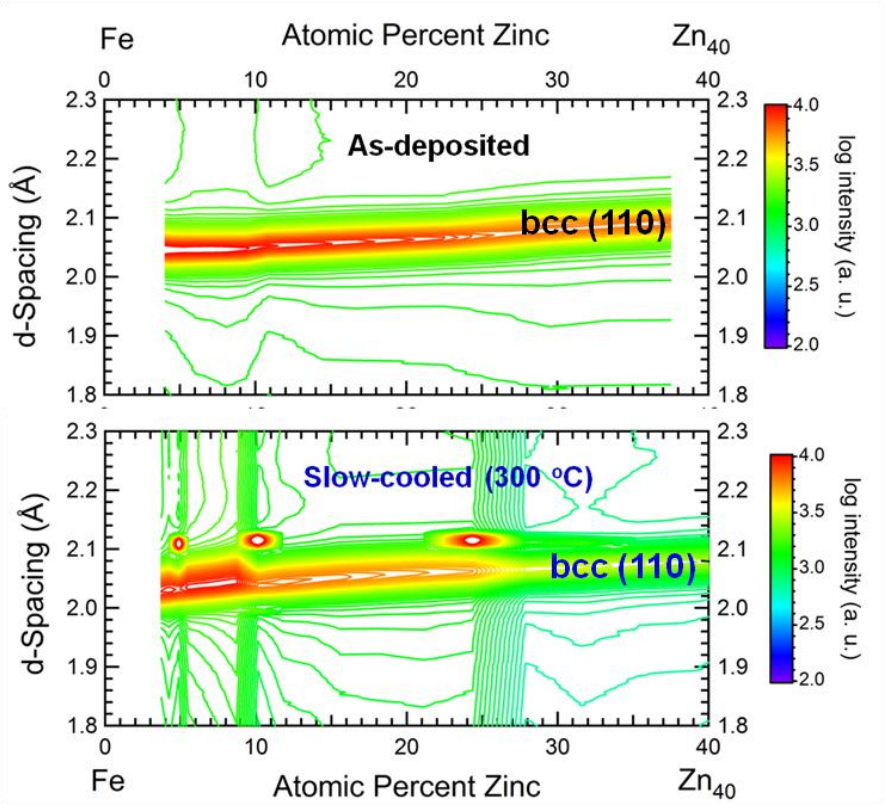

Figure 5.3 Synchrotron X-ray microdiffraction of two Fe-Zn composition spreads. Top) as-deposited, bottom) annealed at 300 °C and slow-cooled.

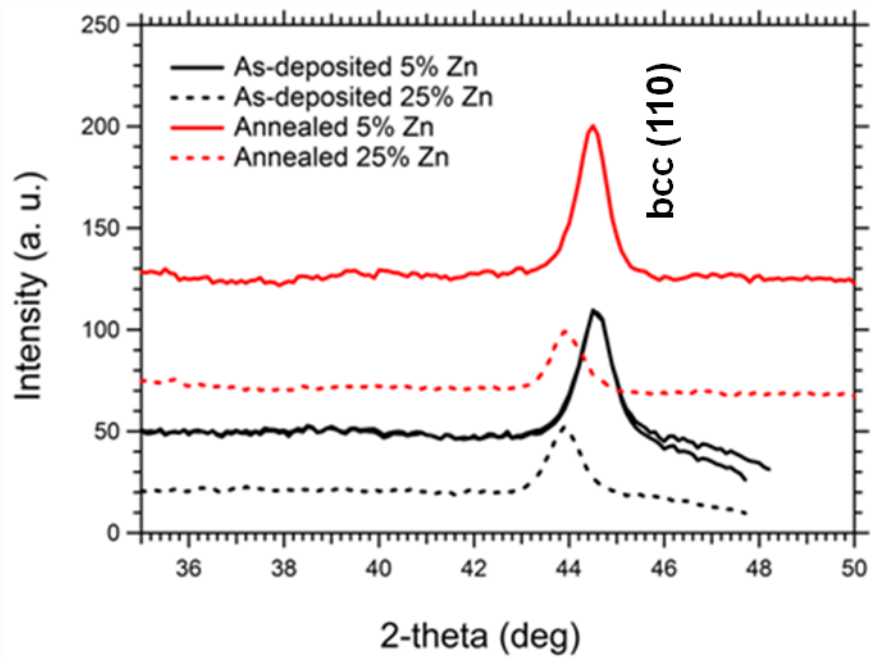

Figure 5.4 X-ray patterns of $Fe_{0.95}Zn_{0.05}$ and $Fe_{0.75}Zn_{0.25}$ thin film samples. Red plots) annealed sample, black plots) as-deposited.

5.2.4: Micro-structural studies of Fe-Zn thin films

The microstructure of the Fe-Zn thin films were examined by TEM. Due to the potential problems caused by the high vapor pressure from Zn atoms, it was necessary to ascertain if the sputtering technique used here was capable of producing good homogeneous films. Any segregation or clustering of Zn atoms would be detrimental to our efforts. The goal of this microscopy study was therefore to determine homogeneity of the Zn atoms in the bcc Fe matrix. Despite the modest magnetostriction observed in these films, there is still great benefit in realizing adequate techniques that can produce high quality films. Figure 5.5 and Fig 5.6 show the TEM image of as-deposited and annealed $Fe_{0.95}Zn_{0.5}$ and $Fe_{0.75}Zn_{0.25}$ samples.

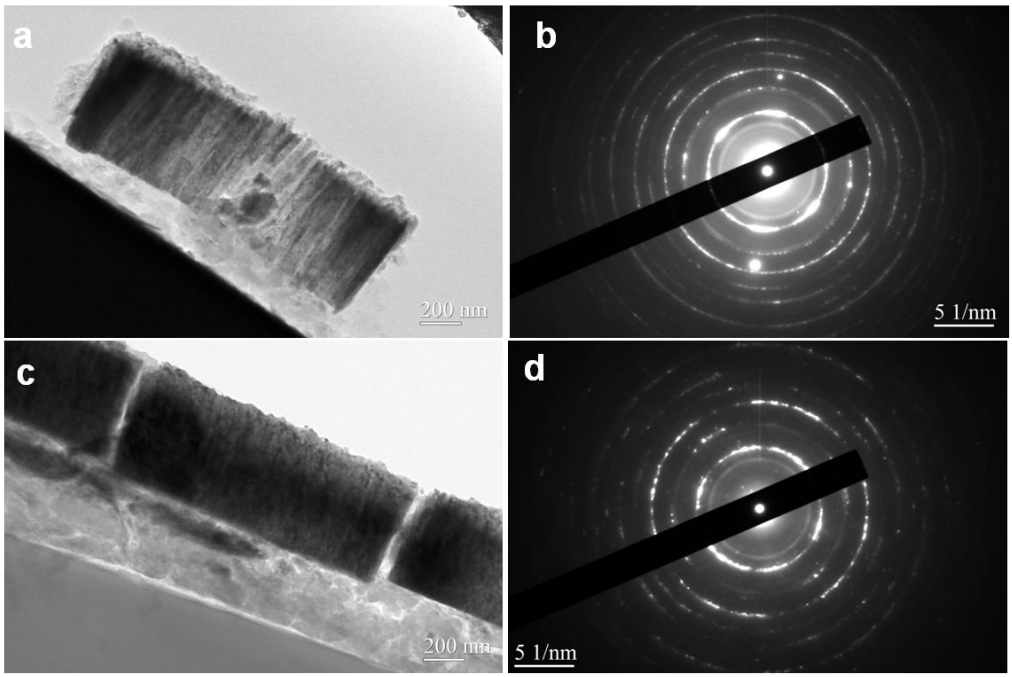

Figure 5.5 Bright-field image and SAED patterns for $Fe_{0.95}Zn_{0.5}$ thin films. a) as-deposited bright-field image, b) corresponding SAED pattern, c) bright field image for annealed sample, d) corresponding SAED pattern.

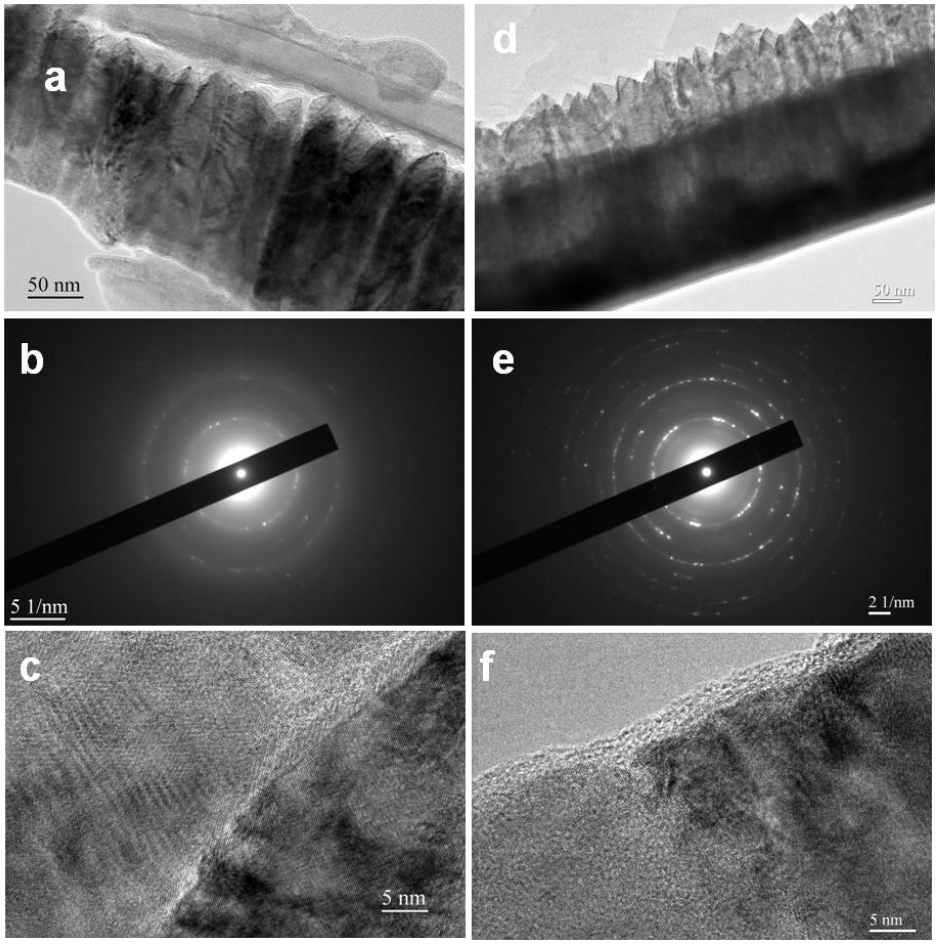

Figure 5.6 Bright-field image and SAED patterns for $Fe_{0.75}Zn_{0.25}$ thin films. a) bright-field image, b) corresponding SAED pattern, c) high-resolution image of as-deposited sample. d) bright-field image e) corresponding SAED pattern, f) high-resolution image of annealed sample.

5.2.5: Conclusion on Fe-Zn thin films

$Fe_{1-x}Zn_x$ composition spread film samples with *x* up to 50 % were fabricated using the composition spread technique. Their magnetostrictive and microstructural properties were analyzed in two sets of samples: one as-deposited and the other annealed and slow-cooled at 300 ^{o}C. Magnetostriction variation as a function of atomic composition showed two peaks one at about ~7 at.% and the other at ~35 at.%

Zn. The largest peak in effective magnetostriction was 40 ppm observed at ~7 at.% in the annealed sample. Synchrotron and conventional X-ray diffraction showed only the α-Fe phase over all compositions studied. Despite the modest values of magnetostriction observed, the TEM results of Figure 5.6 shows no segregation or clustering of Zn atoms in the Fe matrix, suggesting that the fabrication technique employed here is reliable for growing high quality homogeneous Fe-Zn films.

5.3: Fe-W and Fe-Mo binary alloys

5.3.1: Introduction to Fe-W and Fe-Mo binary alloys

As a part of our continued effort to explore other Fe-based systems which could potentially give large magnetostriction, Fe-W and Fe-Mo binary alloys were investigated. Similar to the Fe-Ga and Fe-Zn alloys discussed earlier, Fe-W and Fe-Mo has an α-phase. They are non-ideal solid solutions and have non-random distribution of solute atoms in the bcc parent lattice, which means they exhibit either solute clustering or solute ordering[100]. Strain modulations introduced due theses non-random distributions of solute atoms can influence the magnetostriction.

Guruswamy et al[100] studied the magnetostrictive behaviors of several compositions of Fe-W and Fe-Mo single crystals. The bulk materials were grown using vertical Bridgman technique, and post-growth treatment were performed. Table 3 shows a summary of the study. As is the case with most bulk synthesis techniques, only a limited number of compositions can be produced in single crystal experiments.

Table 3 Magnetostriction constant λ_{100} for various Fe alloy single crystals Ref[100].

Alloys	*Thermal history*	*Magnetostriction (3/2) λ_{100} ($x10^{-6}$)*
Fe-15 at.% Mo	Annealed at 1250 ^{o}C for 70 days	123
Fe-17.5 at.% Mo	DG	24
Fe-17.5 at.% Mo	Annealed at 1400 ^{o}C for 4 hrs	75
Fe-4.4 at.% W	Annealed at 1400 ^{o}C for 4 hrs	97
Fe-10 at.% W	DG	99
Fe-10 at.% W	Annealed at 1500 ^{o}C for 2 hrs	122

Due its high-throughput and versatility, the combinatorial strategy was applied to the Fe-W and Fe-Mo binary alloys. As shown in previous studies[28,39-40], this technique is good at uncovering potentially interesting compositions which may have been overlooked during bulk synthesis. Binary composition spread thin films of Fe-W and Fe-Mo were fabricated in a manner similar to that described in Chapter 2.2.2. In each experiment, pure Fe, W, and Mo targets were sputtered at 75, 35, and 50 Watts, to make their respective binary spreads.

5.3.2: Magnetostriction in Fe-W and Fe-Mo thin films

Figure 5.7 shows the magnetostriction variation as a function of atomic composition for the $Fe_{1-x}W_x$ composition spread film samples. The figure shows that as more W is substituted for Fe, there is a monotonous increase in magnetostriction from pure Fe up to about 10 at.% W with a maximum effective magnetostriction ~ 45 ppm. As more W is added, the magnetostriction decreases dips below that of pure Fe at around 25 at.% W.

Figure 5.8 shows the magnetostriction variation as a function of atomic composition for the $Fe_{1-x}Mo_x$ composition spread film samples. In this plot, there appears to be no clear dependence of the magnetostriction on composition as the values of the magnetostriction hovers around that of pure Fe (~ 25 ppm) up 25 at.% Mo. From this plot, it appears that there might be a potentially interesting composition at approximately 7 at.% Mo, which is the composition of largest magnetostriction (~ 35 ppm) in this plot. Qualitatively the results reported here for the Fe-W are consistent with previous bulk reports[100] where a peak in magnetostriction was observed at 10 at.% W in bulk crystals. As discussed in the introduction of this chapter, the effective magnetostriction values presented here on Fe-W and Fe-Mo thin film spreads are lower bound, since only values of $D_{\parallel}$ was used calculation the magnetostriction.

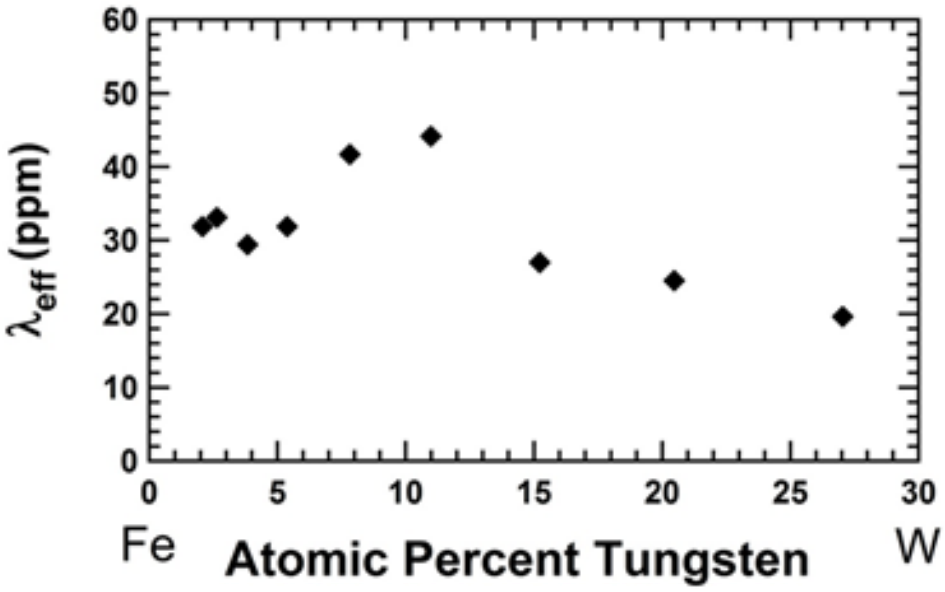

Figure 5.7 Effective magnetostriction in Fe-W thin film alloys. The figure shows maximum magnetostriction ~ 10 at.% W.

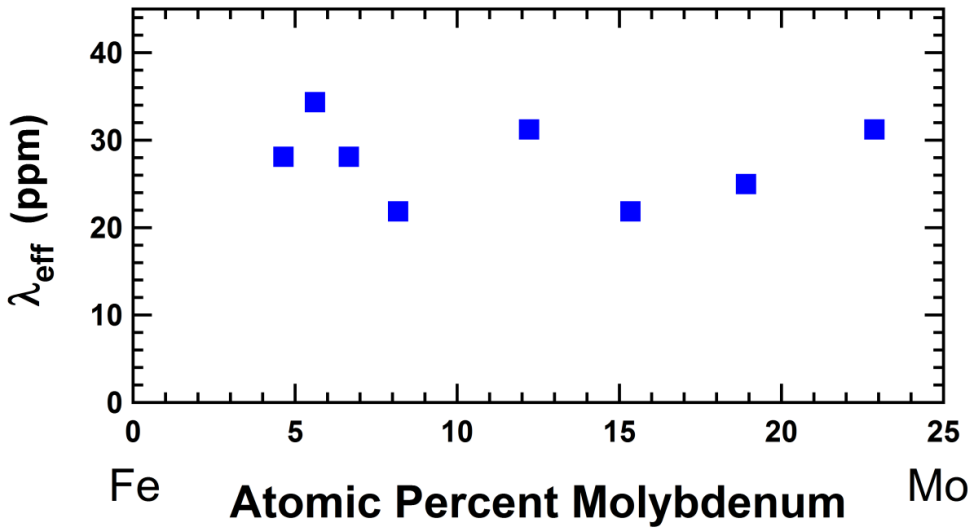

Figure 5.8 Effective magnetostriction in Fe-Mo thin film alloys. The figure shows maximum magnetostriction ~ 7 at.% Mo.

5.3.3: Conclusion on Fe-W and Fe-Mo thin films

Fe-W and Fe-Mo composition spread film samples were fabricated using the composition spread technique. Magnetostrictive characterizations were performed on both sets of spreads. The largest peak in effective magnetostriction was 45 ppm observed at ~10 at.% W in the Fe-W spread while the Fe-Mo spreads did not show any clear dependence of magnetostriction on composition in samples studied.

5.4: Comparison of different Fe-based binary alloy system

We compare the magnetostrictive values of the three α-Fe binary systems which were studied in this thesis. Figure 5.9 shows the comparison of those magnetostriction values for the different binary thin film composition spreads. As seen in the figure, the Fe-Ga spreads show much larger magnetostriction values than

the other samples. The Fe-W and Fe-Zn alloys only show modest magnetostriction values.

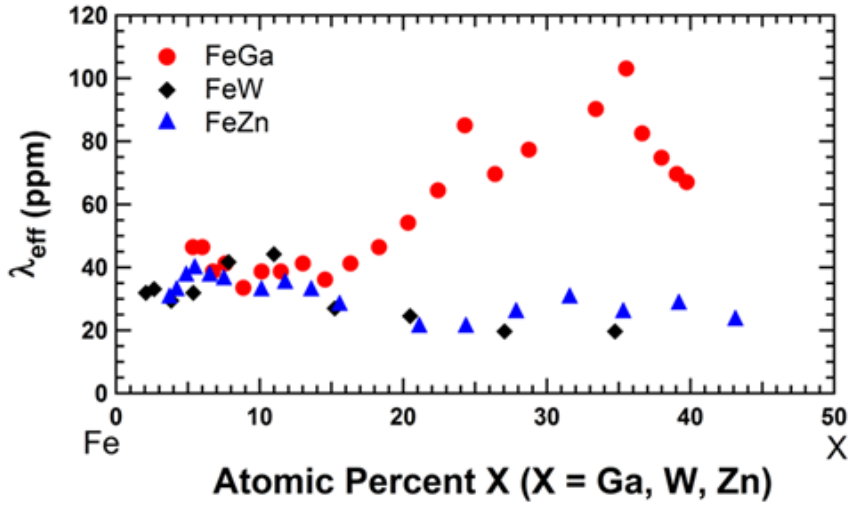

Figure 5.9 Comparison of magnetostriction in different Fe-based metallic thin film alloys.

Chapter 6: Magnetostriction in some ternary alloys

As stated previously in Chapter 3, the discovery of Galfenol has triggered explorations of alloys to integrate in the Fe-Ga system in attempts to increase the magnetostriction. This Chapter is a compilation of some of the promising ternary systems which we have investigated using the co-sputter deposition technique. All the results presented in this chapter were done on as-deposited samples with no post-annealing. Also, no $D_{\perp}$ measurements were done, which means that the magnetostriction values are only lower bound.

6.1: Introduction to Fe-Ga-Zn ternary system

The embrittlement caused by large amounts of Ga has led to the study and development of partially replacing Ga with a suitable ternary element. The goal of the ternary element is to enhance the workability of the material especially in areas of ductility while preserving its large magnetostriction. So far majority of the alloying studies have been done with bulk materials where limited compositional sampling and run-to-run errors can cause promising compositions to be potentially overlooked.

6.1.1: Fabrication of Fe-Ga-Zn thin-films

Using theoretical predictions based on density functional theory calculations, Wu et al[99] that postulated that there should be substantial magnetostriction at the compositions of $Fe_{0.875}Ga_{0.062}$ $Zn_{0.062}$ in the Fe-Ga-Zn system (Figure 6.1), we applied the combinatorial approach to investigate Fe-Ga-Zn ternary system. The deposition technique is the same as described in the deposition of Fe-Ga binary but now we co-sputtered with a third element, Zn. We co-sputtered pure Fe, pure Zn, and

intermetallic Fe_2Ga_3 targets to create ternary composition spreads. The film thickness was about 0.7 μm.

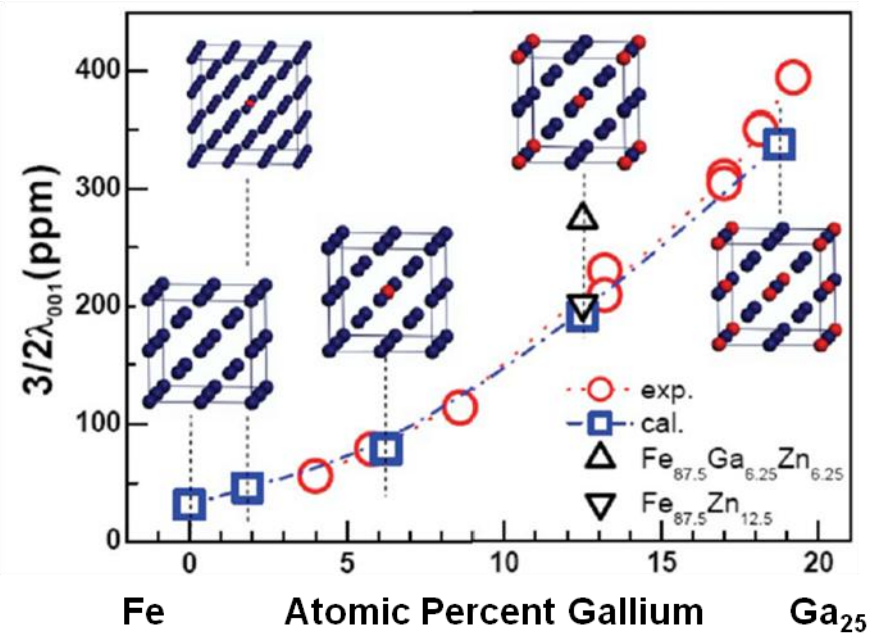

Figure 6.1 Theoretical calculations of magnetostriction in $Fe_{0.875}Ga_{0.062}$ $Zn_{0.062}$ bulk material. These calculations were generated using rigid band models based on density functional theory Ref[99].

6.1.2: Magnetostriction in Fe-Ga-Zn thin-films

Figure 6.2 shows the magnetostriction results of the ternary Fe-Ga-Zn thin-films. Note that the maximum compositions for Zn and Ga is 50 at.%. The first notable feature about this figure is that as one goes along the Fe-Zn binary compositions, we see modest values of magnetostriction with maximum less than 40 ppm, which is consistent with the results obtained for the binary Fe-Zn. On the other hand, the highest magnetostriction lies along the Fe-Ga_{50} binary and the maximum effective magnetostriction occurs for compositions close to 35 at.% Ga with < 2 % of Zn addition. There is a slight increase in the magnetostriction value of the ternary Fe-

Ga-Zn over binary Fe-Ga. Another important take away from this figure is the unexpectedly large values of magnetostriction around $Fe_{0.6}Ga_{0.1}Zn_{0.3}$ composition, where the maximum magnetostriction approaches ~80 ppm.

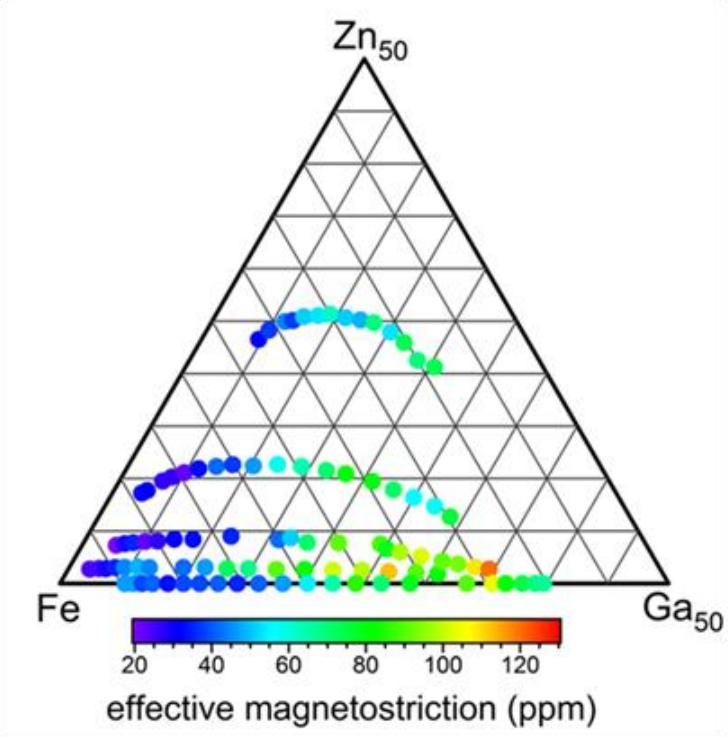

Figure 6.2 Effective magnetostriction in Fe-Ga-Zn thin film alloys.

6.2: Introduction to the Fe-Co-Al ternary alloys

Another ternary system we studied was the Fe-Co-Al. Fe-Al is a well-known magnetostrictive system and have magnetostriction upwards of 150 ppm in bulk materials[59]. From our own studies we have discovered that the Fe-Co is large magnetostrictive material. Individually, Fe-Al and Fe-Co have large magnetostriction, so the idea behind this ternary exploration was to see if we could obtain enhanced magnetostrictive properties in some other compositions by combining these two

systems. At the time when this study was carried out there has not been any other thin film or bulk study on this system.

6.2.1: Magnetostriction in Fe-Co-Al thin-films

Again we apply the combinatorial strategy to the Fe-Co-Al ternary system through the simultaneous sputtering of Fe, Co, and Al targets on cantilevers, as described throughout this thesis. The result of the magnetostriction measurements on the as-deposited Fe-Co-Al ternary thin films is shown in Figure 6.3. The highest magnetostriction λ_{eff} ~ 80 ppm, obtained in this system is for the $Fe_{50}Co_{25}Al_{25}$ composition. We also observed some consistency along the Fe-Co binary, with small amounts of Al, with our own studies on the Co-Fe results in Chapter 4. Here at the approximate $Fe_{35}Co_{65}$ composition (> 5 at.% Al), we get an effective magnetostriction of ~70 ppm which is around the same value we reported for the as-deposited binary film in Figure 4.3.

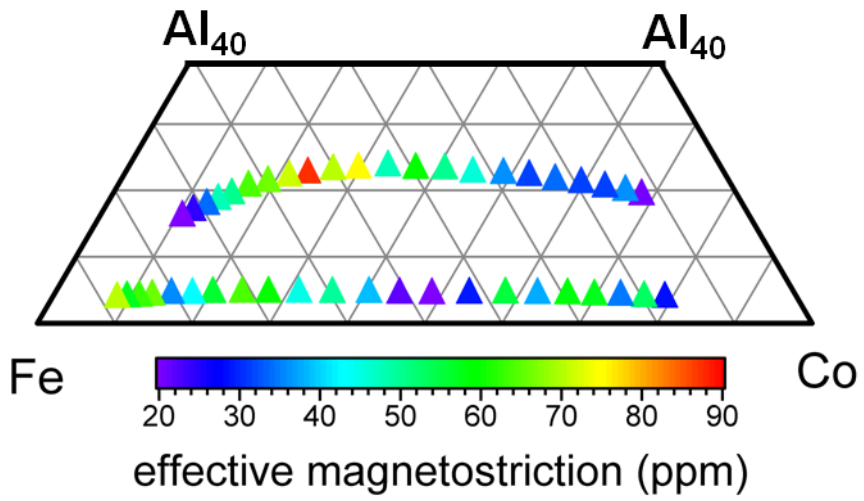

Figure 6.3 Effective magnetostriction in as-deposited Fe-Co-Al thin films.

6.3: Conclusion on Fe-Ga-Zn and Fe-Co-Al thin films

The composition spread technique was applied in the investigation of magnetostriction in Fe-Ga-Zn and Fe-Co-Al thin films. Though our magnetostriction results on the Fe-Ga-Zn thin films didn't corroborate with the values from theoretical predictions, we found that near the magnetostriction values around the $Fe_{0.6}Ga_{0.1}Zn_{0.3}$ compositions was reasonably high, λ_{eff} ~ 80 ppm. This is interesting from an applications and cost points of view, because this means that a cheaper metal like Zn could substitute Ga, while still preserving the magnetostriction.

For the Fe-Co-Al ternary, the highest effective magnetostriction, λ_{eff} ~ 80 ppm, was observed near the $Fe_{50}Co_{25}Al_{25}$ composition. We also found good agreement along the Fe-Co binary, with minute amount of Al added, to our previous results on as-deposited binary Co-Fe thin films reported in Chapter 4.

Chapter 7

7.1: Overall conclusion

Magnetostrictive materials belong to a class of smart materials that show dimensional change in response to a magnetic field. They are used in a variety of applications such as sonars, ultrasonic shakers, position controllers for machine tool heads, and in acoustic devices and magnetic field sensors. They have also been used in conjunction with piezoelectric materials in hybrid transducers. As thin films they are used for monitoring biomechanical movement[101], and in microactuators[102], micro bio sensors[103], and several other MEMS applications[104].

In this thesis, we investigated the composition dependent magnetostrictive and micro-structural properties of several binary (Fe-Ga, Co-Fe, Fe-Zn, Fe-W, Fe-Mo) and ternary (Fe-Ga-Zn, Fe-Co-Al) Fe-based thin film alloys prepared using a co-sputtering based composition spread approach. This technique facilitates synthesis and screening of large compositional landscapes in individual studies and allows rapid identification of compositions with enhanced physical properties. Magnetostriction measurements were performed on arrays of micro-machined cantilevers with sputter deposited compositionally graded films.

From the study on the binary films, the Co-Fe alloys emerged as a large magnetostrictive material with magnetostrictive values that rival that of well-known large magnetostrictive compound such as Fe-Ga. In the Co-Fe alloy, a substantial increase in magnetostriction was observed for compositions near the (fcc+bcc)/bcc phase boundary, in particular after annealing the spread at 800 ^{o}C for 1 hr, this enhancement was found to depend on the cooling rate from the annealing

temperature. Structural characterization by synchrotron micro-diffraction and transmission electron microscopy (TEM) reveal that the large increase in magnetostriction is associated with the presence of an equilibrium Co-rich fcc phase that precipitates into a host Fe-rich bcc phase upon annealing. The Co-Fe system is compared with Fe-Ga alloys, in which DO_3 nanoprecipitates dispersed in the host A2 matrix was observed. The DO_3 nanoprecipitates in the Fe-Ga alloys are believed to act as tetragonal defects in the matrix and their orientations can be changed by the application of a magnetic field, which lead to magnetostriction. It is speculated that the Co-rich precipitates in our Co-Fe films function in much the same way as the DO_3 precipitates in the Fe-Ga alloys, which would imply that the mechanisms which give rise to magnetostriction in both systems are similar. We also note that there has been a recent neutron scattering study on Fe-Ga alloys whose result is not consistent with the heterogeneous model discussed above for enhanced magnetostriction observed in Fe-Ga alloys. For more details on this, please check Chaitanya Mudivarthi PhD Thesis, University of Maryland (2010). In spite of this, we feel that the heterogeneous model presented by Khatchaturyan and Viehland provides a clear comparison between our Co-Fe films and Fe-Ga alloys. It is expected that future work will shed light on more details and the true nature of the enhanced magnetostriction observed in both systems.

The results on the as-deposited Fe-Ga-Zn and Fe-Co-Al ternary thin film spreads are somewhat encouraging. In the Fe-Ga-Zn alloys, we found that the magnetostriction value around the $Fe_{0.6}Ga_{0.1}Zn_{0.3}$ compositions was reasonably high, $\lambda_{eff} \sim 80$ ppm. This could be interesting from an application and cost points of view,

because this means that a cheaper metal like Zn could substitute Ga, while still preserving the magnetostriction. For the Fe-Co-Al ternary, the highest effective magnetostriction, $\lambda_{eff} \sim 80$ ppm, was observed near the $Fe_{50}Co_{25}Al_{25}$ composition. We also found good agreement along the Fe-Co binary with our previous results on binary Co-Fe thin films.

All the magnetostriction measurements with the exception of the Co-Fe films were carried out on room-temperature as-deposited films. Also, the Young's modulus was only measured for the Co-Fe films. In all the other films, we used an effective modulus, where $E_f/(1 + V_f) = 50$ GPa. This value was used in previous works on cantilever thin films[14].

As seen in the Co-Fe alloys, substantial a substantial increase in magnetostriction was observed after post deposition heat treatments were carried out. It is possible that performing heat treatments on some of the other binary and ternary spreads studied here, can result in similar enhancement in their magnetostrictions. As noted earlier, special considerations will have to be made when dealing with systems that have high vapor pressure elements such as Ga and Zn.

7.2: Implications of the current work

In most current applications using magnetostrictive materials, the active material is Terfenol-D, which is an expensive rare-earth containing compound. One motivation behind the development of Fe-based magnetostrictive materials, in particular Fe-Ga, is to find suitable rare-earth free materials. Our discovery of large magnetostriction at low saturation fields in Co-Fe alloys is an important step towards

achieving this goal. Figure 7.1 shows how our current finding stacks up against other magnetostrictive thin films.

Furthermore, Fe-Co has advantages of being more ductile and cheaper than the Fe-Ga, and therefore could be a strong candidate for replacing Terfenol-D or expensive rare-earths in current applications.

According to the metalprices.com website, the costs for various metals are as follows:

Terbium: < $5000 per 100 gram

Gallium: ~ $45 per 100 gram

Cobalt: ~ $4 per 100 gram

This indicates that from a cost effective point of view, replacing gallium with cobalt in Fe-based systems not only provides better ductility but it is also much less expensive.

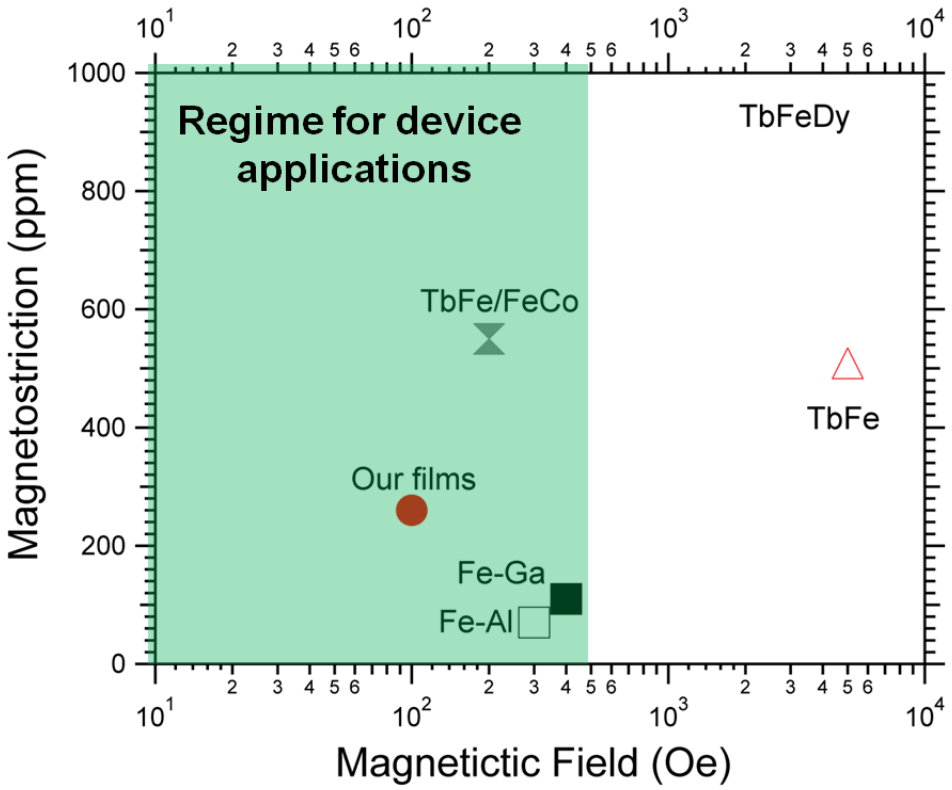

Figure 7.1 Magnetostriction vs saturation magnetic field for various magnetostrictive thin films. Our Co-Fe labeled "our films" ($Co_{0.65}Fe_{0.35}$) is within the operation regime of devices and is thus a good candidate for device applications.

7.3: Future work

Throughout this thesis, we have demonstrated that the combinatorial approach is a viable technique for investigating magnetostriction in Fe-based alloys. Table 4 highlights some of the elements from which different combinations of composition spreads were made and studied in this thesis, namely: Fe-Ga, Fe-Co, Fe-Zn, Fe-Mo,

Fe-W, Fe-Ga-Zn, and Fe-Co-Al. Though most of the work is complete on the Fe-Co, Fe-Ga, and Fe-Zn binaries, more measurements should be perform on the Fe-Mo and Fe-W alloys. For example, they should be annealed at high temperatures and their respective magnetostrictions and Young's modulus measured. The magnetostriction results presented in Chapter 5 was calculated using only $D_{\parallel}$, these measurements should be repeated for $D_{\perp}$, to obtain more precise values on the effective magnetostriction. Our preliminary results on room temperature as-deposited Fe-Co-Al is encouraging. It might be possible to get enhancement in magnetostriction after some post-deposition heat treatment is carried out, similar to the binary Co-Fe. It is recommended that the same annealing conditions (800 ^{o}C for 1hr in UHV) as that of the Co-Fe alloys be used as a starting point for the Fe-Co-Al films.

Table 4 A portion of the periodic table highlighting the elements that were to make the binary and ternary composition spreads studied in this thesis.

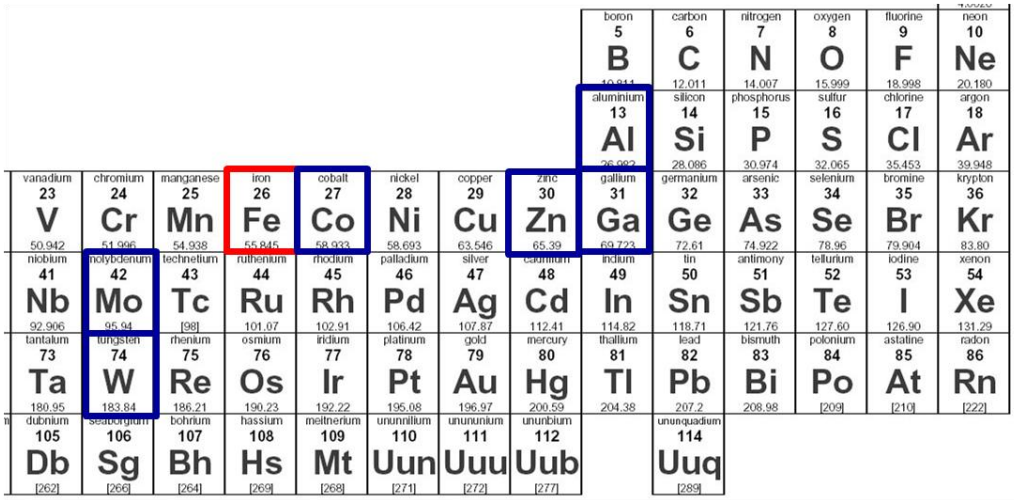

Other systems of interest

Besides the ones discussed above, there are also other ternary systems that we feel could be interesting to apply the combinatorial strategy and study their magnetostrictive properties. These have either been postulated by theory or formulated through combinations of binary systems.

Fe-Co-Ga: This ternary system might be interesting for the fact that both the binary Fe-Co and Fe-Ga alloys show appreciable large magnetostriction. Thus combining both systems could lead to an enhancement in magnetostriction. To date, there have been a few bulk studies, but to the best of our knowledge there have not been any reported thin film studies on this alloy system.

Fe-Co-W and Fe-Co-Mo: Due to the extraordinary results (260 ppm) which we obtained in annealed Co-Fe alloys, and the small magnetostriction observed in as-deposited Fe-W (~45 ppm) and Fe-Mo (~35 ppm) alloys, it is conceivable that under the right processing conditions both alloys could give large magnetostriction. It is recommended that the Fe-Co-W and Fe-Co-Mo alloys be heated treated under similar conditions to that used in Co-Fe alloys which presented in Chapter 4. In both the as-deposited Fe-W and Fe-Mo binaries, the maximum magnetostriction was observed at around 10 at.% W and Mo, respectively. Therefore, the concentrations of W and Mo should be kept under 10 at.%.

Fe-Ga-Pt, Fe-Pt-Al, Fe-Ir-Al: Theoretical work using ab initio calculations by Wu et al (MURI Review meeting, 2009) suggests that giant magnetostriction in excess of

1000 ppm could be obtained in these alloys. Below are the predicted magnetostriction values at their respective compositions:

$Fe_{88}Pt_6Ga_6$ ~ 950 ppm, $Fe_{88}Pt_6Al_6$ ~ 1156 ppm, and $Fe_{75}Irt_6Al_{18.5}$ ~ -1100 ppm. It's important to note that these theoretical predictions by Wu et al, does not take into account the heterogeneous model.

Appendix A

Re: Measuring magnetostriction in cantilever thin films

In Chapter 2.4, we talked about how to measure magnetostriction in cantilever thin films. A picture of the magnetostriction setup is shown in Figure A1.

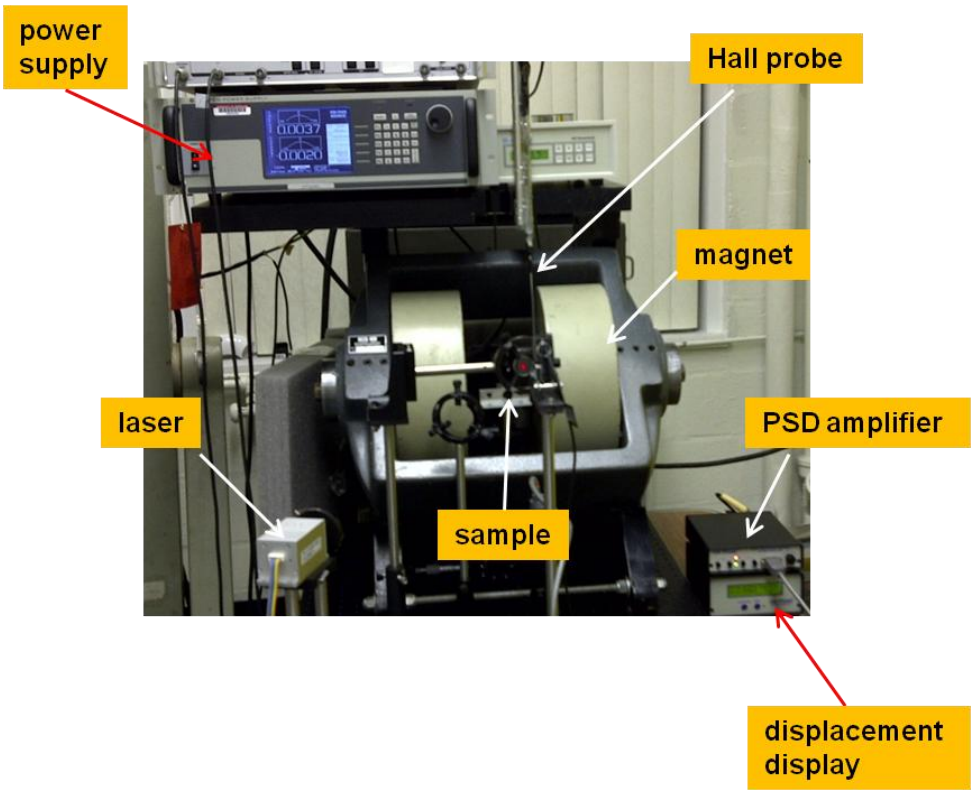

Figure A1 Picture of the high-throughput setup for measuring magnetostriction in cantilever thin films.

Now, I would like to provide some specific details when using our current setup here at UMD.

- Do not use a light chopper or a lock-in amplifier. The current PSD model (OT-301) by ON-TRAK has all adjustable parameters built in already. Using additional accessories will lead to erroneous results.
- PSD amplifier should not exceed 1 to 5 V for sum voltage and both H/L indicators should be off during measurements.
- The PSD is equipped with an optical filter. The filter is only sensitive to "red light" or the wavelength of the laser and is therefore used to filter out ambient light during measurements. However, to ensure maximum accuracy, measurements should be carried out in a dark room.
- The blue wave laser is 635 nm at 25 mW intensity. However, we have attached a 5% filter, which means the effective laser intensity is about 1.25 mW, which is appropriate for this PSD that we currently use. Note: using higher intensity laser > 5mW, while over saturate the photo-diode in the PSD which will reduce its sensitivity. This can be a big problem when measuring small displacements.

Bibliography

1. Jiles, D. Introduction to Magnetism and Magnetic Materials. 1st edn, (Chapman & Hall, 1991).
2. Joule, J. P. On a new class of magnetic forces. Ann. Electr. Magn. Chem. 8, 219-224, (1842).
3. Villari, E. Change of magnetization by tension and electric current. Ann. Phys. Chem. 126, 87-122, (1865).
4. Wiedemann, G. Uber die torsion und die beiziehung derselben zum magnetismus. Pogg. Ann. 106, 161-201, (1860).
5. Barrett, W. F. On the alterations in the dimensions of the magnetic metals by the act of magnetisation. Nature 26, 585-586, (1882).
6. Datta, S. Quasi-static characterization and modeling of the bending behavior of single crystal galfenol for magnetostrictive sensors and actuators PhD thesis, University of Maryland, (2009).
7. Clark, A. E. Ferromagnetic Materials. Vol. 1 (1980).
8. Szymczak, H. From almost zero magnetostriction to giant magnetostrictive effects: recent results. Journal of Magnetism and Magnetic Materials 200, 425-438, (1999).
9. Cooke, M. D., Gibbs, M. R. J. & Pettifer, R. F. Sputter deposition of compositional gradient magnetostrictive FeCo based thin films. Journal of Magnetism and Magnetic Materials 237, 175-180, (2001).
10. Giang, D. T. H., Duc, N. H., Richomme, F. & Schulze, S. Microstructure and magnetic studies of magnetostrictive Terfecohan/YFeCo multilayers. Journal of Magnetism and Magnetic Materials 262, 361-367, (2003).
11. Speliotis, A. & Niarchos, D. Magnetostrictive properties of amorphous and crystalline TbDyFe thin films. Sensors and Actuators a-Physical 106, 298-301, (2003).
12. Kiyomiya, T. et al. Magnetostrictive Properties of Tb-Fe and Tb-Fe-Co Films. Electr. Commun. Jpn. 91, 49-55, (2008).

13. Na, S. M., Suh, S. J. & Lim, S. H. Fabrication condition effects on the magnetic and magnetostrictive properties of sputtered Tb-Fe thin films. Journal of Applied Physics 93, 8507-8509, (2003).
14. Quandt, E. Giant magnetostrictive thin film materials and applications. Journal of Alloys and Compounds 258, 126-132, (1997).
15. Quandt, E., Ludwig, A., Betz, J., Mackay, K. & Givord, D. Giant magnetostrictive spring magnet type multilayers. Journal of Applied Physics 81, 5420-5422, (1997).
16. Quandt, E., Gerlach, B. & Seemann, K. Preparation and applications of magnetostrictive thin-films. Journal of Applied Physics 76, 7000-7002, (1994).
17. T. Tanaka, S. S., M. Okada, M. Homma, and K. Arai. in International Symposium on Giant Magnetostrictive Materials and Their Applications.
18. Honda, T., Arai, K. I. & Yamaguchi, M. Fabrication of magnetostrictive actuators using rare-earth (Tb,Sm)-Fe thin films (invited). Journal of Applied Physics 76, 6994-6999, (1994).
19. Quandt, E. & Ludwig, A. Giant magnetostrictive multilayers (invited). Journal of Applied Physics 85, 6232-6237, (1999).
20. Ludwig, A. & Quandt, E. Giant magnetostrictive thin films for applications in microelectromechanical systems (invited). Journal of Applied Physics 87, 4691-4695, (2000).
21. Quandt, E. & Ludwig, A. Magnetostrictive actuation in microsystems. Sensors and Actuators a-Physical 81, 275-280, (2000).
22. Zhao, P. et al. Fabrication and characterization of all-thin-film magnetoelectric sensors. Applied Physics Letters 94, (2009).
23. Hoogenboom, R., Meier, M. A. R. & Schubert, U. S. Combinatorial methods, automated synthesis and high-throughput screening in polymer research: Past and present. Macromol. Rapid Commun. 24, 16-32, (2003).
24. Hanak, J. J. The “multiple-sample concept” in materials research: Synthesis, compositional analysis and testing of entire multicomponent systems. Journal of Materials Science 5, 964-971, (1970).

25. Xiang, X. D. et al. A combinatorial approach to materials discovery. Science 268, 1738-1740, (1995).
26. Amis, E. J., Xiang, X. D. & Zhao, J. C. Combinatorial materials science: What's new since Edison? MRS Bulletin 27, 295-297, (2002).
27. Specht, E. D. et al. Metastable phase evolution and grain growth in annealed nanocrystalline Cr-Fe-Ni films. Thin Solid Films 493, 307-312, (2005).
28. Takeuchi, I. et al. Identification of novel compositions of ferromagnetic shape-memory alloys using composition spreads. Nat Mater 2, 180-184, (2003).
29. Takeuchi, I., Lauterbach, J. & Fasolka, M. J. Combinatorial materials synthesis. Materials Today 8, 18-26, (2005).
30. Wang, J. S. et al. Identification of a blue photoluminescent composite material from a combinatorial library. Science 279, 1712-1714, (1998).
31. Senkan, S. M. High-throughput screening of solid-state catalyst libraries. Nature 394, 350-353, (1998).
32. Newsam, J. M. & Schueth, F. Combinatorial approaches as a component of high-throughput experimentation (HTE) in catalysis research. Biotechnology and Bioengineering 61, 203-216, (1998).
33. Tuinstra, H. E. & Cummins, C. L. Combinatorial materials and catalyst research. Advanced Materials 12, 1819-1822, (2000).
34. Bonakdarpour, A. et al. Dissolution of transition metals in combinatorially sputtered Pt1-x-yMxMy ' (M, M ' = Co, Ni, Mn, Fe) PEMFC electrocatalysts. Journal of the Electrochemical Society 153, A1835-A1846, (2006).
35. Maier, W. F., Stowe, K. & Sieg, S. Combinatorial and high-throughput materials science. Angewandte Chemie-International Edition 46, 6016-6067, (2007).
36. Olong, N. E., Stowe, K. & Maier, W. F. A combinatorial approach for the discovery of low temperature soot oxidation catalysts. Applied Catalysis B-Environmental 74, 19-25, (2007).

37. Rende, D., Schwarz, K., Rabe, U., Maier, W. F. & Arnold, W. Combinatorial synthesis of thin mixed oxide films and automated study of their piezoelectric properties. Progress in Solid State Chemistry 35, 361-366, (2007).
38. Seyler, M., Stoewe, K. & Maier, W. F. New hydrogen-producing photocatalysts - A combinatorial search. Applied Catalysis B-Environmental 76, 146-157, (2007).
39. Zarnetta, R. et al. Identification of Quaternary Shape Memory Alloys with Near-Zero Thermal Hysteresis and Unprecedented Functional Stability. Advanced Functional Materials 20, 1917-1923, (2010).
40. Hattrick-Simpers, J. R. et al. Combinatorial investigation of magnetostriction in Fe-Ga and Fe-Ga-Al. Applied Physics Letters 93, (2008).
41. Fujino, S. et al. Combinatorial discovery of a lead-free morphotropic phase boundary in a thin-film piezoelectric perovskite. Applied Physics Letters 92, (2008).
42. Cui, J. et al. Combinatorial search of thermoelastic shape-memory alloys with extremely small hysteresis width. Nat Mater 5, 286-290, (2006).
43. Koinuma, H. & Takeuchi, I. Combinatorial solid-state chemistry of inorganic materials. Nat Mater 3, 429-438, (2004).
44. Takeuchi, I., van Dover, R. B. & Koinuma, H. Combinatorial synthesis and evaluation of functional inorganic materials using thin-film techniques. MRS Bulletin 27, 301-308, (2002).
45. Wuttig, M., Li, J. & Craciunescu, C. A new ferromagnetic shape memory alloy system. Scripta Materialia 44, 2393-2397, (2001).
46. Delacheisserie, E. D. T. & Peuzin, J. C. Magnetostriction and internal-stresses in thin-films - The cantilever methed revisited. Journal of Magnetism and Magnetic Materials 136, 189-196, (1994).
47. Ludwig, A., Cao, J., Savan, A. & Ehmann, M. High-throughput characterization of hydrogen storage materials using thin films on micromachined Si substrates. Journal of Alloys and Compounds 446, 516-521, (2007).

48. Hanak, J. J. & Gittleman, J. I. Iron-Nickel-Silica Ferromagnetic Cermets. AIP Conference Proceedings 10, 961-965, (1973).
49. Zarnetta, R. Combinatorial development and discovery of ternary and quarternary shape memory alloys PhD thesis, der Ruhr-Universitat Bochum, (2010).
50. Hattrick-Simpers, J. R. A combinatorial investigation of magnetostrictive materials PhD thesis, University of Maryland, (2007).
51. Quandt, E., Ludwig, A., Lord, D. G. & Faunce, C. A. Magnetic properties and microstructure of giant magnetostrictive TbFe/FeCo multilayers. Journal of Applied Physics 83, 7267-7269, (1998).
52. Cullity, B. D. Introduction to Magnetic Materials. 1st edn, (Addison-Wesley Pub. Co., 1972).
53. Petersen, K. E. & Guarnieri, C. R. Young's modulus measurements of thin-films using micromechanics. Journal of Applied Physics 50, 6761-6766, (1979).
54. Meirovitch, L. Fundamentals of Vibrations. p400 (McGraw-Hill, 2001).
55. Kubaschewski, O. Iron-Binary Phase Diagrams. (Springer-Verlag Berlin Heidelberg, 1982).
56. Godecke, T. & Koster, W. Constitution of system Fe-Ga between 10 AND 50 at-percent Ga and its dependence on heat-treatment .3. Supercooling diagram and diagrams for processes occurring during annealing of furnace cooled or quenched alloys. Zeitschrift Fur Metallkunde 68, 758-764, (1977).
57. Dasarath.C & Humeroth.W. System iron-gallium. Proceedings of the Royal Society of London Series a-Mathematical and Physical Sciences 286, 141-&, (1965).
58. Kawamiya, N., Adachi, K. & Nakamura, Y. Magnetic properties and mossbauer investigations of Fe-Ga alloys. Journal of the Physical Society of Japan 33, 1318-1327, (1972).
59. Hall, R. C. Single crystal anisotropy and magnetostriction constants of several ferromagnetic materials including alloys of NiFe, SiFe, AlFe, CoNi, and CoFe. Journal of Applied Physics 30, 816-819, (1959).

60. Clark, A. E., Restorff, J. B., Wun-Fogle, M., Lograsso, T. A. & Schlagel, D. L. Magnetostrictive properties of body-centered cubic Fe-Ga and Fe-Ga-Al alloys. IEEE Trans. Magn. 36, 3238-3240, (2000).
61. Guruswamy, S., Srisukhumbowornchai, N., Clark, A. E., Restorff, J. B. & Wun-Fogle, M. Strong, ductile, and low-field-magnetostrictive alloys based on Fe-Ga. Scripta Materialia 43, 239-244, (2000).
62. Clark, A. E., Wun-Fogle, M., Restorff, J. B., Lograsso, T. A. & Cullen, J. R. Effect of quenching on the magnetostriction of Fe1-xGax ($0.13 < x < 0.21$). Ieee Transactions on Magnetics 37, 2678-2680, (2001).
63. Clark, A. E., Wun-Fogle, M., Restorff, J. B., Lograsso, T. A. & Petculescu, G. Magnetostriction and elasticity of body centered cubic Fe100-xBex alloys. Journal of Applied Physics 95, 6942-6944, (2004).
64. Petculescu, G., Hathaway, K. B., Lograsso, T. A., Wun-Fogle, M. & Clark, A. E. Magnetic field dependence of galfenol elastic properties. Journal of Applied Physics 97, (2005).
65. Wuttig, M., Dai, L. Y. & Cullen, J. Elasticity and magnetoelasticity of Fe-Ga solid solutions. Applied Physics Letters 80, 1135-1137, (2002).
66. Khachaturyan, A. G. & Viehland, D. Structurally heterogeneous model of extrinsic magnetostriction for Fe-Ga and similar magnetic alloys: Part I. Decomposition and confined displacive transformation. Metallurgical and Materials Transactions a-Physical Metallurgy and Materials Science 38A, 2308-2316, (2007).
67. Xing, Q. et al. Experimental exploration of the origin of magnetostriction in single crystalline iron. Applied Physics Letters 97, (2010).
68. Mudivarthi, C., Laver, M., Cullen, J., Flatau, A. B. & Wuttig, M. Origin of magnetostriction in Fe-Ga. Journal of Applied Physics 107, (2010).
69. Boisse, J., Zapolsky, H. & Khachaturyan, A. G. Atomic-scale modeling of nanostructure formation in Fe-Ga alloys with giant magnetostriction: Cascade ordering and decomposition. Acta Mater. 59, 2656-2668, (2011).
70. Evans, P. G. & Dapino, M. J. Stress-dependent susceptibility of Galfenol and application to force sensing. Journal of Applied Physics 108, (2010).

71. Ueno, T., Zhang, Z. G. & Higuchi, T. Translatory and Bending Micro Magnetostrictive Actuator using Iron-Gallium Alloys (Galfenol): A New Actuation Approach for Microrobots. Advanced Robotics 24, 1423-1440, (2010).
72. Atulasimha, J. & Flatau, A. B. Experimental Actuation and Sensing Behavior of Single-crystal Iron-Gallium Alloys. Journal of Intelligent Material Systems and Structures 19, 1371-1381, (2008).
73. Basantkumar, R. R., Stadler, B. J. H., Robbins, W. P. & Summers, E. M. Integration of thin-film Galfenol with MEMS cantilevers for magnetic actuation. Ieee Transactions on Magnetics 42, 3102-3104, (2006).
74. Guruswamy, S., Mungsantisuk, P., Corson, R. & Srisukhumbowornchai, N. Rare-earth free Fe-Ga based magnetostrictive alloys for actuator and sensors. Transactions of the Indian Institute of Metals 57, 315-323, (2004).
75. Corson, R. P., Guruswamy, S., McCarter, M. K. & Lin, C. L. Processing of bulk Fe-Zn alloys using explosive compaction. Int. J. Powder Metall. 45, 45-54, (2009).
76. Jiang, H. L., Zhang, M. C., Gao, X. X., Zhu, J. & Zhou, S. Z. Microstructure and magnetostriction of the melt-spun Fe83Ga17 alloy ribbons. Acta Metallurgica Sinica 42, 177-180, (2006).
77. Kellogg, R. A. et al. Tensile properties of magneto strictive iron-gallium alloys. Acta Mater. 52, 5043-5050, (2004).
78. Wun-Fogle, M., Restorff, J. B. & Clark, A. E. Magnetostriction of stress-annealed Fe-Ga and Fe-Ga-Al alloys under compressive and tensile stress. Journal of Intelligent Material Systems and Structures 17, 117-122, (2006).
79. Duenas, T. et al. Micro-sensor coupling magnetostriction and magnetoresistive phenomena. Journal of Magnetism and Magnetic Materials 242, 1132-1135, (2002).
80. Iannotti, V. & Lanotte, L. Improved model for the magnetostrictive deflection of a clamped film-substrate system. Journal of Magnetism and Magnetic Materials 202, 191-196, (1999).

81. Rafique, S. Magnetic anisotropy of $Fe_{1-x}Ga_x$ alloys MS thesis, University of Maryland, (2003).
82. Yang, S. et al. Large Magnetostriction from Morphotropic Phase Boundary in Ferromagnets. Physical Review Letters 104, (2010).
83. Okamoto, H. Desk Handbook: Phase Diagrams for Binary Alloys. Second Edition edn, (ASM International, 2000).
84. Ustinovshikov, Y. & Pushkarev, B. Ordering and phase separation in alloys of the Fe-Co system. Journal of Alloys and Compounds 424, 145-151, (2006).
85. Masiyama, Y. Magnetostriction in Cobalt-Iron alloys. Sci. Rpts. of Tohoku Imperial U. 21, (1932).
86. Williams, S. R. The Joule magnetostrictive effect in a group of cobalt & iron alloys. Review of Scientific Instruments 3, 675-683, (1932).
87. Hall, R. C. Journal of Applied Physics 31, (1960).
88. Domyshev, V. A., Ashchepkov, V. T., Osipov, A. Y., Kuznetsova, I. N. & Kuznetsov, N. A. Dependence of magnetostriction of iron-cobalt alloys on deformation texture, recrystallization and ordering heat-treatment. Fiz. Metallov Metalloved. 57, 1116-1121, (1984).
89. Ishio, S. & Takahashi, M. Magnetostriction in dilute Fe-Co alloys. Journal of Magnetism and Magnetic Materials 46, 142-150, (1984).
90. Dai, L. & Wuttig, M. Magnetostriction in Co-rich bcc CoFe Solid Solutions (Dept. of Mat. Sci & eng., University of Maryland, 2007).
91. Bozorth, R. M. Ferromagnetism. (Macmillan, 1951).
92. Bhattacharyya, S. et al. Nanodispersed DO3-phase nanostructures observed in magnetostrictive Fe-19% Ga Galfenol alloys. Physical Review B 77, (2008).
93. Srisukhumbowornchai, N. & Guruswamy, S. Large magnetostriction in directionally solidified FeGa and FeGaAl alloys. Journal of Applied Physics 90, 5680-5688, (2001).
94. Diaz-Ortiz, A., Drautz, R., Fahnle, M., Dosch, H. & Sanchez, J. M. Structure and magnetism in bcc-based iron-cobalt alloys. Physical Review B 73, (2006).
95. Burton, B. P. & Perrot, P. Fe-Zn (Iron-Zinc) in Phase Diagrams of Binary Iron Alloys. 2309-15 (ASM International, 1993).

96. Ono, H., Shimada, M. & Toma, H. Magnetostrictive properties of a new type of Tb-Dy-Fe-Zn Laves phase compound. Journal of Applied Physics 88, 7213-7216, (2000).
97. Wriedt, H. A. & Arajs, S. Ferromagnetic Curie temperatures of some iron-zinc solid solutions. Physica Status Solidi 16, 475-&, (1966).
98. Zhou, F., Chou, Y. T. & Lavernia, E. J. Formation of supersaturated single-phase bcc solid solutions in Fe-Zn binary system by mechanical alloying. Mater. Trans. 42, 1566-1570, (2001).
99. Zhang, Y. N., Cao, J. X. & Wu, R. Q. Rigid band model for prediction of magnetostriction of iron-gallium alloys. Applied Physics Letters 96, (2010).
100. Guruswamy, S., Jayaraman, T. V., Corson, R. P., Garside, G. & Thuanboon, S. Short range ordering and magnetostriction in Fe-Ga and other Fe alloy single crystals. Journal of Applied Physics 104, (2008).
101. Oduncu, H. & Meydan, T. A novel method of monitoring biomechanical movements using the magnetoelastic effect. Journal of Magnetism and Magnetic Materials 160, 233-236, (1996).
102. Claeyssen, F., Lhermet, N., Le Letty, R. & Bouchilloux, P. Actuators, transducers and motors based on giant magnetostrictive materials. Journal of Alloys and Compounds 258, 61-73, (1997).
103. Guntupalli, R. et al. A magnetoelastic resonance biosensor immobilized with polyclonal antibody for the detection of Salmonella typhimurium. Biosensors and Bioelectronics 22, 1474-1479, (2007).
104. Gibbs, M. R. J. Applications of magmems. Journal of Magnetism and Magnetic Materials 290-291, 1298-1303, (2005).